2017

Performance Assessment of HSRM Concrete Ties Through Finite Element Model Simulations

Adam I. Zeitouni
University of South Carolina

Performance Assessment of HSRM Concrete Ties Through Finite Element Model Simulations

By

Adam I. Zeitouni

Bachelor of Science
University of South Carolina, 2016

Submitted in Partial Fulfillment of the Requirements

For the Degree of Master of Science in

Civil Engineering

College of Engineering and Computing

University of South Carolina

2017

Accepted By:

Dimitris Rizos, Director of Thesis

Juan M Caicedo, Reader

Robert L Mullen, Reader

Cheryl L. Addy, Vice Provost and Dean of the Graduate School

Abstract

Concrete ties have become a promising alternative to timber ties for freight lines with increased curvature, high annual traffic, and large axle loads. They are also widely adopted in passenger lines. High strength (HS) concrete is the material of choice in the fabrication of prestressed concrete railroad ties. The higher strength of the concrete is directly related to higher values of the Elastic Modulus, thus increasing the rigidity of the material. The combination of increased strength, rigidity, and the material brittleness may lead to the development of high amplitude stresses with high gradients, which appears to be a common underlying cause of premature cracking and deterioration observed in some concrete ties. Realizing the current issues associated with the performance of concrete ties and recalling the findings of an almost fifteen-year-old research conducted at the University of South Carolina (USC), a hypothesis was formulated that there is a potential benefit in introducing weathered granite aggregates into mix designs for railroad concrete ties. A high strength, yet lower rigidity, concrete will reduce the amplitude of the stress field and equally important, will regularize the stress field providing for a smoother load distribution that will diffuse stress concentrations. Consequently, the High Strength Reduced Modulus (HSRM) concrete improves the cracking resistance and fatigue performance, thus extending the life of the

tie. A comprehensive research program has been conducted at USC to identify the benefits of using HSRM in concrete ties. The research is based on experimental investigations and computer simulations at the material, component and structural member levels. This work presents the details of the computer simulation studies that were conducted as part of the project. Three-dimensional nonlinear finite element (FE) models have been developed for the HSRM and the "standard" concrete ties. Nonlinear material models based on damaged plasticity are implemented. The steel-concrete bond interface is also modeled and discussed. Validation of these models is conducted through comparisons with laboratory testing of prototype and standard ties, and it has shown excellent accuracy. Subsequently, a series of parametric studies related to varying support conditions in tangent and curved track have been conducted. These studies showed that the HSRM concrete tie outperformed the standard concrete tie in all of the benchmark tests by better distributing its stresses and delaying the initiation of cracks. The analysis results are discussed and future recommendations presented.

Table of Contents

List of Tables

List of Figures

Chapter 1: Introduction

General Background

Railroad ties or sleepers are one of many important structural components that make up the overall railway system. The main purpose of the railroad tie is to support the rail above and distribute the wheel loads from the train to the ballast below. Railroad ties are generally made of wood, however prestressed concrete, steel, and composite ties have been growing in popularity in recent years. In particular, prestressed concrete ties are being used more often amongst class I railroad companies due to their ease of installation, greater life expectancy, reduced level of maintenance, and environmental friendliness among others.

Prestressed concrete ties have pre-set gauges, which makes them relatively easy to install. The high strength and durability of concrete allows the concrete ties to carry large loads over a longer period of time when compared with traditional wood ties. Additionally, this allows concrete ties to be spaced in larger increments, which reduces the overall number of ties needed per mile of track. Concrete ties also have a higher stiffness than wood ties, which provides a stiffer foundation for the overall track systemand therefore reduces the amount of surface and lining (adjusting track to original alignment) maintenance required. Finally, wood ties are often treated with

creosote to increase their resistance to weathering, erosion, and rotting, however the use of creosote in wood ties can present a fire hazard risk due to its flammability. The use of concrete ties eliminates this potential risk. Though prestressed concrete ties offer many advantages when compared to the traditional wood tie, some unforeseen difficulties have arisen, such as premature cracking and deterioration (Kaewunruen & Remennikov, 2009), which is believed to be attributed to the increase in rigidity due to concrete's higher elastic modulus. Lowering the elastic modulus of the concrete, while maintaining it's high strength, could present itself as a solution to the issues above, thus prolonging the life and reliability of concrete ties in the field.

High-Strength Reduced-Modulus Concrete (HSRM) is a relatively new type of concrete that has been developed at the University of South Carolina, Columbia (Ortiz, Caicedo, & Rizos, 2016). As the name suggests, HSRM concrete has a lower elastic modulus, but still maintains the high strength seen in conventional high strength concretes. This counter intuitive behavior is believed to be caused by the mechanical behavior of the coarse aggregates used in the concrete mix. Prototype prestressed concrete ties, using HSRM concrete, have been developed and studied both experimentally in the lab (Abdulqader, 2017) and through finite element (FE) analysis. This thesis presents and compares the results from the computer simulations performed on both the prototype HSRM concrete tie and one of the industry standard ties. ABAQUS was the finite element software utilized in this study.

Objectives of the Study

The objective of this paper is to investigate the performance of the prototype HSRM prestressed concrete tie and compare the findings with that of the "standard tie" through FEM model simulations. If our hypothesis is correct, we expect the HSRM tie to be more flexible, while continuing to match or even outperform the standard tie in its overall load carrying capacity; i.e. better distributing stresses throughout the tie, while maintaining its high strength. In such a case, the prototype tie could offer itself as a possible solution to potential early cracking and deterioration seen in some concrete ties today. It is also hypothesized that the prototype tie could potentially reduce the amount of failures seen in concrete ties caused by faulty ballast. In other words, it is believed that the HSRM tie will better conform to the surface of the ballast and therefore reduce the chance of potential stress concentrations that may occur when the ballast is not distributed uniformly underneath by a loss of ballast support.

Organization of the Thesis

This paper begins with a comprehensive exploration of previous reporting's of field and laboratory investigations on concrete ties, material modeling, FE models of prestressed concrete members, and FE models of prestressed concrete ties. The information learned from these previous studies is used and built upon in order to create comprehensive FE models for concrete ties. The Literature Review chapter is followed by a detailed description of both the prototype and standard tie, such as the

tie geometry, material characteristics, and tie fabrication process. Tie dimensions as well as the experimental methods for determining the aggregate and concrete mechanical properties are discussed in this chapter. Chapter 3 is followed with a comprehensive simulation work plan, which includes descriptions of the benchmark test. The proposed simulations and reasoning behind the proposals are discussed in this chapter. Chapter 5 (Modeling Considerations) discusses assumptions and model considerations taken into account, such as the mesh, material, loads, and boundary conditions. Material models are developed in this chapter. Chapter 6 presents the results from the simulated tests and highlights the important findings from each simulation. Finally, this paper concludes with suggestions and recommendations based on the results presented in this paper.

Chapter 2: Literature Review

Concrete Tie Performance

Field Investigations

One of the biggest advantages that prestressed concrete ties have over traditional wood ties is its much longer service life (generally 20 years depending on climate). However, frequent inspections of many railroad tracks have uncovered numerous concrete ties that have prematurely failed or cracked well before their designed service life. In fact, a 2010 study sponsored by the Railway Tie Association, reported that of the "29 million ties that were installed since the 1970's, approximately 2.2 to 2.7 million ties were reported as failed and replaced" (ZETA-TECH, 2010). That is an approximate failure rate of 7.9 to 9.2%. These unexpected findings have prompted the need for further field investigations in order to assess the performance and behavior of concrete ties in service. Mayville, Jiang, and Sherman (2014) studied the performance of concrete ties that were installed on the Northeast Corridor (NEC) in an attempt to determine the factors that lead to these cases of early cracking of the concrete tie (Mayville et al., 2014). In particular, the authors sought to study the horizontal cracking phenomenon that has been known to appear along the top row of prestressed steel tendons located at one or both ends of the tie. The author's sampled different concrete

ties of varying ages and from five separate locations along Amtrak's rail lines in the NEC. The concrete ties were inspected in both the field and laboratory. The concrete ties in the field were examined visually and non-destructively by the impact echo method. Laboratory tests were performed for modulus and strength, tensile strength, and flexural strength data among others. Furthermore, the authors simulated various tests on the concrete ties by conducting finite element analysis. Based on the results from their extensive examinations of the concrete ties, the authors concluded that the premature cracking of the concrete ties is caused by a combination of contributing factors working together. The first main factor can be attributed to a high concentration of tensile stress in the concrete ties, primarily located at the location of the prestressing steel, which is caused by the transfer of forces when the prestressed strands are released. The second main contributing factor is associated with the pressures produced by alkali-silica reaction (ASR) that were seen to cause additive stresses to those already from the prestressing. Additionally, the authors concluded that other factors, such as cyclic freezing and thawing, delayed ettringite formation, and stresses due to fastener inserts or unusual tie vibrations were not major contributors to the premature cracking of concrete ties. Longitudinal cracking of concrete crossties is not the only concern related to the premature failure of concrete crossties. A survey, conducted by the RailTEC program at the University of Illinois at Urbana-Champaign, polled professionals pertaining to the rail industry on the performance of concrete crossties and elastic fastening systems (Van Dyk et al., 2012). The feedback received showed that the deterioration of concrete beneath the rail, shoulder/fastening system wear or fatigue,

cracking from dynamic loads, derailment damage, and cracking from center binding are the five most critical failures of concrete ties in North America. This has prompted the need for further investigations of these failure methods, such as Zeman's (2010) extensive study on the rail seat deterioration of concrete crossties and Manda et al. (2014) study on the effect of static and dynamic loads on the crosstie and fastening system.

Laboratory Investigations

The Advanced Railroad Technology Group (ARTG), at the University of South Carolina (USC), has continued their widespread and extensive studies on both HSRM material and its performance in concrete crossties. The ARTG has performed both laboratory and finite element model investigations into HSRM concrete. A few examples of the experimental tests performed on the HSRM and standard concrete tie at USC include Rail Seat Positive and Negative Bending Tests, Center Negative and Positive Bending Tests, Four Point Flexural Bending Test, Fatigue on Rail Seat Negative Bending Test, and Fatigue on Center Negative Bending Test. The ARTG has organized and recorded all of the experimental tests and results onto their online data warehouse, "https://sdii.ce.sc.edu/ties-project/" (Rizos, 2014).

The RailTEC group at the University of Illinois at Urbana-Champaign has recently performed a comparative study on the performance of the HSRM crossties against one of the industry standard ties, which is referred to as "standard crosstie" (RailTEC, 2016).

The RailTEC group performed tests such as the Fastening Insert Test and Fastener Uplift Test, which are in accordance with and described in the American Railway Engineering and Maintenance of Way (AREMA) Manual on Railway Engineering. Also, the RailTEC group performed two additional in house Crosstie Flexural Tests, which included loading the crosstie simultaneously at its rail seat and a different support scenario for the two cases. The first support scenario represents a full support, in which a 1 in. thick rubber pad supported the entire length of the crosstie. The second support scenario represents a center-binding case, in which same rubber pad was used to support the middle section of the crosstie, leaving the two ends of the tie unsupported. The RailTEC group found that both the standard and HSRM crossties passed the Fastening Insert Test and Fastener Uplift Test, however the HSRM crosstie outperformed the standard crosstie when the these tests were performed until failure. The standard crosstie cracked at a load of 31.6 kips and was the insert was pulled out at 34.6 kips, while the HSRM crosstie cracked at a load of 33.2 kips and the insert was pulled out at 35.1 kips. The RailTEC group measured similar strains and bending moments between the standard and HSRM crossties. The standard and HSRM crossties also showed similar gauge widening, with the HSRM widening slightly more. Finally, the HSRM crosstie seemed to develop more cracks than the standard crosstie, however these cracks were more small or short. The standard crosstie showed less cracks, however the cracks were larger or deeper. This discovery could provide further evidence on the hypothesis that the HSRM tie is better at distributing its loads throughout, where the standard tie may be more prone to stress concentrations.

Material Modeling

The plastic behavior for reinforced concrete is modeled by two approaches via ABAQUS/Standard: Smeared Cracking Model and Concrete Damaged Plasticity (CDP) Model. The CDP Model is commonly used because of its relatively good convergence and its ability to handle monotonic, cyclic, and dynamic loading, where as the smeared cracking model is only able to handle monotonic loading. The CDP Model is based off the findings of Hillerborg et al. (1976), Lee J. and G. L. Fenves (1998), and Lubliner et al. (1989).

The CDP Model is a generally accepted approach for modeling the nonlinear behavior of concrete and has been used by many authors for various applications, such as reinforced, prestressed, fiber reinforced or plain concrete members (Tao & Chen, 2015; Yapar et al., 2015; Kmiecik & Kamiński, 2011). Additionally, CDP models have already been utilized and employed in prestressed concrete models specific to concrete crossties (Kaewunruen et al., 2016; Yu et al., 2011; Rezaie & Farnam, 2015). Thus, a CDP model has been chosen as the preferred material model for this research due to the fact that CDP models have been widely used in many reinforced or prestressed concrete models, especially for concrete crossties, and because of it's versatility in regards to the types of loads it can handle.

Prestressed Concrete Members

The desire to study the behavior of prestressed concrete members has generated the need for accurate finite element models that can predict the response of

such members. Kannel et al. (1997) developed a three-dimensional finite element model of a pretensioned concrete girder in order to study the influence of different release methodologies on the end cracking in pretensioned concrete girder. The authors modeled the steel strands with truss elements and the concrete with continuum elements. The authors modeled the transfer of the longitudinal prestressing force using two different approaches. The first approach involved linearly varying the steel strands cross-sectional area from zero (at the end of the concrete girder) to its nominal area (at the end of the transfer length). The second approach involved modeling the steel-strand interface with rigid springs containing a plastic behavior.

Arab et al. (2011) presents a methodological approach for modeling three-dimensional pretensioned concrete members at the release of the pretensioned 7-wire strands. The Concrete Damaged Plasticity Model (CDP) was used to model the inelastic behavior of the concrete. Two techniques were used to model the steel-concrete interface. The extrusion technique was the first method that was used and consists of modeling the strands themselves and arranging them within the extruded concrete specimen. A friction contact model, comprised of a normal and tangential behavior, is assigned between the steel and the concrete for the extruded model. The embedment technique is the second method that was used and involves the embedding of the steel elements inside a host element. This approach does not require any contact modeling, but instead eliminates the degrees of freedom at the embedded elements nodes and converts the nodes to “embedded nodes”. The authors concluded that the extruded models provided greater detail at the actual steel-concrete interface, such as bond

stress, transfer length, slippage, etc., but was more computationally expensive than the embedded model.

Abdelatif et al. (2014) developed three models in order to simulate the transfer of the prestress force to the concrete. The first model is an analytical one that is based on the thick-walled cylinder theory, with the steel and concrete being assigned a linear elastic behavior. This model is used to predict the transmission length and the stress profile that is observed within the transmission zone. The second model is an axi-symmetric model that is used for the purpose of validating the analytical model. The third model is a nonlinear finite element model that incorporates a Concrete Damaged Plasticity Model. The steel-concrete interface was modeled using a surface-to-surface contact with an augmented Lagrange multiplier for the normal behavior and the penalty method for the tangential behavior. It was determined that the shrinkage losses should not be subtracted from the initial prestress in order to account for concrete shrinkage. It was also determined that the element size does not significantly affect the prestress transfer. Finally, this study offers valuable insight on the influence that the strand diameter, concrete cover, concrete strength, initial prestress, section size, member length, time of prestress releasing, and surface condition of the strand have on the prestress transfer.

Prestressed Concrete Ties

As the interest in the mechanical behavior of prestressed concrete crossties continues to grow, so has the desire for accurate finite element models that can

simulate these behaviors by imposing various loading scenarios or support conditions. Kaewunruen and Remennikov (2006) developed three-dimensional finite element models for concrete sleepers within ANSYS. In particular, the authors wanted to study the response of the concrete crosstie due to pre-tensioning and the release of the strands. The authors modeled the concrete with solid bricks (SOLID65) and the prestressing wires by embedding three-dimesnional spar elements (LINK8), similar to a truss element in ABAQUS, within the concrete. The authors assumed perfect bonding between the steel-strand interfaces.

Yu et al. (2011) developed finite element models of prestressed concrete crossties in order to simulate the effects of a concrete tie that is loaded at its rail seats with a representative ballast and subgrade supporting it underneath. Two geometrically different crossties were modeled. The first model is an 8-strand tie with a strand diameter of 3/8". The second model is a 24-wire tie with a wire diameter of .207". The authors assume the prestressing steel to be linear elastic with a perfectly plastic yield strength. The authors utilized the concrete damaged plasticity model, supported by ABAQUS, in order to model the nonlinear behavior of the concrete. The authors proceeded to model the concrete-stand interface by representing the bond of the steel to the concrete by using cohesive elements of negligible thickness. Finally, the ballast and subgrade were modeled with an Extended Drucker-Prager model. In order to simulate the transfer of load from the prestressed steel to the concrete, the authors first defined a predefined stress to the steel strands of 1,074 and 1,342 Mpa for the 8-strand and 24-wire models. The prestressed strands were released in their own static

general step. The authors make note of some interface deterioration at the strand ends. Next, a two pressure loads of 344.7 Mpa are applied to the rail seat in a second step. The pressure is allowed to ramp up linearly over the defined step time of one second. The authors conclude that the 24-wire tie retains the pretension force better than the 8-strand tie due to the higher bonding surface areas. Also, the authors conclude that the 24-wire tie is able to withstand slightly higher rail seat loadings before failure.

Yu and Jeong (2015) later built upon their previous models by further developing the steel-strand interface specific to the seven-wire prestressing strands that are commonly used in many concrete crosstie designs. The authors used a "thin" layer of cohesive elements between the strands and concrete in order to represent the strand-concrete interface. The bond parameters for this interface were calibrated through the performance of both un-tensioned pullout tests and pre-tensioned prism tests on concrete specimens. For the un-tensioned pullout test, four seven-wire steel strands, with a nominal diameter of 3/8", were embedded 4 in. inside the concrete specimen, so that the embedment length and bond breaking length are both 4 in. The concrete specimen was enclosed within a steel tub casing that had an inner diameter of 4 in. (101.6 mm). Both the pullout force and displacements were recorded from the unloaded and loaded regions of the specimen. The pre-tensioned prism test consisted of four steel strands that were embedded inside rectangular concrete prism with dimensions of 5.5 x 5.5 x 69 inches. The strands were placed in a square shape with every two strands being spaced 2 inches apart. The steel strands were pre-tensioned with an initial force of 17,415 lbs or an initial tensile stress of 157,678 psi. The strands

were released after the concrete had reached its specified release strength and the surface strains along the concrete were measured in order to calculate the transfer length. The authors performed three tests, which varied based on the concretes compressive strength at the release of the strands: 3,500, 4,500, and 6,000 psi. The bond parameters were than calculated based on the experimental tests and then introduced into their previously developed finite element models of a prestressed concrete tie. Center negative moment tests were performed, both experimentally and through computer simulations, on the concrete crossties in order to test the validity of the newly calculated bond parameters. The authors concluded that the concrete models using a frictional bond model and the model using adhesive/frictional/dilatational bond models were within 4.9% and 11.3% of the experimental failure load. In both models the elastic regions seem to coincide with the experimental results. The adhesive/frictional/dilatational bond model predicts an ultimate failure load that is 17% higher than the model using a frictional bond model.

There are few publications on the effects of HSRM concrete crossties through finite element analysis simulations (Ortiz, Caicedo, & Rizos, 2016; Rizos, 2016). This thesis plans to fill this gap by producing nonlinear finite element models for HSRM crossties and study it's response to various loading and support scenarios.

Chapter 3: The Prototype Concrete Tie

Geometry

The tie design used in this research is based on an industry standard tie that is developed by one of the major class I tie manufacturers in the United States. This tie is not commercially available. The geometry of the tie and its cross section is shown in Figure (3.1). The tie is 2,590.8 mm (8'-6") long and 266.7 mm (10.5") wide. The concrete tie contains eight 7-wire low relaxation strands. The diameter of each strand is 9.525 mm (3/8"). The prestressed steel strands are Grade 270K standards and conform to ASTM A886. The geometry and prestressed strands used in this study are the same for both the standard and prototype tie. The only difference between the two ties is the concrete used in each. The concrete mix design used in the standard tie has been provided by the tie manufacturer. The mix design for the prototype tie is the same as in the standard, with exception to the coarse aggregates used. A detailed description of the design parameters used in this study is shown in Table (3.1).

Table 3.1: Experimental tie parameters

Experimental Tie Parameters					
Description	**Symbol**	**SI**		**US Customary**	
Area of Tie at Rail Seat	A_{tr}	**52,257.96**	mm^2	**81.00**	in^2
Area of Tie at Center	A_{tc}	**46,128.94**	mm^2	**71.50**	in^2
Strand eccentricity at railseat	**e**	**11.43**	mm	**0.45**	in
Section modulus wrt bottom of tie	S_B	**2,755.90**	mm^4	**108.50**	in^4
Strand diameter	d_s	**9.53**	mm	**0.38**	in
Strand area	A_s	**71.25**	mm^2	**0.11**	in^2
Prestressing force/strand	P_i	**76.73**	kN	**17.25**	kip
Effective force/strand	P_e	**68.31**	kN	**15.36**	kip
Strand Stress	σ_i	**1,077**	Mpa	**156.19**	ksi
Effective Strand Stress	σ_{ie}	**959**	Mpa	**139.04**	ksi
Number of strands	N_s	**8**		**8.00**	
Total Prestressing force	P_{si}	**614**	kN	**138.00**	kip
Total effective force	P_{se}	**546**	kN	**122.85**	kip
Elastic Modulus for Steel	E_s	**200**	Gpa	**29,000.00**	ksi

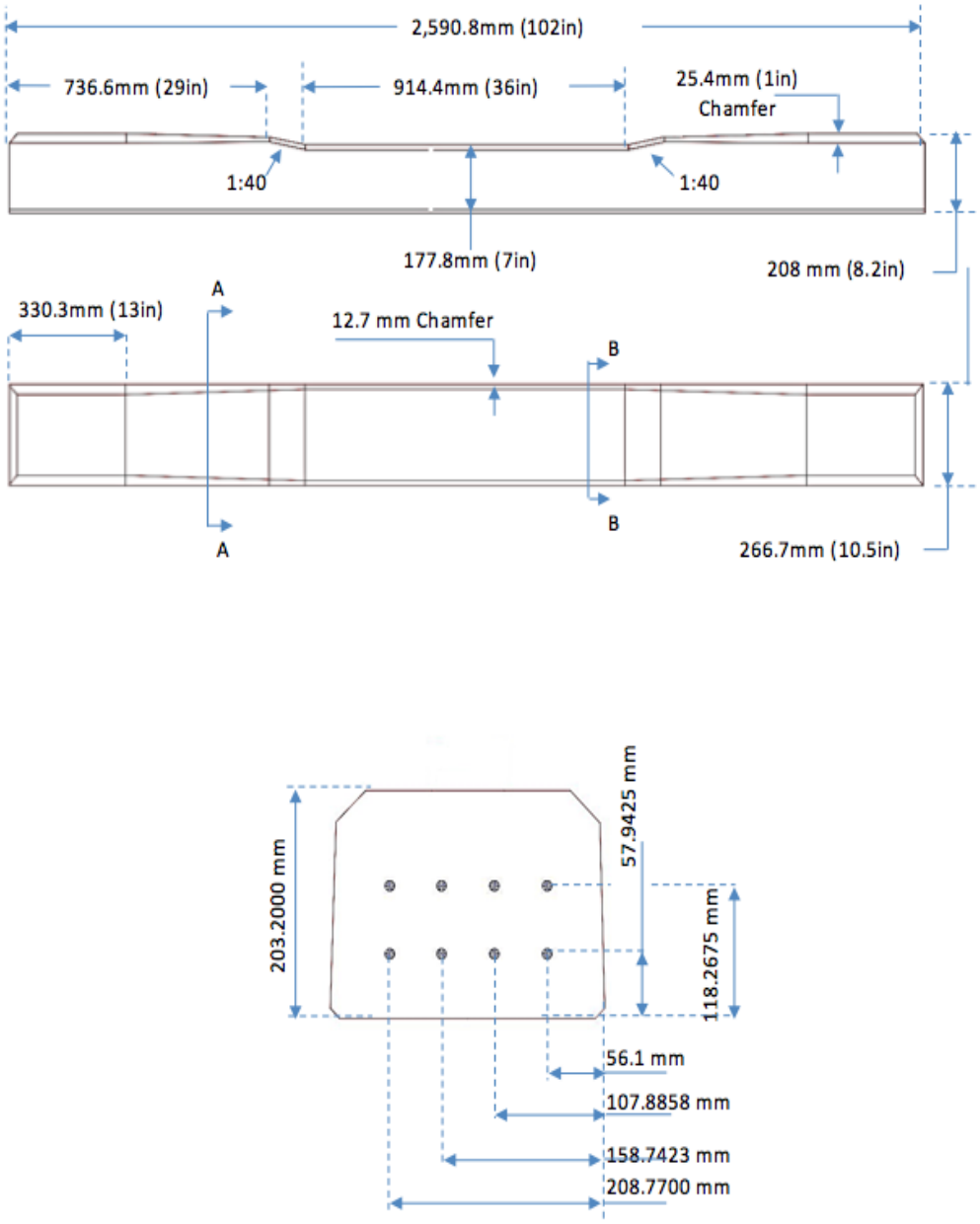

Figure 3.1: Concrete tie geometry and cross-section

Materials

Standard

The tie manufacturer has provided the mix design used in this study for the standard tie. Type III cement, conforming to ASTM C150, is used in order to provide high early strength, so that the tie can withstand the stresses due to the release of the pre-tensioned strands at 1 day. Admixtures are used in the mix to increase the workability of the wet concrete during its production. The same fine and coarse aggregates used by the tie manufacturer were shipped to the USC Structural Laboratory and used in material characterization studies. The coarse aggregate used in the standard tie has been termed "CA-1" and is a limestone type rock. Figure (3.2) shows an image of the CA-1 aggregate used in this study.

Extensive laboratory studies were performed on the coarse aggregate in order to define the aggregates mechanical and visual characteristics. For example, a few of the ASTM standard tests performed on the crushed aggregate include ASTM C29, ASTM C127, ASTM C131, and ASTM C136 in order to define the aggregates density, absorption, resistance to degradation, and particle size distribution. The elastic modulus of the aggregate is obtained from previous studies (Zhou, Lydon, & Barr, 1995) on limestone aggregates used in concrete and is shown in Table (3.2).

After investigations into the aggregates properties were completed, standard concrete cylinders were prepared and tested experimentally in the lab. Multiple batches of concrete were created. Within each batch, cylindrical concrete specimens were

formed and cured in 4”x8” molds according to ASTM C192. The concrete specimens were allowed to cure in an environmentally controlled and undisturbed area until the time of testing: 1, 7, 14, 28, 56, and 90 days. The concrete specimens were tested under uniaxial compressive loading for strength and modulus per ASTM C39. Displacements encountered during the loading procedure were measured by attaching a rig, containing four Linear Variable Differential Transformers (LVDT’s), to the concrete specimen. The displacements measured by the LVDT’s can be converted into strains through the given gauge length. Figure (3.3) shows an example of a concrete specimen with the attached rig and LVDT’s. Furthermore, the concrete specimens were “capped” on both ends with un-bonded steel retainers containing neoprene pads. These measures are taken in order to insure a smooth, uniform, and parallel contact surface that is perpendicular to the axially applied load. Figure (3.4) shows a concrete specimen with capped ends following its failure. An average value for the standard concrete’s 28-day elastic modulus and compressive strength is recorded in Table (3.2).

Table 3.2: Mechanical properties for the concrete's compressive strength, elastic modulus, and the aggregate's elastic modulus

Concrete Type	f'_c	E_c	E_a
Standard	8,620 psi 59.4 (Mpa)	4,660,000 psi 32,100 (Mpa)	8,260,000 psi 56,900 (Mpa)
HSRM	9,100 psi 62.7 (Mpa)	3,340,000 psi 23,000 (Mpa)	3,480,000 psi 24,000 (Mpa)

Figure 3.2: Limestone aggregate defined as "CA-1"

Figure 3.3: Concrete specimen with an attached rig and LVDT's

Figure 3.4: An example of a capped concrete specimen following its failure

HSRM

High-Strength Reduced-Modulus concrete is a relatively new type of concrete that was developed and is being studied at the University of South Carolina. HSRM concrete has the potential to compete with traditional high strength concrete in certain applications because of its ability to maintain a high strength without developing a high elastic modulus. This behavior is believed to be a result from the coarse aggregates used for the concrete. The aggregate used in the HSRM concrete has been termed "CA-3" and is a "weathered" granite. The weathered aggregate was provided by a local rock quarry located in the southeast. The quarry also provided a large boulder-like sample of CA-3 for further testing. Figure (3.5) shows an image of the CA-3 aggregate.

The same mix design was used for the HSRM concrete as the standard concrete with exception to the aggregates used. As with CA-1, the same laboratory investigations were performed on CA-3. However, additional tests were needed in order to define the aggregates elastic modulus and Poisson's ratio. In an effort to define these properties, cylindrical specimens were cored out of the larger boulder-like rock and tested in uniaxial compression. The coring process is depicted in Figure (3.6). The cored specimens have a diameter and height equal to 57.15 mm (2.25") and 114.3 mm (4.5"), yielding a L/D ratio of 2. This is within the acceptable range per ASTM D4543.

The elastic constants of the rock cores, E (elastic modulus) and Nu (poisson's ratio), were found by testing the specimens in uniaxial compression according to the ASTM D3148. The axial and longitudinal strains used in the calculation of these constants were measured using the Digital Image Correlation (DIC) method. This method has been verified and proven to provide accurate and detailed results (Sutton et al., 2017). Figures (3.7-3.8) show the test setup and a typical strain profile that one may obtain by using the Digital Image Correlation method.

Similarly to the procedures for the standard concrete, multiple batches of HSRM were produced and tested. The same process and techniques that were used in the testing of the standard concrete were performed for the HSRM concrete. Values for the modulus of aggregates, concrete, and average compressive strength of both concrete is reported in Table (3.2), where E_c is the modulus of the concrete and E_a is the modulus of the aggregate.

Figure 3.5: Weathered granite aggregate defined as "CA-3"

Figure 3.6: Coring process for obtaining the rock core specimens

Figure 3.7: DIC setup for the testing of the rock core under uniaxial loading

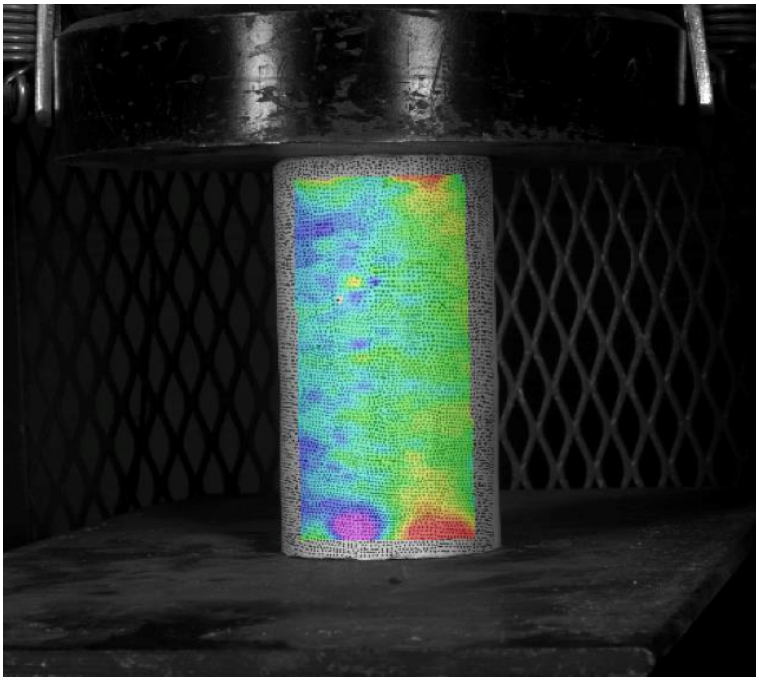

Figure 3.8: Example axial strain profile of a rock core specimen at a given load obtained through DIC technique

Prototype Fabrication

The prototype HSRM ties were fabricated in the plant warehouse of one of the major pre-stressed concrete tie manufacturers in the US. The ties were manufactured in September of 2015. In this particular plant, the freshly prepared wet concrete is poured into a pre-stressing bed, which consists of a total 37 cavities arranged in series. Each cavity is comprised of 8 steel forms, in which the wet concrete is allowed to harden. Each cavity is enclosed on both ends by removable steel blades. The steel strands run continuously throughout the length of the bed: eight strands per steel form. Before the concrete is poured in the forms, the strands are pre-tensioned with an initial force of 76.8 kN (17.25 Kip) by a hydraulic system at one end of the bed. On the other side of the bed, the steel stands are anchored on a bulkhead. For simplicity, the bed end containing the hydraulic system has been designated the “live end”, where as the bed end anchoring the strands has been designated the “dead end”.

A total of thirty-two HSRM ties and eight standard ties were fabricated and then shipped to the Structural Laboratory at USC for further testing. The ties arrived to the testing laboratory approximately three months after fabrication. Upon arrival, the ties were arranged and stored in a designated area, free from potential disturbances.

Chapter 4: Simulation Work Plan

Model Validation Studies

One of the most important components of this research is to develop working finite element models for the HSRM and standard concrete crossties in order to simulate their responses to various loading and support conditions. However, before any hypothetical simulations of loading and support conditions can be commenced, the material model and steel-strand interface must first be validated in order to ensure accurate results. In order to validate these models, a Four Point Flexural Bending Test is proposed to be experimentally performed, in USC's Structural Laboratory, on the standard concrete crosstie and use the results of this test as a benchmark for the finite element model. The tie will be inverted upside-down and supported between each of its rail seats by steel rollers. A spreader beam, with two attached rollers, will be connected to the actuator in order to introduce equal loads at two points. The two rollers, where the load is applied, will be spaced 34 inches (863.6 mm) apart from each other and each roller will be 17 inches (431.8 mm) from the midspan of the tie. The roller supports are an additional 13 inches (330.2 mm) from the loaded roller or 30 inches (762 mm) from the midspan. Figure (4.1) shows a schematic of the proposed Four Point Flexural Test. The displacement at the midspan of the concrete tie will be measured using LVDT's and

the DIC method. Additionally, the DIC method will be utilized in order to measure surface strains and stresses along the face of the concrete tie specimen. The concrete tie will be loaded in a series of steps (0-2 kips, 2-5 kips, 5-10 kips, etc…) with a loading rate of 5 kips per minute until the ties ultimate failure. Data will be recorded continuously throughout the entirety of the test.

After the ultimate failure of the crosstie, cylindrical concrete specimens will be cored out from the two ends of the tie itself. These specimens will then be tested for strength and modulus per ASTM C39. The results from the testing of the cored specimens will be utilized in order to calibrate the material models that will be used for the finite element simulations. Also, these values will be used to create the HSRM material models as discussed in the next section. Once the finite element models for the standard concrete crosstie have been validated with the benchmark Four Point Flexural Bending Test, studies can be commenced on the behavioral response of the concrete tie due to a reduction of its elastic modulus.

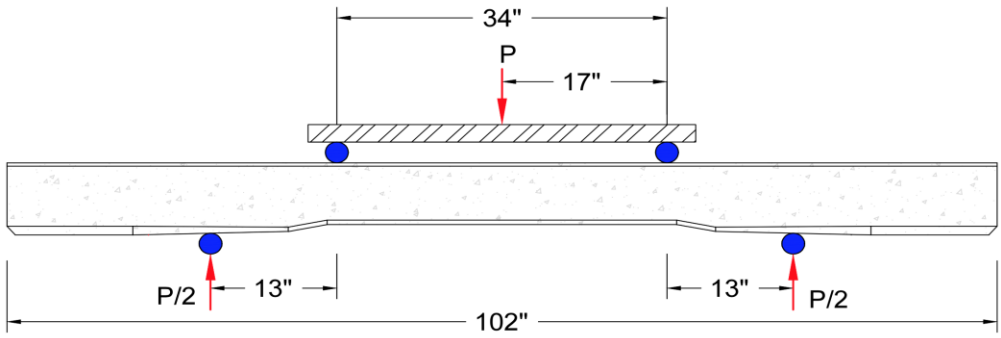

Figure 4.1: Proposed Four Point Flexural Bending setup

Standard Vs HSRM Concrete

Based on experimental lab testing, HSRM concrete is observed to reduce the concrete's modulus of elasticity by as little as 22.6% and as high as 40% (Rizos, 2014). Furthermore, the concrete's compressive and tensile strength is noticed to be very similar and in some cases slightly higher than the standard concrete. Due to these findings, two different material models for the HSRM concrete are formulated by using these percentages as lower and upper bounds for the concrete, while keeping the concretes compressive and tensile strength constant throughout the three different material models. In other words, the standard concrete will be tested for both its strength and modulus characteristics and two additional models will be created with the same strength as the standard, but with a reduced elastic modulus of 22.6% and 40%. In doing this, the elastic modulus is isolated as the primary parameter in order to study the significance of reducing the concretes modulus, while maintaining its strength, which is what is observed with the HSRM concrete. Further details and equations used to define the material models are discussed in more detail in the "Materials" section under Chapter 5, Modeling Considerations.

Simulation of In-Track Performance

Varying Tie Support Condition

In the "field", railroad crossties are almost always supported by an aggregate ballast that lies underneath them. Ideally, the ballast should be uniformly dispersed

beneath the tie, thus fully supporting the tie. However, over many years in service the ballast supporting the ties can shift, leaving pockets of void spaces underneath the tie and thus creating a non-uniform support. If these pockets remain unaddressed, a potential for unwanted moments and stress concentrations may arise as the tie is loaded. These additional stresses and/or moments can then produce a hazardous environment for the structural integrity of the concrete tie. However, a concrete that is more flexible than traditional high strength concrete, while preserving that high strength (HSRM concrete), could reduce the risk that such an environment produces by the tie better conforming to the uneven surface beneath and thus reducing the magnitude of stress seen by the tie by better distributing the stresses within the it.

In order to test this hypothesis, three supporting conditions are proposed for the for the finite element analysis simulations: continuous support, center binding support, and end supported. The continuous support case represents the ideal situation in which the ballast is uniformly distributed beneath the tie. The center binding support represents the scenario in which the ballast has shifted underneath both ends of the concrete tie, thus only supporting the middle portion of the tie. These two support scenarios have been previously applied in experimental tests on concrete ties (RailTEC, 2016). Finally, the end supports represents the scenario in which the ballast has shifted underneath the center region of the tie, thus supporting the tie only at its ends. Figures (4.2-4.4) show simplified representations of the three proposed support scenarios for this study, where P is the total applied load.

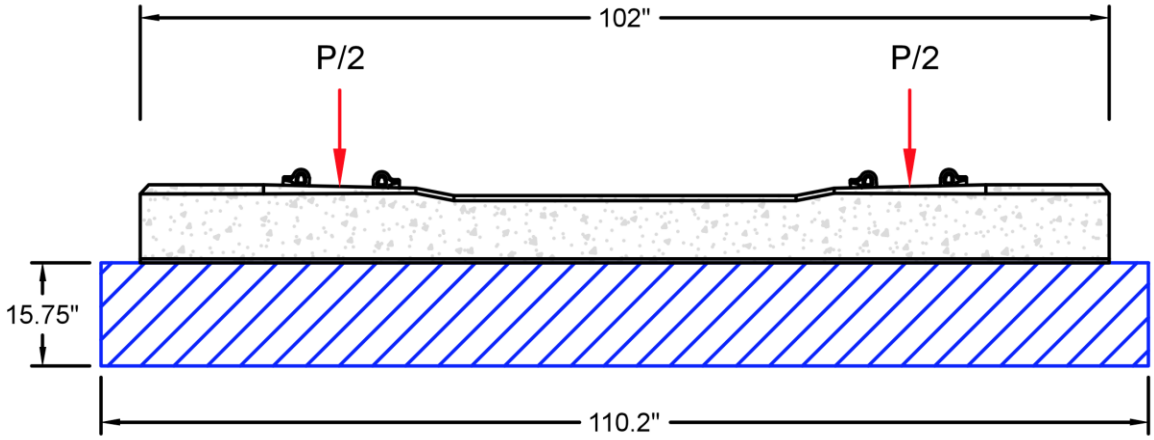

Figure 4.2: Idealized setup for the continuously supported tie

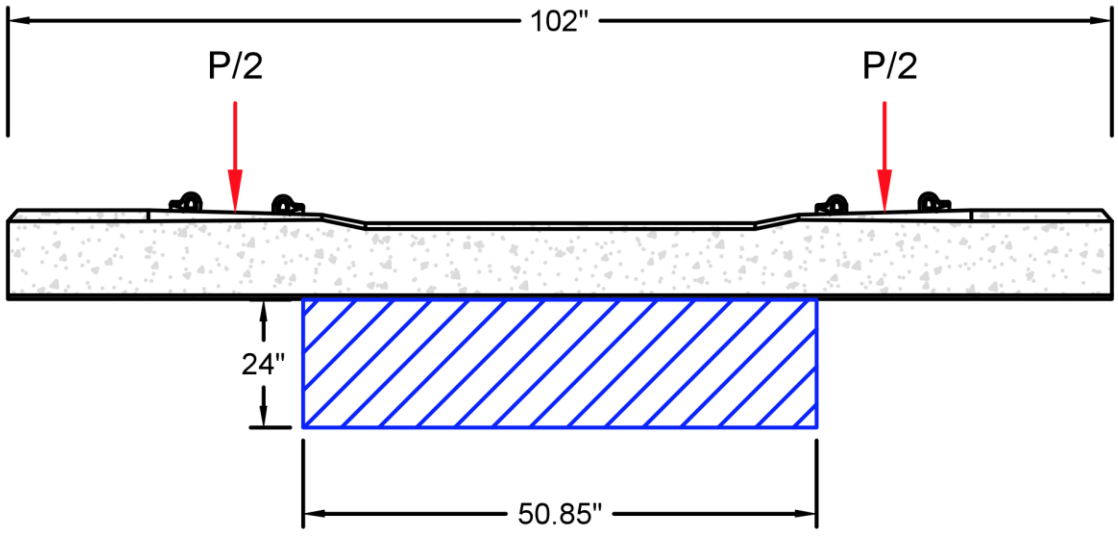

Figure 4.3: Idealized setup for the center binding support

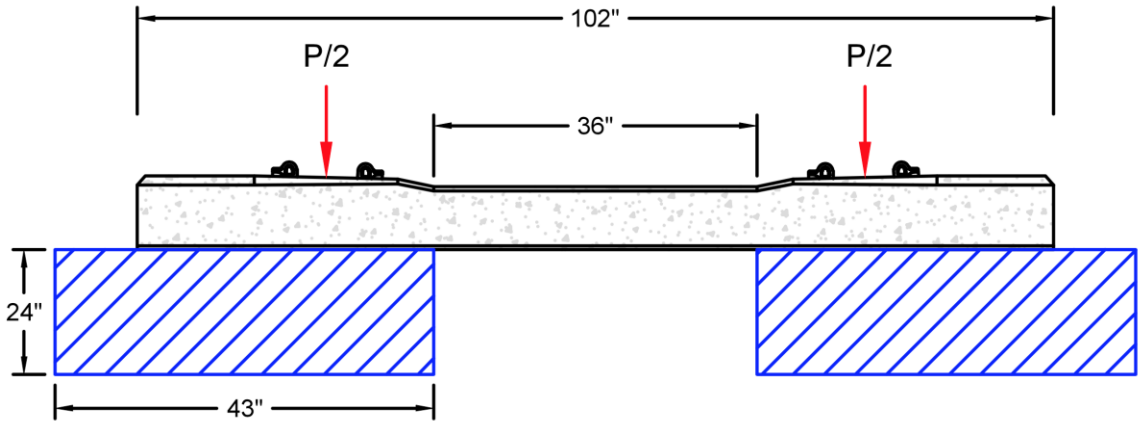

Figure 4.4: Idealized setup for the concrete tie with its ends supported

L/V Load Ratio

In addition to the three previously proposed support conditions, two loading scenarios within each support setup are considered: L/V = 0 and L/V = .6. The L/V load ratio represents the ratio of the laterally applied load over the vertically applied load. For practical purposes, L/V = 0 represents a case where the train is moving along a straight and level track, where as an L/V = .6 represents a case where the train is moving along a curved track. Additionally, for the case of L/V = .6, it is intuitively obvious that the lateral load should only be applied at one rail seat in the direction that points toward the field side. A load of 40 kips per rail seat is chosen as the vertical load to be applied, as well as an additional 24 kips applied laterally at on rail seat for the case of L/V = .6. The vertical load of 40 kips is chosen based on the Cooper E-80 loading scenario, when the locomotives front wheels are passing over the tie. Furthermore, the loads are applied as distributed pressures that are applied to the rail seat area. Figures

(4.5-4.6) show an example of each L/V load ratio scenario for the continuous support condition. In total, there are 18 proposed simulations that will be run. This is a reasonable assumption for the objectives of this analysis.

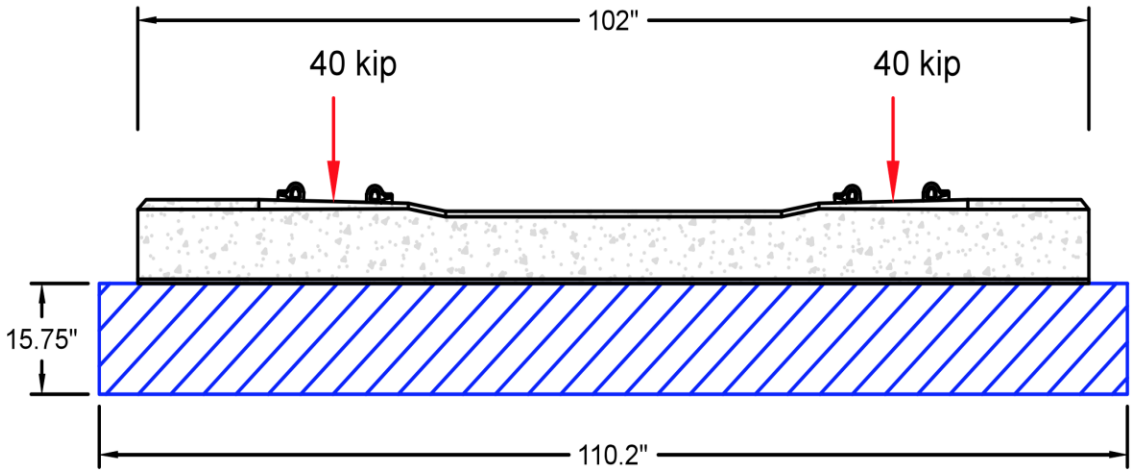

Figure 4.5: Continuous support with L/V = 0 load case

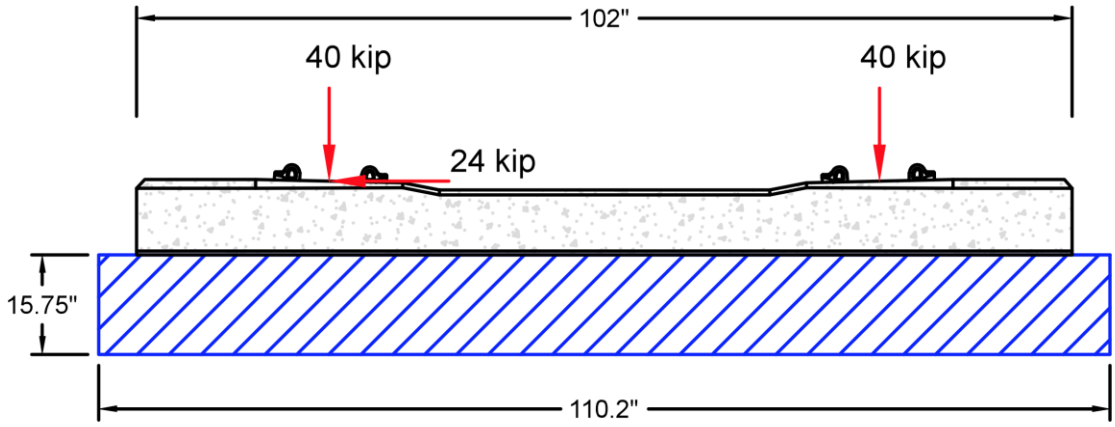

Figure 4.6: Continuous support with L/V = .6 load case

Chapter 5: Modeling Considerations

The finite element models developed in this study are created using the commercially available finite element software, ABAQUS. The model consists of four domains, i.e., the concrete, the steel strands, the interface between the concrete and steel domains and the ballast. This chapter discusses the geometry and mesh of these domains, the materials models used in each domain, the loading and boundary conditions and the solutions procedure and steps.

Geometry and Mesh

Concrete

The concrete tie is modeled as a 3D deformable solid. Figure (5.1-5.2) depicts the geometry of the tie and mesh of half the tie. The dimensions of the modeled tie are consistent with the reported values in Figure (3.1). The tie geometry is discretized into 183,840 elements using 8-node linear brick elements with reduced integration and hourglass control (C3D8R). ABAQUS provides a few options for modeling the inelastic behavior of concrete. A concrete damaged plasticity model is utilized in this study and is discussed further in the "Materials" section of this paper.

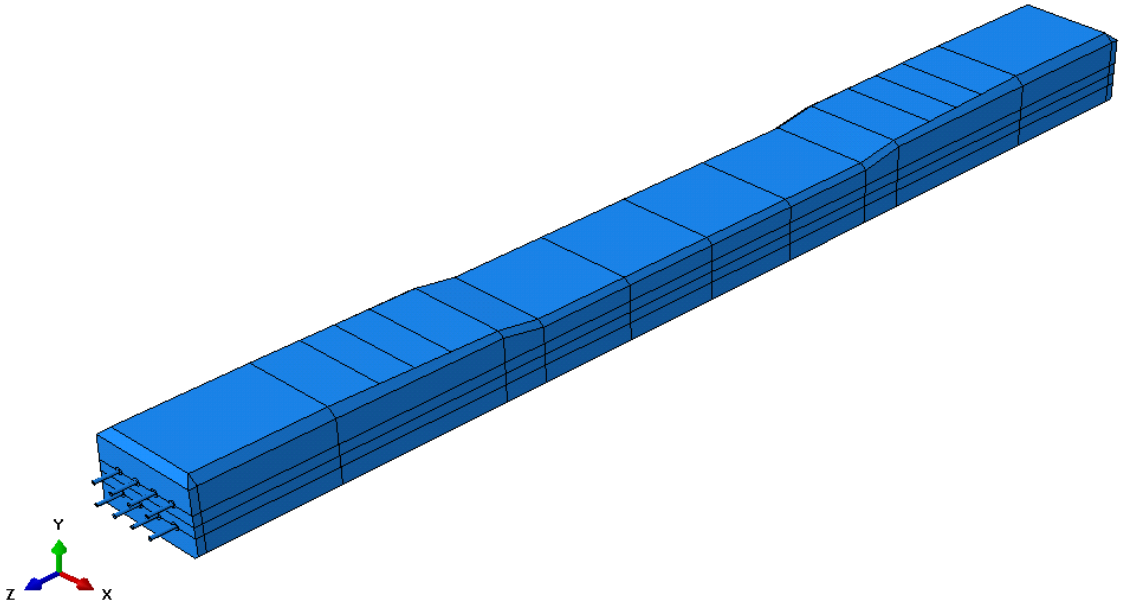

Figure 5.1: Image of the tie geometry developed in ABAQUS

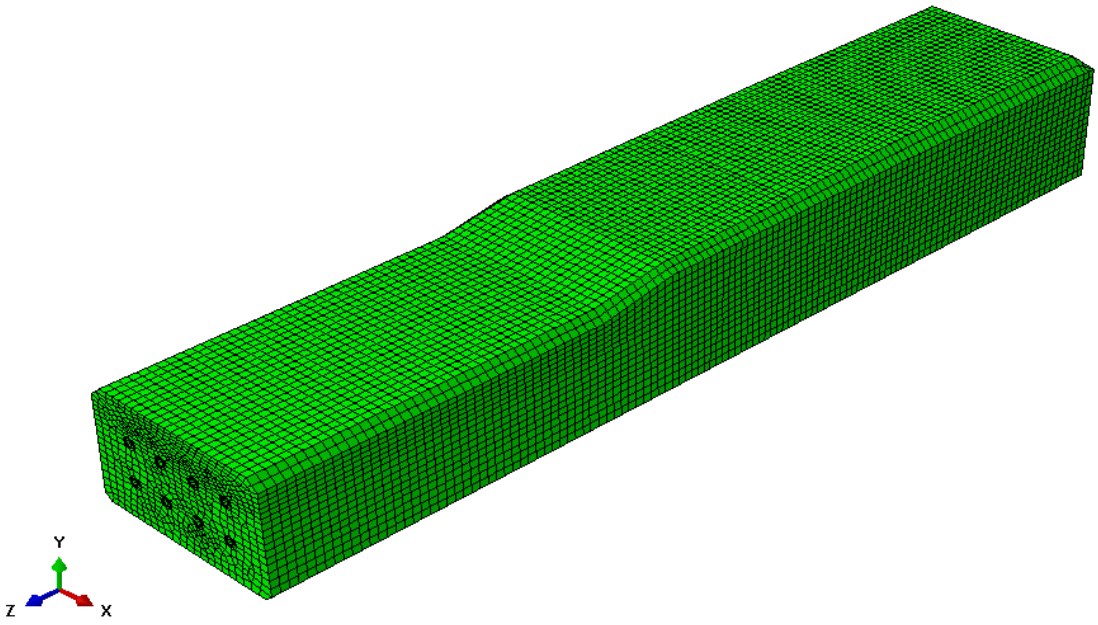

Figure 5.2: Depiction of the concrete mesh for half the tie

Strands

The steel strands are modeled as 3D deformable objects. Eight steel strands, each with a diameter of 9.525 mm (3/8”), are used in this particular tie design. Each strand is discretized into 1,080 elements using C3D8R for a total of 8,640 elements. The steel is assumed to be linear elastic. Its mechanical properties are reported in the “Materials” section.

Concrete-Strand Interface

The bonding interface between the concrete and the steel strands are modeled by a thin layer of cohesive elements with an essentially zero thickness of 7.87e-5 in. (.002 mm). Length of the cohesive element is the same as the ties length, 102 in. (2590.8 mm). Each bonding interface is modeled with 4,144 cohesive elements using 8-node three-dimensional cohesive elements (COH3D8). There is a total of eight bonding regions, resulting in a total of 33,152 cohesive elements used in the model. The mechanical properties defining the bonding characteristics are discussed in the “Materials” section.

Ballast

Three representative ballast geometries are proposed for this study. Each of the ballast cases proposed represents a different support condition that may be observed in the field. The first ballast, Ballast_1, represents the ideal “continuous support” boundary

condition. The second ballast, Ballast_2, represents the “end supports” boundary condition. The third ballast, Ballast_3, represents the “center binding support” boundary condition. The three representative ballasts were all modeled as three-dimensional deformable objects. Ballast_1, Ballast_2, and Ballast_3 are discretized into to 84,000, 66,490 (total considering both sections), and 30,870 elements using C3D8R. Ballast_1 was considered to be 23.6 in. (600 mm) wide, 15.75 in. (400 mm) high, and 110.24 in. (2,800 mm) long. Ballast_2 consists of two deformable objects with each being 24 in. (610 mm) wide, 24 in. (610 mm) high, and 43 in. (1,092.2 mm) long. Ballast_3 was considered to be 28 in. (711.2 mm) wide, 24 in. (610 mm) high, and 50.85 in. (1,291.6 mm) long. Figures (5.3-5.5) show the tie and ballast setups with their respective mesh.

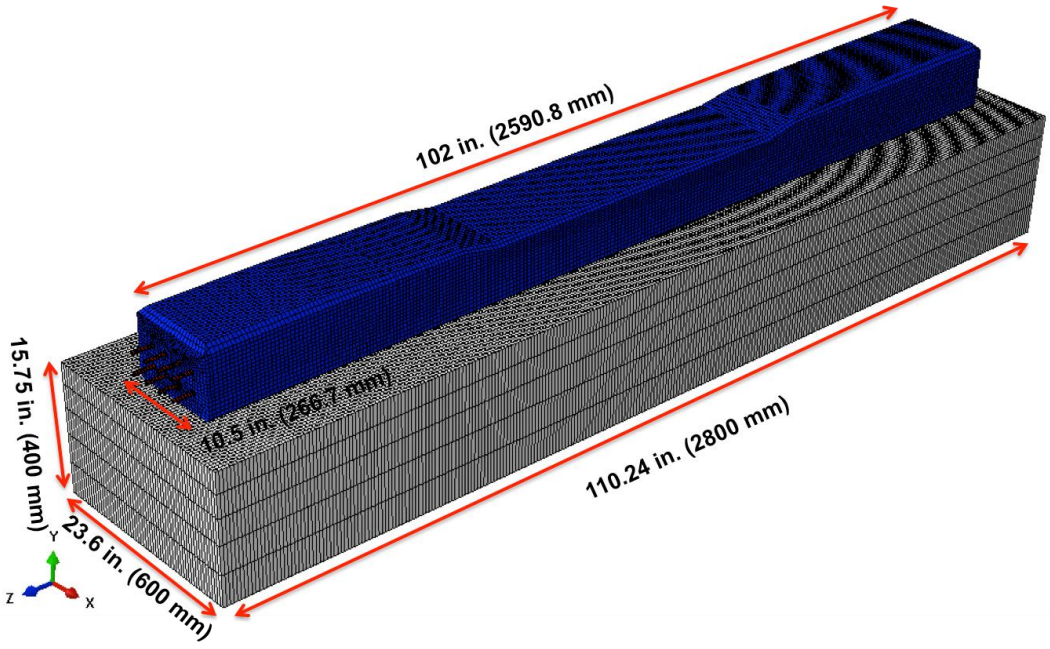

Figure 5.3: Respective mesh for the concrete tie with a continuous support (Ballast 1)

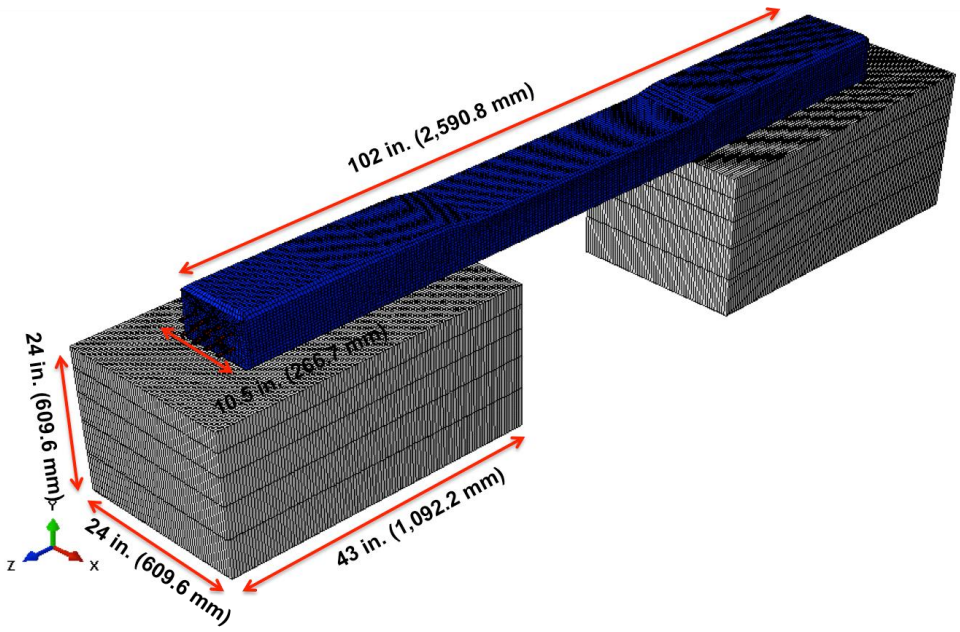

Figure 5.4: Respective mesh for the concrete tie with its ends supported (Ballast 2)

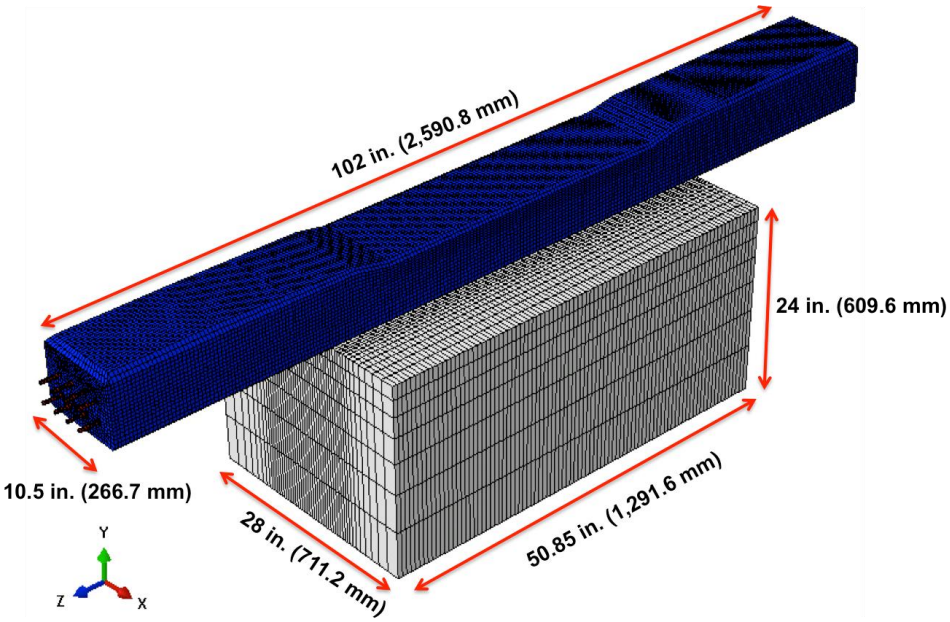

Figure 5.5: Respective mesh for the concrete tie with a center binding support (Ballast 3)

Materials

Concrete Material Models

A concrete damage plasticity model (CDP) is used in order to define the inelastic behavior of each concrete. This model assumes that the two main failure mechanisms are tensile cracking and compressive crushing (ABAQUS Theory Manual, 6.12). ABAQUS uses two hardening variables, $\tilde{\varepsilon}_t^{pl}$ and $\tilde{\varepsilon}_c^{pl}$, in order to define the progression of the stress-strain curves after the material has reached its yielding point or failure. The variables, $\tilde{\varepsilon}_t^{pl}$ and $\tilde{\varepsilon}_c^{pl}$, are referred to as the "tensile and compressive equivalent plastic strains". Figures (5.6-5.7) depict the idealized stress-strain curves used for the concrete in its compression and tensile state.

Under uniaxial compressive loading, the stress-strain curve is defined in three regions: linear elastic, strain hardening, and strain softening. The stress-strain response initially follows a linear elastic response until it reaches the initial yield stress in compression, σ_{c0}. In this study, σ_{c0} is assumed to be equal to 60% of the concretes compressive strength as seen in Eq. (1).

$$\sigma_{c0} = .6\,\sigma_{cu} \tag{1}$$

The variable, σ_{cu}, represents the ultimate compressive strength of the concrete. After the initial compressive yielding value has been reached, the stress-strain behavior progresses into a "strain hardening" phase. ABAQUS requests that the hardening data

be given in terms of inelastic strain, $\tilde{\varepsilon}_c^{in}$. The inelastic strain is defined as the total strain minus the elastic strain as seen in Eq. (2).

$$\varepsilon_c^{in} = \varepsilon_c - \varepsilon_{0c}^{el} \tag{2}$$

$$\varepsilon_{0c}^{el} = \frac{\sigma_c}{E_0} \tag{3}$$

The variables, ε_{0c}^{el} and ε_c, are the elastic strain and total strain. After the ultimate strength has been reached, a cumulatively increasing damage variable, d_c, is introduced as the curve begins to descend into the compressive softening region. The damage variable can take on values ranging from 0 to 1, where d_c=0 represents the undamaged state and d_c=1 represents complete loss of stiffness. This relationship is simply shown in Eq. (4), where E_0 is the undamaged elastic modulus.

$$E = (1 - d) * E_0 \tag{4}$$

ABAQUS implicitly converts the inelastic strain values into plastic strain values, so the user needs only to define the inelastic strains. The relationship ABAQUS uses to convert both inelastic and cracking strains into plastic strains is shown in Eq. (5). If the user does not define any damage, the inelastic strain is simply equal to the plastic strain and the model behaves merely as a plasticity model.

$$\varepsilon_c^{pl} = \varepsilon_c^{in} - \frac{d_c}{(1 - d_c)} \frac{\sigma_c}{E_0} \tag{5}$$

The process of defining the uniaxial tensile behavior of the concrete differs slightly to that of the compressive behavior in that a strain-hardening region is not

defined for the tensile case. The uniaxial tensile curve follows a linear elastic response until it reaches its tensile strength, σ_{tu}, after which, continues into a strain-softening response. ABAQUS requests that the input strains be given in terms of "cracking strain", ε^{ck}_t, which is defined as the total strain minus the elastic strain, similar to Eq. (2). A damage variable, d_t, with the same restrictions as the compressive damage variable, can also be introduced for the tensile softening region. It should be mentioned that the user might also define the post-failure stress as a function of displacement or fracture energy. Furthermore, based on the equations and methods described above, the stress-strain relationship for compressive and tensile loading can be simplified as seen in Eqs. (6-7).

$$\sigma_c = (1 - d_c)E_0(\varepsilon_c - \varepsilon_c^{pl}) \tag{6}$$

$$\sigma_t = (1 - d_t)E_0(\varepsilon_t - \varepsilon_t^{pl}) \tag{7}$$

Empirical stress-strain models were utilized in order to define the concrete's hardening and softening regions resulting from uniaxial compressive and tensile loading. Many numerical models for defining the stress-strain behavior of concrete have been previously developed and referenced (Popovic, 1973; Carreira & Chu, 1985; Hsu & Hsu, 1994). As mentioned previously, a linear elastic region followed by a strain hardening and softening region, defines the concrete's stress-strain behavior in compression. This paper assumes a linear elastic behavior up to 60% of the concrete's ultimate strength based on previous literature (Yu, Jeong, & Sussmann, 2011). The stresses in the linear elastic region are described by Eq. (8).

$$\sigma_c = E_0 \varepsilon_c,\ \varepsilon_c \leq \frac{\sigma_{c0}}{E_0} \tag{8}$$

The numerical models used to describe the strain hardening and softening regions resulting from uniaxial compressive loading are adopted from the work referenced in (Yu, Jeong, & Sussmann, 2011; Collins & Mitchell, 1991). The equation to define the stress in the strain-hardening region is as follows:

$$\sigma_c = \sigma_{c0} + \frac{E_0 \varepsilon_c - \sigma_{c0}}{1 + A\left(\frac{E_0 \varepsilon_c - \sigma_{c0}}{E_0 \varepsilon_{c0} - \sigma_{c0}}\right)^n},\ \frac{\sigma_{c0}}{E_0} < \varepsilon_c \leq \varepsilon_{cu} \tag{9}$$

The variable, ε_{cu}, represents the strain at the concrete's ultimate strength and the constants, A and n, are determined through Eqs. (10-11).

$$A = \frac{E_0 \varepsilon_c - \sigma_{c0}}{\sigma_{cu} - \sigma_{c0}} - 1 \tag{10}$$

$$n = 1 + \frac{1}{A} \tag{11}$$

Finally, the equation used to define the stress in the strain-softening region is a modified version of Popovics proposed formulation and is as follows:

$$\sigma_c = \frac{\sigma_{cu} r \frac{\varepsilon_c}{\varepsilon_{cu}}}{r - 1 + \left(\frac{\varepsilon_c}{\varepsilon_{cu}}\right)^{kr}},\ \varepsilon_c > \varepsilon_{cu} \tag{12}$$

The variables, r and k, depend on σ_{cu} and are expressed as:

$$r = .8 + \frac{\sigma_{cu}}{17} \tag{13}$$

$$k = .67 + \frac{\sigma_{cu}}{62} \tag{14}$$

It is noted that σ_{cu} must be expressed in Mpa in order to satisfy the equations for r and k. Figure (5.8) shows the compressive stress-strain curve attained from the equations listed above, when E_0=34,448 (Mpa), σ_{cu}=59.42 (Mpa), and ε_{cu}=2.17e-3, which characterize the standard material in this study.

Having now defined the compressive behavior of the concrete, one can now proceed in determining the values of the damage variable, d_c, for the descending portion of the curve. One method for defining the damage progression is to simply calculate the ratio of the stress along the declining portion of the curve to the concrete's compressive strength, as suggested by Kmiecik and Kamiński (2011). Another method is to use numerical models to calculate the plastic strain, ε^{pl}, to solve equations for d_c. This paper utilizes the first suggested method due to its relative simplicity. Figure (5.9) shows a plot of the progression of damage for an increase in inelastic strain for the previously listed example. An upper limit of .99 or 99% was set for the value of d_c as suggested in the ABAQUS User's Manual (ABAQUS User's Manual, 6.12). The purpose of this limit is to increase the rate of convergence due to the "critical effect" that excessive damage exhibits on the rate of convergence.

The idealized stress-strain curve for the concrete in uniaxial tension is slightly easier in that there is no strain-hardening region to define. The tensile curve is assumed

to be linear elastic until it reaches the ultimate tensile strength, σ_{tu}, after which the curve descends into a strain-softening phase. The linear elastic response for the tensile curve is given by the equation:

$$\sigma_t = E_0 \varepsilon_t,\ \varepsilon_t \leq \frac{\sigma_{tu}}{E_0} \tag{15}$$

Similarly to the compressive curve, the descending branch of the tensile curve was defined using empirical models. This paper uses the numerical model, for the descending branch of the tensile curve, suggested and referenced in (Calayir & Karaton, 2005; Rezaie & Farnam, 2015). The tensile stress for the descending branch is as follows:

$$\sigma_t = \sigma_{tu}\left[2e^{-a(\varepsilon_t - \varepsilon_{tu})} - e^{-2a(\varepsilon_t - \varepsilon_{tu})}\right], \varepsilon_t > \varepsilon_{tu} \tag{16}$$

The variable, ε_{tu}, is the strain corresponding to the tensile strength of the concrete. The constant, a, is dimensionless and is determined by the following relation:

$$a = \frac{3}{\varepsilon_{tu}\left[\frac{2E_0 G_f}{I_{ch}\ {\sigma_{tu}}^2}\right]} \geq 0 \tag{17}$$

The above equation introduces two more variables, I_{ch} and G_f. I_{ch} is termed the "characteristic length" and is a geometrical constant presented as a measure of the length of the fracture process zone. G_f is simply the fracture energy per unit area. The term I_{ch} is calculated as

$$I_{ch} = \frac{E_0 G_f}{{\sigma_{tu}}^2} \tag{18}$$

The fracture energy needed to open a unit area of crack was calculated by averaging the following two equations ("Phillips & Binsheng, 1993; Abdelatif, Owen, & Hussein, 2015).

$$G_f = 43.2 + 1.13\ \sigma_{cu} \tag{19}$$

$$G_f = 30.5 + 6.64\ \sigma_{tu}{}^2 \tag{20}$$

Both, σ_{cu} and σ_{tu}, must be in Mpa and G_f is in N/m. With the fracture energy now known, one can calculate the stresses for the descending curve. Figure (5.10) shows the idealized tensile stress-strain curve of the previously mentioned example based on the equations mentioned above. Finally, the damage variable, d_t, is calculated applying the same method used in calculating d_c.

Aside from defining the two stress-strain curves (tensile and compressive), there is an additional five variables that are needed to fully define the CDP model: dilation angle, eccentricity, σ_{b0}/σ_{c0}, K_c, and a viscosity parameter. The dilation angle, ψ, is measured in the p-q plane at high confining pressure. In literature, ψ is usually defined between 30-40° for the concrete (Kmiecik & Kamiński, 2011; Jankowiak & Łodygowski, 2005). A value of ψ = 36° is used for the dilation angle in this study. The variable, ε or eccentricity, defines the rate at which the flow potential function approaches the asymptote. ABAQUS sets a default value of ε = .1, which is utilized in this study. The variable, σ_{b0}/σ_{c0}, describes the ratio of the initial equibiaxial compressive yield stress to the initial uniaxial compressive yield stress. This study uses the ABAQUS default value of σ_{b0}/σ_{c0} = 1.16. The variable K_c is interpreted as the ratio of the second stress invariant on the tensile meridian to that on the compressive meridian. Again, this study adopts

the ABAQUS recommended default value of K_c = 2/3. Finally, a small value for the viscosity parameter, μ, can be specified in order to increase the rate of convergence. This study adopts a viscosity parameter of μ = .0001. The meaning and importance of each of these variables has been studied and explained extensively in literature and the ABAQUS Theory Manual (Lubliner, Oliver, & Oñate, 1989; ABAQUS Theory Manual, 6.12). The values used for defining the CDP model are summarized in Table (5.1).

Table 5.1: Values used for defining the parameters in the CDP model

Dilation Angle, ψ	Eccentricity, ε	σ_{b0}/σ_{c0}	K_c	Viscostiy Parameter
36°	0.1	1.16	0.667	0.0001

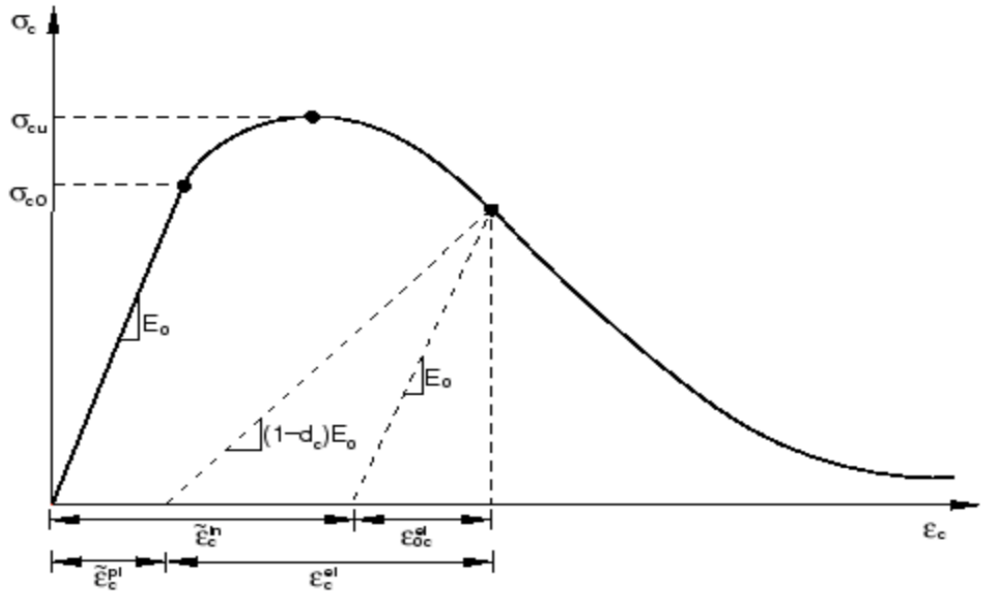

Figure 5.6: Idealized uniaxial compressive stress-strain curve for the CDP model (ABAQUS User's Manual, 6.12)

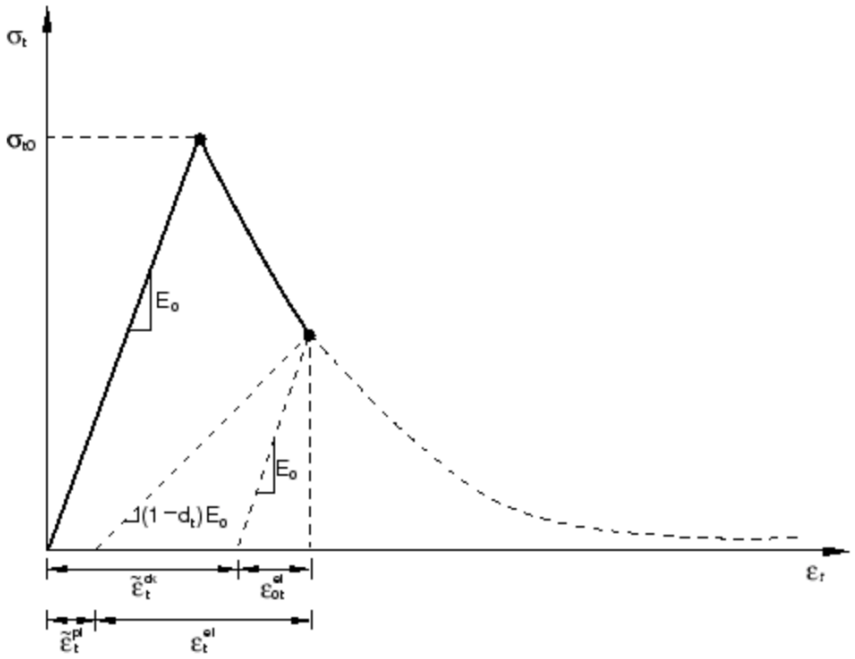

Figure 5.7: Idealized tensile curve for the CDP model (ABAQUS User's Manual, 6.12)

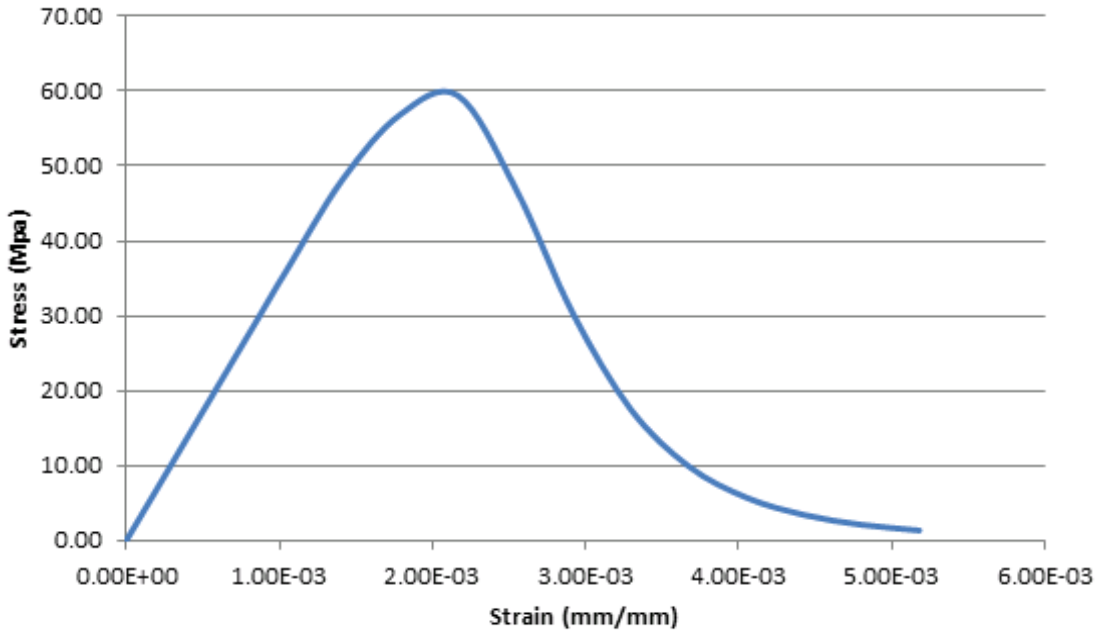

Figure 5.8: Example compressive stress-strain curve for a concrete with σ_{cu} = 59.42 (Mpa), E_0 = 34,448 (Mpa), and ε_{cu} = 2.17e-3

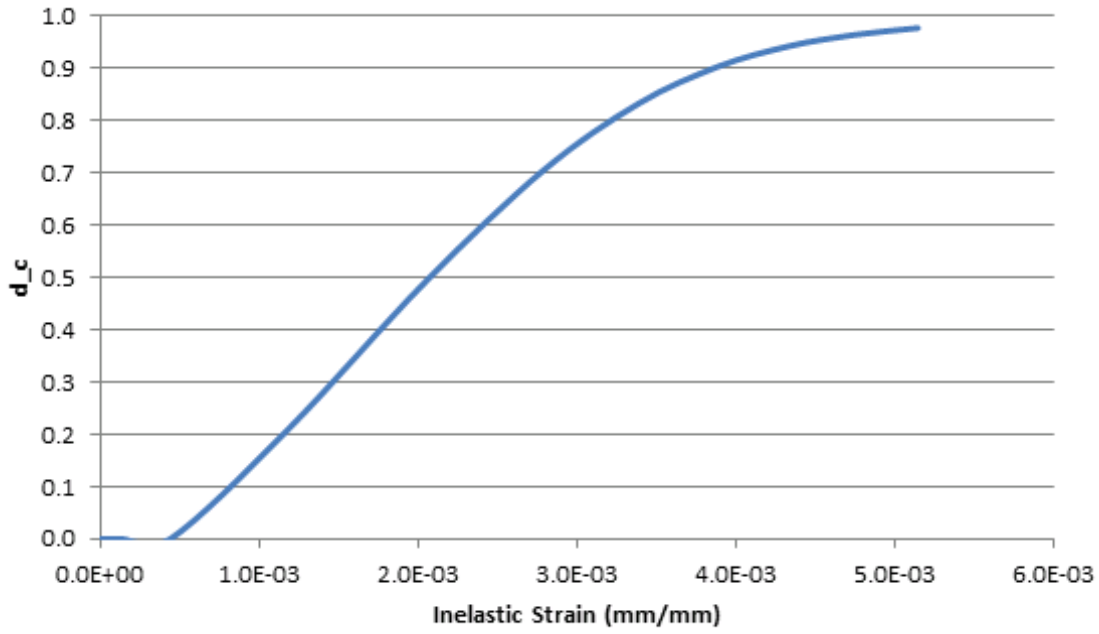

Figure 5.9: Graph of compressive damage, d_c, vs inelastic strain

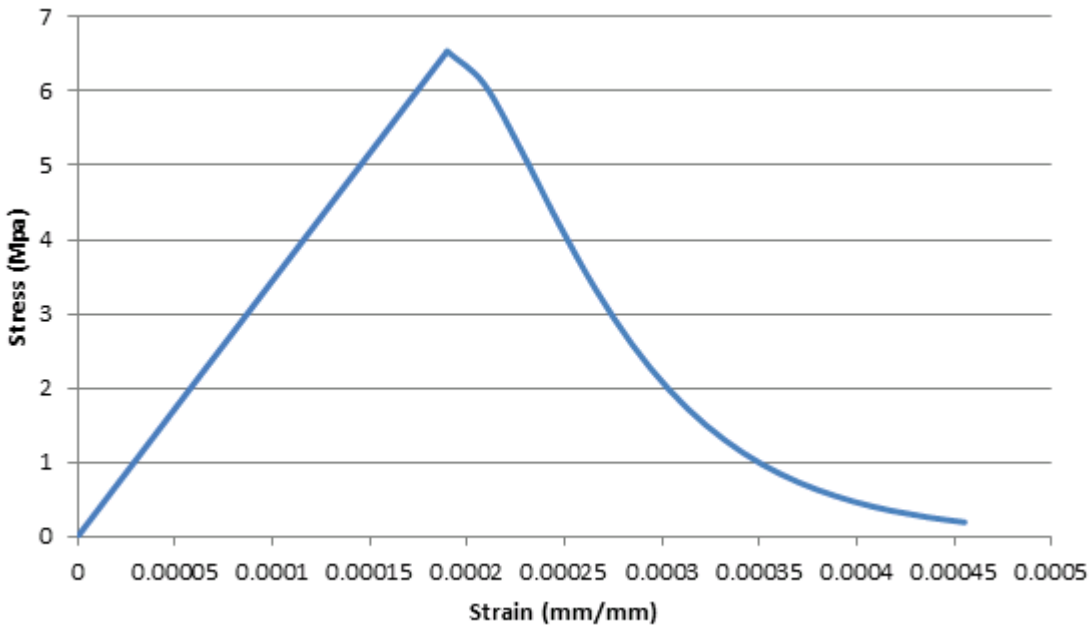

Figure 5.10: Example tensile curve for the CDP model

Concrete-Steel Interface Material Models

It is well documented that the three main bonding mechanisms between the concrete and steel strands are due to adhesion, friction, and mechanical interlocking between the two materials. In particular, bonding due to adhesion refers to both the physical and chemical bonding at the molecular level and is only present when there is no relative slipping between the concrete and the steel strand. The contribution of the adhesive bond to the overall bond is often considered to be relatively small. Friction between the steel and concrete is the second bonding mechanism. In particular, when the steel strands are initially tensioned, before the concrete has been poured, the original diameter reduces at a rate that is dependent on the steels Poisson's ratio. After the concrete is poured and has reached a predetermined strength, the strands are released, and the steel will attempt to expand back to its original diameter; however, the expansion is restricted by the surrounding concrete. This causes the steel to introduce a radial or normal force to the concrete, thus introducing a longitudinal frictional force between the strand and the concrete. The confining pressure is not uniform at the tie ends and, thus, an additional wedging effect is introduced, commonly referred to as Hoyer's effect. Finally, the third bonding mechanism is mechanical interlocking, which refers to the interaction between the concrete with the helical shape/geometry of the seven-wired strand. Mechanical interlocking provides resistance to bond slippage.

Modeling the bond mechanisms follows three approaches that are most commonly used. These include a tie constraint between the concrete and strand, a

frictional interaction model between the two materials, or a thin layer of cohesive elements between the concrete and strands. Each method has its benefits and shortcomings. For example, modeling the concrete-steel bond with a tie constraint is generally the simplest approach, however it doesn't capture the bond slippage and represents a "perfect bond", which we know is not the case in the real world. On the other hand, modeling the concrete-steel bond with cohesive elements often takes more time and effort, however with this type of approach the user has more control in defining the characteristics of the bond itself, such as its elastic properties or bond strength. In an effort to develop a "more complete" model, three-dimensional cohesive elements (COH3D8) were chosen as the means to model the concrete-steel bond.

The concrete-steel interface is modeled by inserting a thin layer of cohesive elements in between the two surfaces. The top and bottom surfaces of the cohesive elements are then connected to the concrete and steel by tie constraints in ABAQUS. The cohesive elements are then assigned with a traction-separation constitutive behavior. The stress-displacement behavior is as follows:

$$\begin{Bmatrix} \boldsymbol{\sigma}_n \\ \boldsymbol{\sigma}_s \\ \boldsymbol{\sigma}_t \end{Bmatrix} = \begin{bmatrix} K_{nn} & K_{ns} & K_{nt} \\ K_{ns} & K_{ss} & K_{st} \\ K_{nt} & K_{st} & K_{tt} \end{bmatrix} \begin{Bmatrix} \boldsymbol{\delta}_n \\ \boldsymbol{\delta}_s \\ \boldsymbol{\delta}_t \end{Bmatrix}$$

where σ_n is the stress in the normal direction and the stress in the two shear directions are σ_s and σ_t. The variable, K, represents the elastic stiffness parameter (force/length^3) and δ is the displacement. The uncoupled condition is assumed, which means all of the stiffness terms are equal to zero, except for the diagonal terms K_{nn}, K_{ss}, and K_{tt}.

Additionally, the shear plane is assumed to be isotropic, implying that $K_{ss} = K_{tt}$. Once the cohesive elements elastic properties are defined, one can proceed in describing the damage initiation and evolution of the material.

The damage initiation refers to the point at which degradation of the cohesive action begins and is dictated by the particular damage initiation criteria that is selected. Degradation of the cohesive element begins when stresses or separations satisfy the damage initiation criteria. ABAQUS provides the user with four different choices for defining the damage initiation criteria: maximum stress, maximum separation, quadratic stress, and quadratic separation criteria. The maximum stress criterion is chosen in this study and is expressed by the following equation:

$$max\left\{\frac{\langle t_n \rangle}{t_n^0}, \frac{t_s}{t_s^0}, \frac{t_t}{t_t^0}\right\} = 1$$

where t^0_n, t^0_s, and t^0_t are the peak values of the contact stress when the separation is purely normal to the interface. The maximum stress criterion assumes that damage has initiated if the stress ratio reaches one, and, from this point onward, the cohesive element's stiffness is degraded at a rate that is defined by the assumed damage evolution law. A linear damage evolution is chosen in this study, an idealization of which is depicted in Figure (5.11). After the damage initiation criterion is satisfied, the linear damage evolution law states that the degradation of the cohesive element will increase linearly until its complete failure at the failure displacement, δ^f_m. Furthermore, a frictional interaction was applied to the concrete and steel strand surfaces to simulate the friction between the steel and concrete. This interaction will only activate if there is

complete degradation of the cohesive element. Due to a lack of initial data at the beginning of the simulations, the elastic stiffness values for the cohesive elements have been adopted from Yu and Jeong (2015) and the bond strength values are assumed as originally reported in Abrishami and Mitchell (1993). The parameters and values used in defining the concrete-steel interaction are shown in Table (5.2). In order to validate the bond strength of 4.83 Mpa used in the model simulations untensioned pullout tests were experimentally performed on concrete specimens. It is noted that these tests were conducted after majority of the simulations were already completed. An additional finite element simulation of the strand release was performed with the experimentally determined bond strength values of 4.57 Mpa. The results are compared with the previous simulations to assess the influence of the slightly reduced measured strength, as discussed further in the "Model Validation Studies" section of Chapter 6.

Table 5.2: Parameter values used for defining the concrete-steel interface

K_{nn}	$K_{ss} = K_{tt}$	δ^f_m	Bond Strength	Friction Coefficient
92,630,000 lb/in^3 (25,144.1 N/mm^3)	385,958 lb/in^3 (104.8 N/mm^3)	2 in. (50.8 mm)	701 psi (4.83 Mpa)	0.3

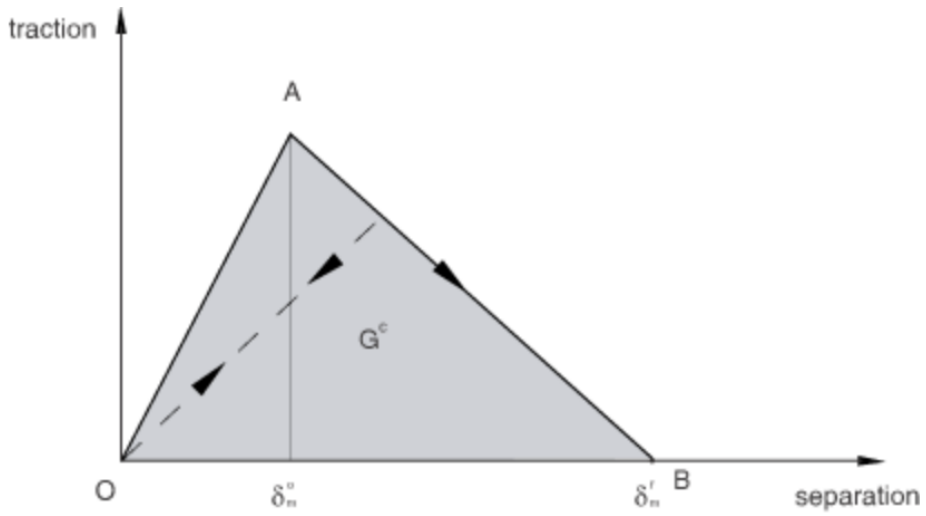

Figure 5.11: Idealized linear damage evolution law defined by ABAQUS (ABAQUS User's Manual, 6.12)

Steel Material Model

The steel strands are assumed to be linear elastic with a modulus of elasticity of E=30,000 ksi (206,843 Mpa). This is an appropriate assumption, as yielding and nonlinear behavior of the steel is not expected in these simulations. Additionally, each strand is assigned a value for Poisson's ratio of ν=0.29.

Ballast Material Model

The representative ballast is assumed to be linear elastic in this initial study. The elastic modulus of the ballast material has previously been modeled by Desai and Siriwardane (1982), as well as Li and Ernest (1995), as cited by Kumaran, Menon, and

Nair (2002), to be ranging from 100 Mpa to 350 Mpa. An elastic modulus of E=29,000 psi (200 Mpa) and Poisson's ratio of ν=0.3 is assumed for all three ballast models.

Loads and Boundary Conditions

Loading Scenarios

The tie is subjected to three loading conditions. The first case pertains to the loading that simulates the prestressing applied during the fabrication process. The second case refers to vertical loading for either the validation studies through testing, or the simulated axle load in a tangent track. The last case pertains to simulated loads in a curved track and consists of lateral loads applied simultaneously with the aforementioned vertical simulated loads. The three loading scenario are discussed next.

Prestressing: In the manufacturing process for producing prestressed concrete, the steel strands are first tensioned, by a jacking system, to the desired initial stress before any concrete has been poured. Next, the concrete is poured into the forms, encompassing the strands and left to cure until the concrete has reached the necessary strength to release the strands. After the concrete has reached the required strength, the pretension in the strands is released, thus transferring the tensile stresses from the strands as compressive stresses in the concrete through the steel-concrete bond. This general approach in fabricating the prestressed concrete ties is simulated in the finite element models by applying a predefined stress field equivalent to the pretension stress. In this study, the 3/8" (9.525 mm) diameter strands are tensioned with an initial

force of 17.25 kips (76,731 N), which corresponds to an initial predefined stress in each strand of approximately 156 ksi (1,076 Mpa).

Validation Study: The validation study pertains to a Four Point Flexural Bending Test. In this study, the tie is tested upside down and thus the loading is applied at the bottom of the tie and supported at the top of the tie. The concrete ties were experimentally loaded as shown in Figure (4.1) and were observed to fail at a total load between 76-80 kips. Accordingly, a total load of 80 kips (355.86 kN) is applied to the tie in the simulations. Two 40 kip (177.93 kN) loads are applied to the bottom of tie as uniform pressures over relatively small area, as seen in Figure (5.12). This is done to prevent any convergence issues that might arise because of a large magnitude load that is concentrated at a few nodes.

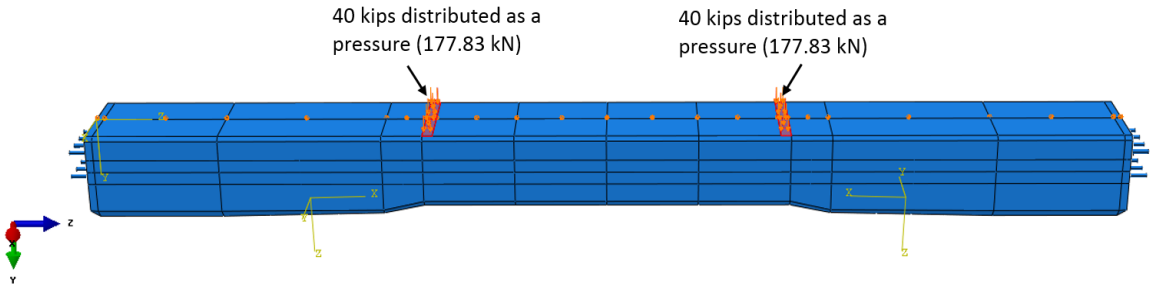

Figure 5.12: Depiction of loading for the FE Four Point Bend Test model

Simulated Track Loads: Vertical loads are applied at the rail seats as pressures over the entirety of each rail seat area and are assumed uniform. The vertical load per rail seat in

each case is equal to 40 kips (177.93 kN). The simulations in this work focus on the global performance of the tie and do not consider local effects in the rail seats. Therefore, although it is well established that the load distribution over the rail seat area is not uniform, the assumption is reasonable and is not expected to affect the results. It is also noted that it is not necessary to account for the fastening system for this level of modeling and the objectives of the simulations. Similarly to the vertical loads, the lateral forces (L) simulating loading on a curved track are applied as uniformly distributed horizontal force on the field side rail seat in proportion to the vertical loads (V) corresponding to a ratio L/V=0.6 or a resultant lateral force of 24 kips (106.76kN).

Boundary Conditions

In view of the loading scenarios and the objectives of the simulations a number of different boundary conditions are considered and discussed next.

Prestress Release: In the simulation of the release of the prestressing and in order to avoid rigid body motion of the tie, the tie is minimally supported by constraining: (a) the displacements in the longitudinal direction of all nodes on the perimeter of the cross section at the midspan; (b) the vertical displacement at two points on the neutral axis on each side of the midspan offset by a small distance; (c) and the transverse displacement at three points located on a line along the length of the bottom face of the tie placed at the mid-width. These conditions are shown in Figure (5.13). Once the release of the prestressing is completed, these boundary conditions are removed.

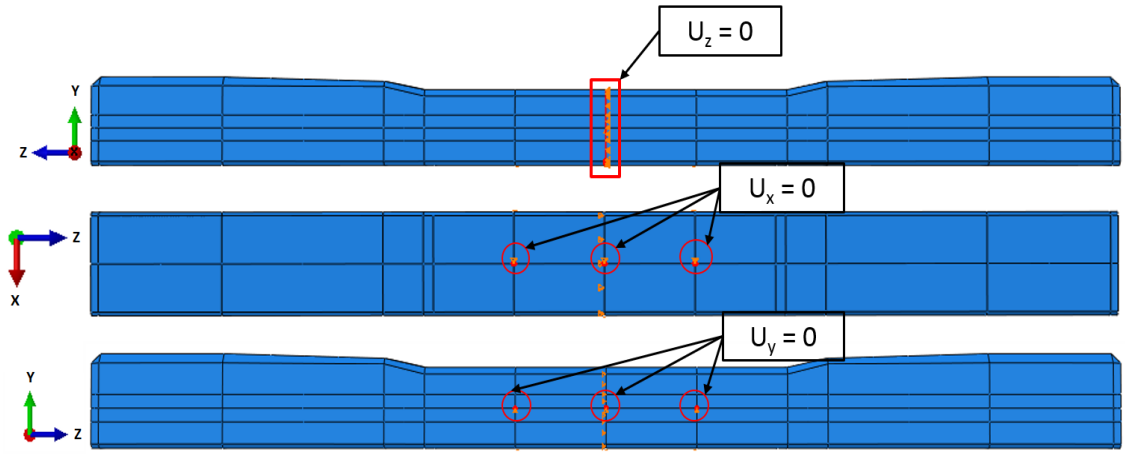

Figure 5.13: Applied boundary conditions for the prestress release step

Validation Study: The validation study pertains to a Four Point Bending Test. In this case, the tie is tested upside down and the tie is supported along a series of nodes at each rail seat. A local coordinate axis is defined for the supported nodes at each rail seat so that the X-axis is parallel and the Z-axis is perpendicular to the rail seat surface. Displacements are restricted at these nodes along the Z-axis of the locally defined coordinate axis. Additionally, the transverse displacements are constrained on a line along the length of the bottom face of the tie placed at the mid-width. This transversal constraint is also activated during the simulated track loading simulations. Figure (5.14) illustrates the applied boundary conditions for the loading phase of the Four Point Bending Test.

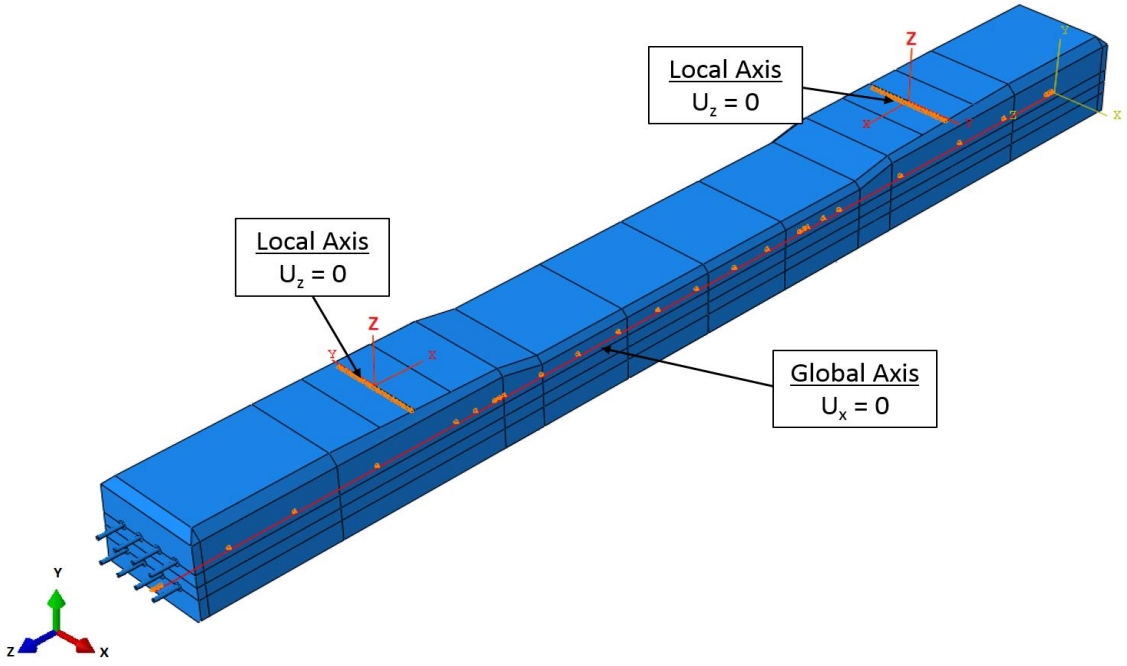

Figure 5.14: Applied boundary conditions for the loading phase of the FE Four Point Bending Test

Simulated Track Loading: In these simulation studies, the boundary conditions pertain to the ballast support. Ballast is fixed in all directions at all points at its base. The tie-ballast interface is modeled by defining a surface-to-surface contact. The interaction between the tie and the ballast contains a normal and tangential defined behavior. The normal behavior is defined as a "hard" contact, which does not allow any penetration of surfaces, allows for separations between the contact surfaces should they arise, and is the default "pressure-overclosure" relationship used by ABAQUS. The tangential behavior is defined with a penalty friction formulation with a friction coefficient $\mu = 0.5$. Figure (5.15) depicts the boundary conditions applied during the simulated track loading

studies. Finally, the transversal constraint, previously described in the validation studies, is activated for the simulated track loading cases.

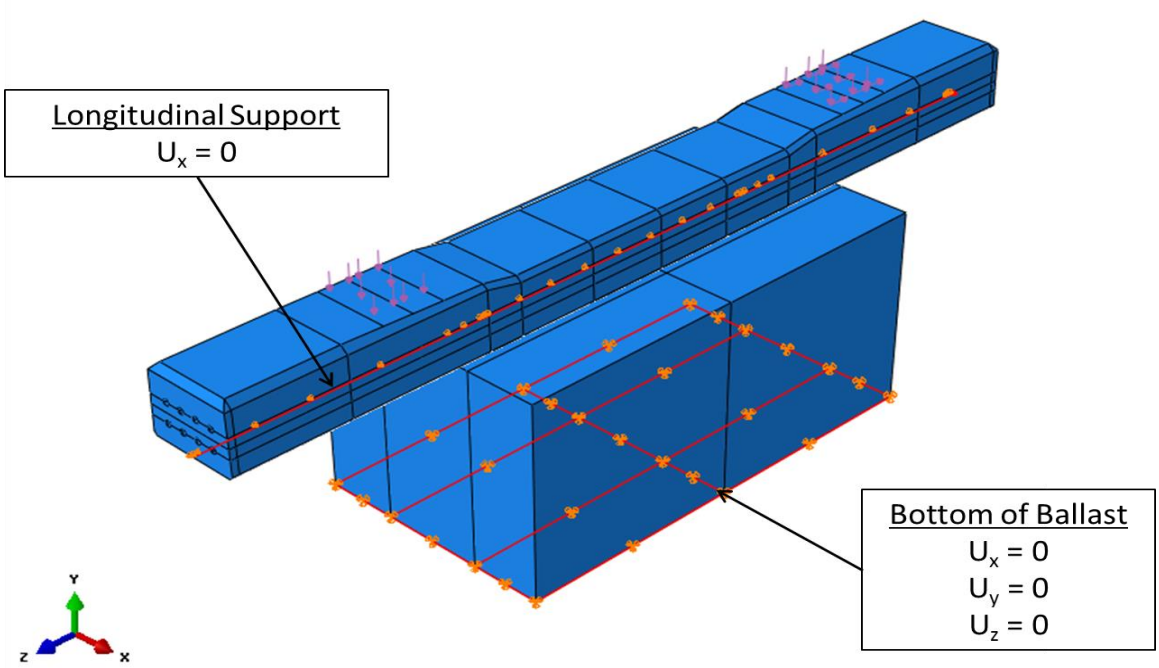

Figure 5.15: Boundary conditions applied to the tie and ballast during the "Apply Load" analysis step

Solution Procedure and Analysis Steps

The general solution procedure in ABAQUS consists of defining a sequence of solution steps with the capability to restart the solution at any step provided that a "restart option" is predefined and the solution at previously executed steps is appropriately stored and available. Each solution step in the simulations considered in this work is typically associated with changes in loading or boundary conditions, or to control the nonlinear analysis and the solution algorithms.

Initial Step: ABAQUS always requires an "Initial Step", which cannot be renamed, deleted or edited. This step is not an analysis step, however its purpose is to allow the user to apply any boundary conditions, predefined fields, and/or interactions before any loading is applied. In the initial step, the predefined stress field in the steel strands is defined. It is noted that any boundary conditions defined at this point may be deactivated and reactivated at subsequent analysis stages.

Prestressing Release: The first analysis step simulates the strand release for the prestressed concrete. The solution provides the state of stress in the concrete tie that corresponds to the tie as shipped from the tie manufacturer. The solution also provides insight into the transfer length between the steel and concrete. The representative ballast is not activated in the "Strand Release" step. This is accomplished by defining a "*Model Change*" type interaction, which suppresses the ballast elements for the duration of this analysis step. Furthermore, the "Direct" equation solver method and the "Full Newton" solution technique are used in all of the static steps (Figure (5.16)), which are the default values for ABAQUS. These methods are sufficient for this phase of the model even though some nonlinearities are expected to develop at the tie ends due to bond deterioration and concrete damage from the high stresses encountered during the transferring of the tensile stresses in the steel to compressive stresses in the concrete. Finally, this step is always performed first before any applied loading cases are considered.

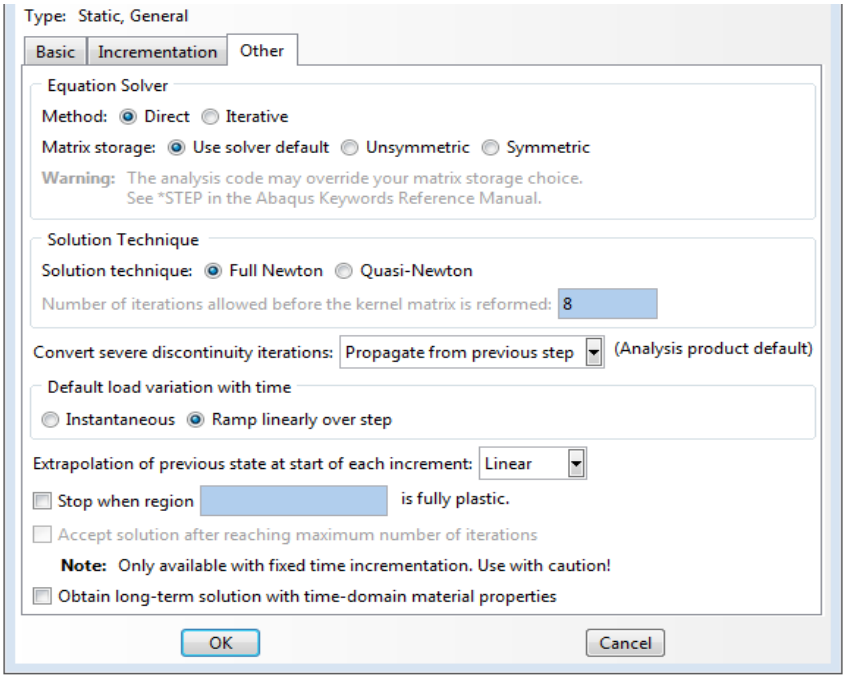

Figure 5.16: Solution parameters used for the general static analysis (ABAQUS, 6.12)

Validation Study: This analysis step represents the static nonlinear solution for the Four Point Bending Test on the tie. In this step all of the relevant forces and boundary conditions are applied. This test is expected to encounter severe damage as the tie approaches its failure, so "*Restart Request*" data is requested in case the general static analysis proves to be insufficient at providing a reasonable convergence rate. Using a restart request, ABAQUS saves the stresses at the previously terminated general static step and allows the user to import theses conditions into a new analysis step as the initial condition, ensuring that the newly restarted analysis step has the same initial stresses and displacement at its beginning that are identical to the those at the terminated increment. Thus, the remaining load left over from the previously

terminated step is applied in the new step. After preliminary simulation runs, it was quickly observed that the Riks method showed a better convergence rate once the tie encountered severe nonlinearities and crack formations. Based on these findings, the linear region of the simulation is run as a general static analysis step, with the solution parameters shown in Figure (5.16), and the nonlinear region of the simulation is restarted as a new step utilizing the Riks method, with the default solution parameters suggested by ABAQUS (Figure (5.17)). More information on the Riks method and model restarts is discussed in detail in the ABAQUS User's Manual (ABAQUS User's Manual, 6.12).

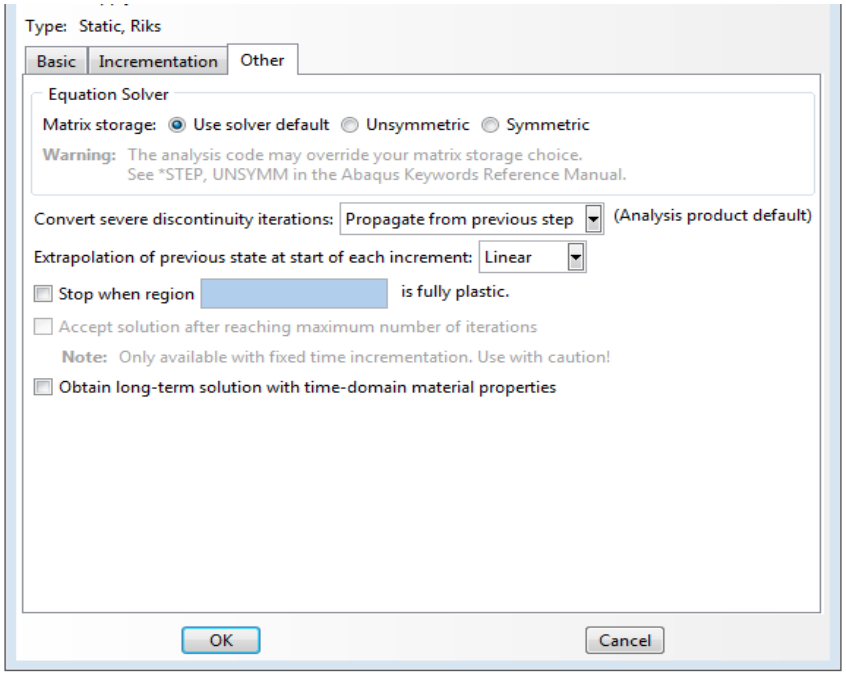

Figure 5.17: Solution parameters used for the Riks analysis step (ABAQUS, 6.12)

Applied Loading: This analysis step represents the static nonlinear solution of the loaded tie. In this step all of the relevant forces and boundary conditions (including ballast supports) for the particular test are applied, as appropriate. The representative ballast that was deactivated during the "Strand Release" step is now engaged and its interaction with the tie activated through another "*Model Change*". All ballast cases, except the center binding case (Ballast_3) showed relatively mild nonlinear behavior with little or no damage and were completed successfully using the static nonlinear analysis. However, in the center binding case severe damage was detected and the static approach showed a very slow convergence rate. Therefore, it was deemed necessary to introduce an additional analysis step that activated the Riks method to calculate solutions when extended damage was encountered. To this end, a model restart is performed, in which the remaining load from the previously terminated step is then applied in the new Riks step. The solution parameters used in the general static step and the Riks step are the same as what's shown in Figures (5.16-5.17).

Chapter 6: Results and Discussion

An experimental Four Point Bending Test is performed on the standard concrete tie to validate the finite element models. Additionally, an experimental untensioned pullout test is performed on a concrete specimen to determine and confirm the bond strength used in the finite element material model for the concrete-steel interface. The experimental and simulated results for these tests are presented and discussed in this Chapter. Furthermore, results from each of the three proposed support conditions (continuously supported, end supported, and center binding support), with their corresponding loading scenarios (L/V=0 & L/V=0.6), are presented and discussed in detail. The performance of the standard and HSRM tie are critically examined and compared for each loading and supporting case.

Model Validation Studies

A Four Point Flexural Test is performed experimentally on the standard concrete tie in order to serve as a benchmark case for the validation of the finite element model. The experimental setup is shown in Figure (6.1). The tie is loaded at a loading rate of 5 5 kips/min until its ultimate failure at a total load of 76 kips. Data is recorded continuously throughout the entirety of the test using the stereo DIC technology. Also, LVDT's and

strain gauges are positioned along the top side of the concrete tie in order to measure strains and displacements at, and in the vicinity of the midspan. The LVDT's are removed after 47 Kips of applied load in order to ensure that they will not be damaged during the tie's failure. After the concrete tie has failed, cylindrical concrete specimens are cored out of the failed specimen at both of its ends and tested for strength and elastic modulus. Figure (6.2) shows one of the failed concrete tie specimens with holes at its ends after the coring process has been completed. The average elastic modulus for the standard concrete, based on three cored concrete cylinders tested in uniaxial compression, is found to be 34,448.33 Mpa (4.99×10^6 psi) with a compressive strength of 59.42 Mpa (8,618 psi). Additionally, the tensile strength of the concrete is found to be approximately 6.54 Mpa (948 psi). These values are used in the material models for the finite element simulations. The midspan displacements from both the experimental and finite element analysis are plotted in Figure (6.3). It is observed that the finite element model seems to predict slightly higher displacements at the ties midspan. Also, the predicted crack pattern that is obtained from the finite element simulations at a load of 50 kips is compared to the cracks observed experimentally using the DIC method. This comparison is shown in Figure (6.4), where the red lines represent cracks in the finite element model. Overall, the finite element model appears to agree reasonably well with the experimental results, thus concluding that the finite element model is adequate for the proposed simulation scenarios.

As mentioned in the "Concrete-Steel Interface Material Models" section of Chapter 5, untensioned pullout test was performed, after majority of the simulations

were already run, in order verify that the cohesive strength of 4.83 Mpa used for the steel-concrete interaction is appropriate. It should be noted that this test is performed on a HSRM concrete specimen. The results from this test are shown in Figure (6.5). Bond failure is defined at 2 mm (.08 in) of strand slippage, which yields a bond stress of approximately 4.57 Mpa (662 psi). This value is also considered in the material model for the cohesive elements and a simulation of the strand release is performed. The results from the test using the bond strength of 4.57 Mpa is compared to the previous simulations using the bond strength of 4.83 Mpa in order to further ensure that the previously simulated models are valid. Longitudinal stress, S_{33}, and tensile damage parameter, d_t, are plotted at the level of bottom strands at the steel-strand interface, as seen in Figures (6.6-6.7). The results show very little difference between the two models. The model using a cohesive strength of 4.83 Mpa seems to have slightly higher stress (approximately 1% higher) at the level of the strands, where as the model with a cohesive strength of 4.57 Mpa has slightly higher initial damage at the strand ends. Due to the very similar results from both models, there is not enough variation to warrant a re-run of the previously simulated models. It is understood that it may be beneficial to perform future calibrations for the bond strength of HSRM and standard concrete models separately.

Figure 6.1: Experimental setup for the Four Point Bend Flexural Test

Figure 6.2: Image of a failed concrete tie with its ends cored out for testing

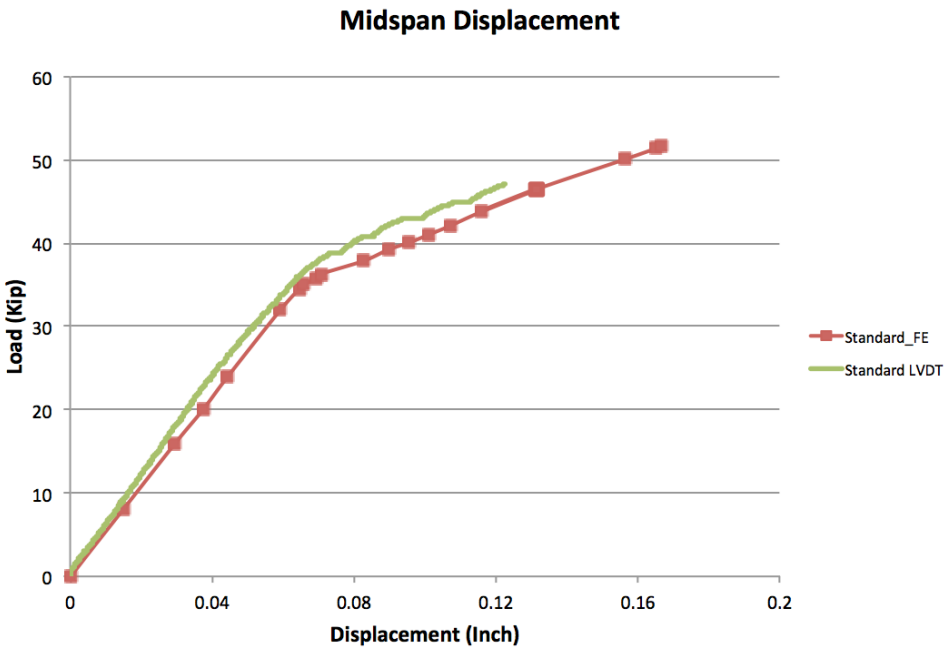

Figure 6.3: Experimental Vs FE load-displacement curves for the Four Point Flexural Bend Test at the midpoint of the tie

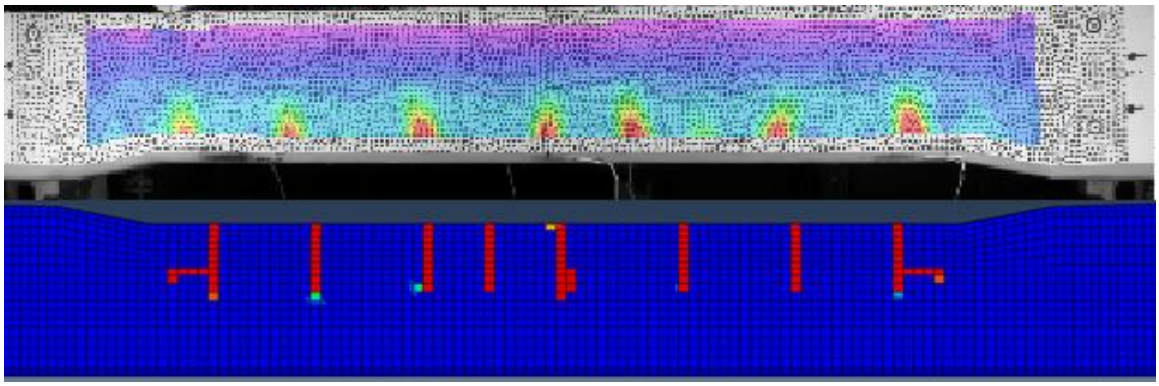

Figure 6.4: Comparison between the cracks observed experimentally and through FE simulations.

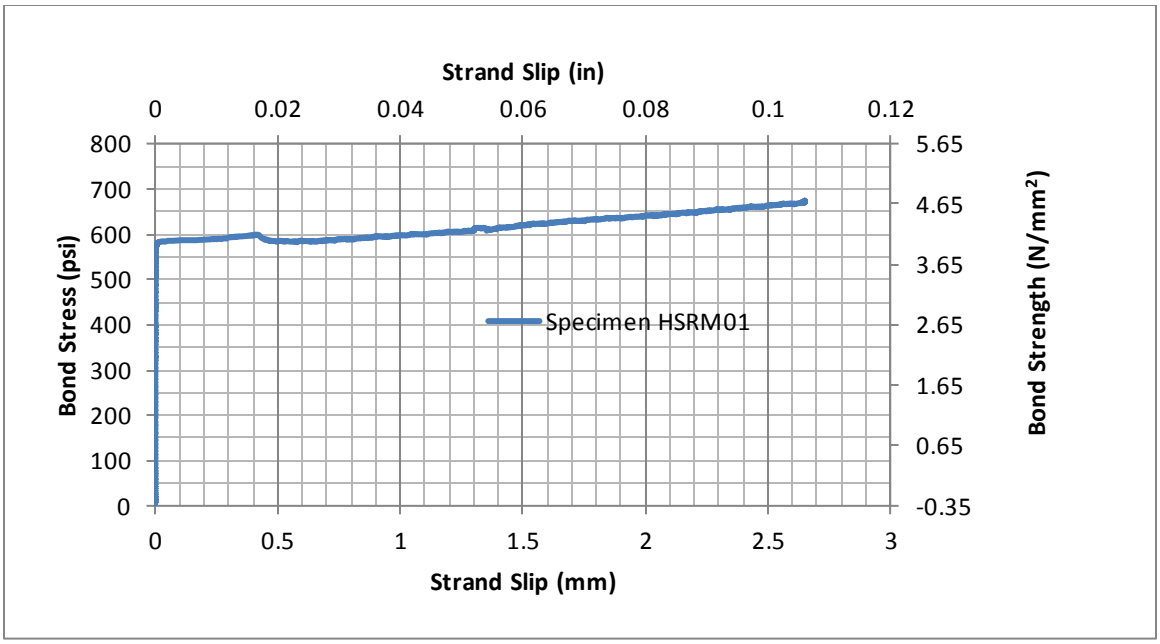

Figure 6.5: Results from an untensioned pullout test on a HSRM concrete specimen

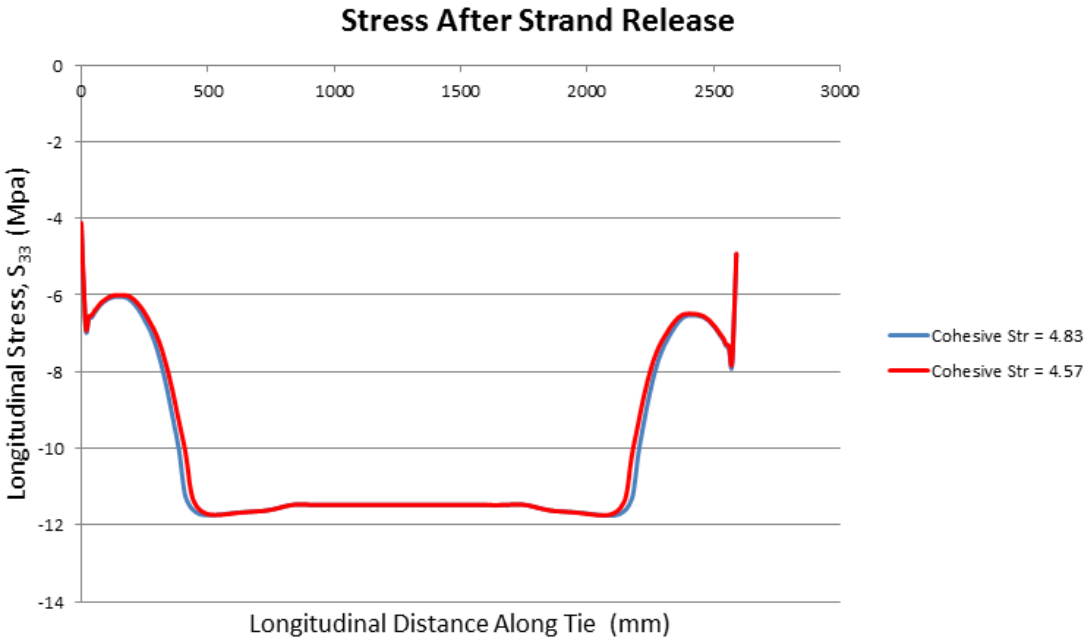

Figure 6.6: Comparison of the longitudinal stress along the distance of the tie for two different cohesive strengths. The curves plotted are acquired after the pretensioned strands have been released

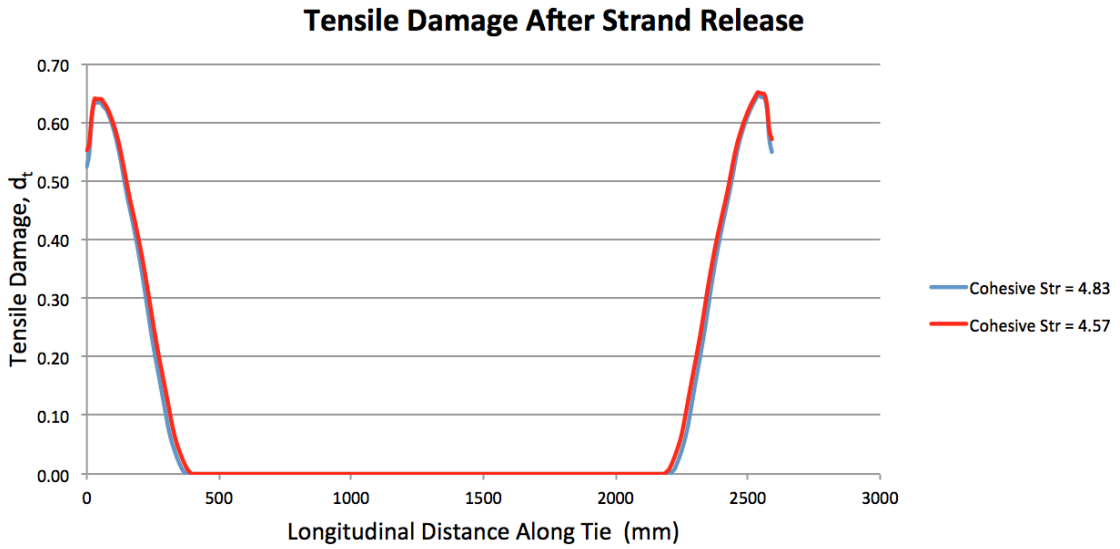

Figure 6.7: Comparison of the tensile damage observed along the distance of the tie for two different cohesive strengths. The curves plotted are acquired after the pretensioned strands have been released

Performance Under Simulated Loading & Boundary Conditions

HSRM concrete has been found to yield similar strength values to the standard concrete. Previous lab tests reveal that the average 28-day compressive strength of the HSRM concrete is approximately 63.43 Mpa (9,9197 psi) with a reduction in elastic modulus varying anywhere between 22.6% and 40%. For the purpose of comparison, the HSRM concrete material models are assumed to have the same strength properties as the standard concrete, but an elastic modulus of 26,670.00 Mpa (3.87×10^6 psi) for the 22.6% reduced case (HSRM-22.6%) and 20,669 Mpa (3.0×10^6 psi) for the 40% reduced case (HSRM-40%). The material properties that are used for the simulations are summarized in Table (6.1).

Table 6.1: Mechanical properties for each of the proposed concretes used in the FE simulations

Concrete Type	f'_c	E_c	f'_t	ν
Standard	8,618.25 psi (59.42 Mpa)	4,996,307.85 psi (34,448.33 Mpa)	948.55 psi (6.54 Mpa)	0.2
HSRM 22.6% Reduction	8,618.25 psi (59.42 Mpa)	3,868,156.5 psi (26,670.0 Mpa)	948.55 psi (6.54 Mpa)	0.2
HSRM 40% Reduction	8,618.25 psi (59.42 Mpa)	2,997,785.0 psi (20,669.0 Mpa)	948.55 psi (6.54 Mpa)	0.2

Varying Tie Support Condition

Three distinctive support conditions are considered in this study. The three supports are selected in order to simulate a concrete crosstie that is continuously supported beneath, supported at its two ends, and supported at its middle region (center binding). The representative ballast that fully supports the crosstie beneath is defined as “Ballast 1”. The representative ballast that supports the crosstie at its two ends is defined as “Ballast 2”. The representative ballast that supports the tie at its middle region is defined as “Ballast 3”. Two loading conditions, L/V = 0 and L/V = .6, are considered for each supporting case to replicate a train moving along a tangent track and a curved track. Longitudinal stress (S_{33}), von Mises stress, and tensile damage are measured throughout the crosstie and recorded for each simulation.

Continuously Supported

Load Case: L/V = 0

A 40 kip vertically applied load is distributed over each rail seat area for the L/V = 0 load case, as discussed in the "Loads and Boundary Conditions" section of Chapter 5 (Figure 6.8). The deformed shape, longitudinal stresses (S_{33}), and von Mises Stresses throughout the tie are recorded and presented in Figures (6.9, 6.11-6.20). Stress maps are superimposed onto the tie for visualization. Additionally, stresses along the top and bottom fibers of the concrete tie are measured along its length and are presented in the Figures (6.21-6.24). Figures (6.11-6.20) presented below are adjusted to the same scale for comparison.

No tensile damage is observed in the tie during the loading procedure. The three concrete ties (standard, HSRM-22.6%, and HSRM-40%) appear to be in a compressive state after 40 Kips is applied vertically to each rail seat. The deformed shape of the loaded tie shows a negative bending moment with the top middle fibers of the concrete tie having a lower magnitude of compressive stress than its bottom fibers, as seen in Figure (6.10a). Additionally, it suggests that for a case in which a larger load is applied to each rail seat, the compressive behavior seen at the top middle region of the tie will continue to decrease and shift towards a tensile behavior. In contrast, the compressive behavior seen in the bottom of the tie will continue to increase. Therefore, of the three concrete ties simulated using the Ballast 1 support and L/V = 0 loading, the tie with

higher compressive stresses in its top fibers and lower compressive stresses in its bottom fibers is the most preferred one.

The longitudinal stress (S_{33}) measured at the middle top fibers of the standard, HSRM-22.6%, and HSRM-40% concrete tie is -839.6 psi (-5.79 Mpa), -880.2 psi (-6.07 Mpa), and -913.7 psi (-6.3 Mpa). The longitudinal stress (S_{33}) measured at the middle bottom fibers of the standard, HSRM-22.6%, and HSRM-40% concrete tie is -2,393.1 psi (-16.5 Mpa), -2,297.3 psi (-15.84 Mpa), and -2,194.9 psi (-15.13 Mpa). The von Mises Stress measured at the middle top fibers of the standard, HSRM-22.6%, and HSRM-40% is 841.2 psi (5.8 Mpa), 881.8 psi (6.08 Mpa), and 915.6 psi (6.31 Mpa). The von Mises Stress measured at the middle bottom fibers of the standard, HSRM-22.6%, and HSRM-40% is 2,378.6 psi (16.4 Mpa), 2,284.6 psi (15.75 Mpa), and 2,183.7 psi (15.06 Mpa). Both the HSRM-22.6% and HSRM-40% concrete tie appear to outperform the standard tie, with the HSRM-40% showing the most desirable response, by better distributing the stresses throughout the tie. For the HSRM-22.6% concrete tie, a 4.0% increase and a 4.83% decrease in the compressive stresses were observed at the center top and bottom fibers of the concrete tie, when compared to the standard tie. For the HSRM-40% concrete tie, an 8.28% increase and an 8.76% decrease in the compressive stresses seen at the center top and bottom fibers of the concrete tie were observed, when compared to the standard tie.

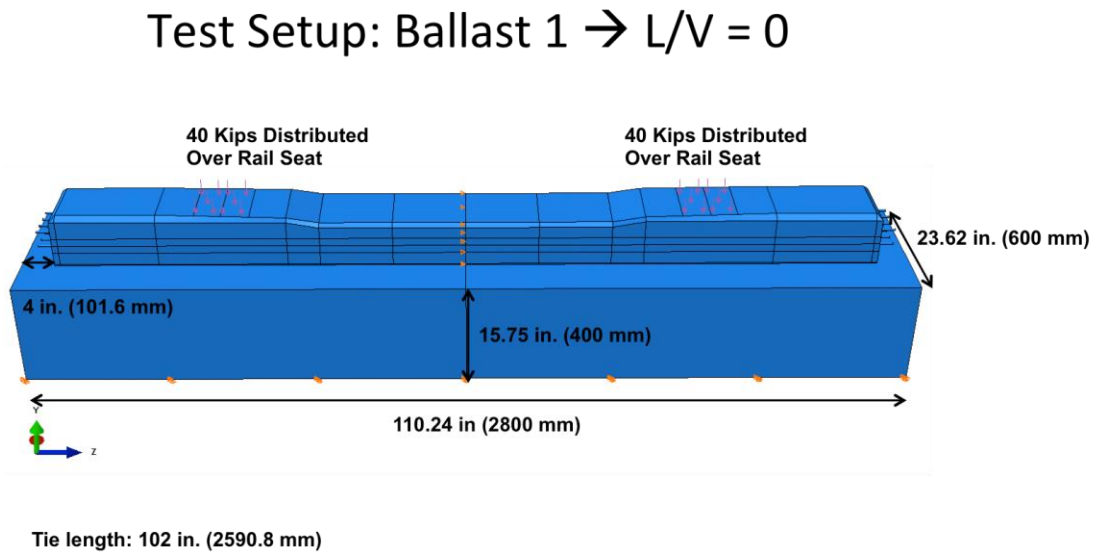

Figure 6.8: Test setup for the continuously supported tie with the load case of L/V = 0

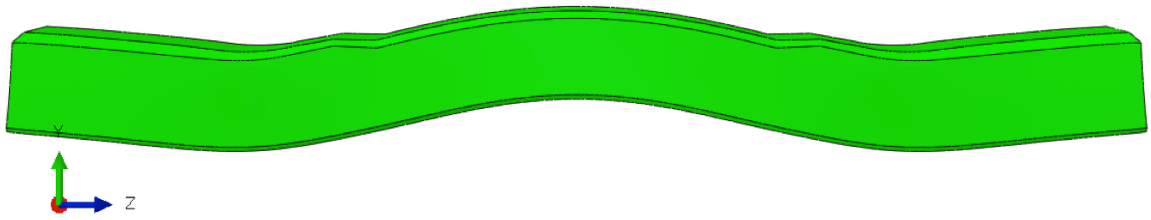

Figure 6.9: Deformed shape of the concrete tie for the continuously supported tie with the L/V = 0 load case

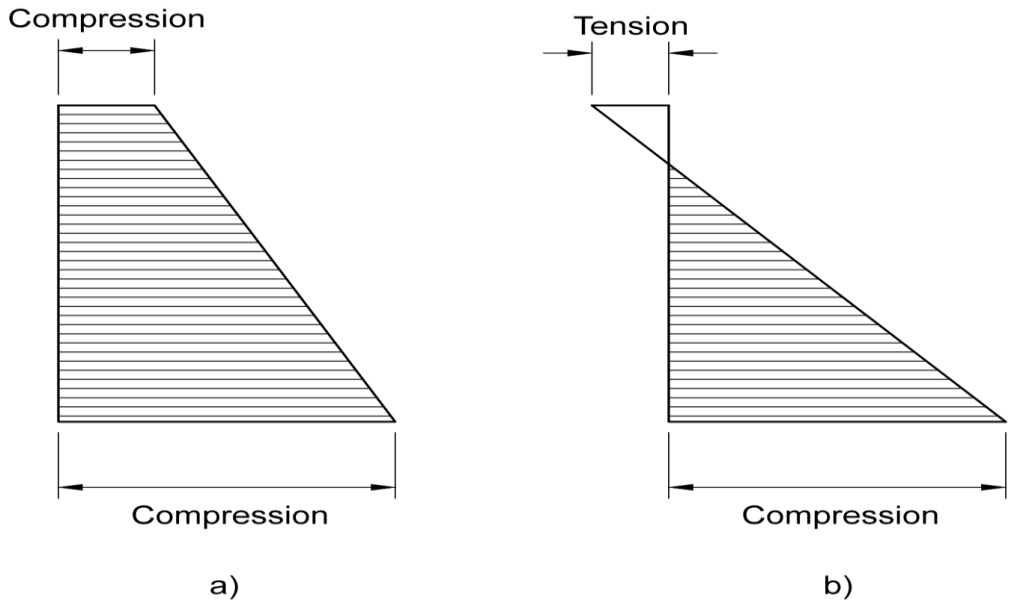

Figure 6.10a & 6.10b: a) Idealized stress distribution for the concrete tie after 80 kips of load has been applied to the rail seat. b) Hypothetical stress distribution if additional load is applied beyond the 80 Kips

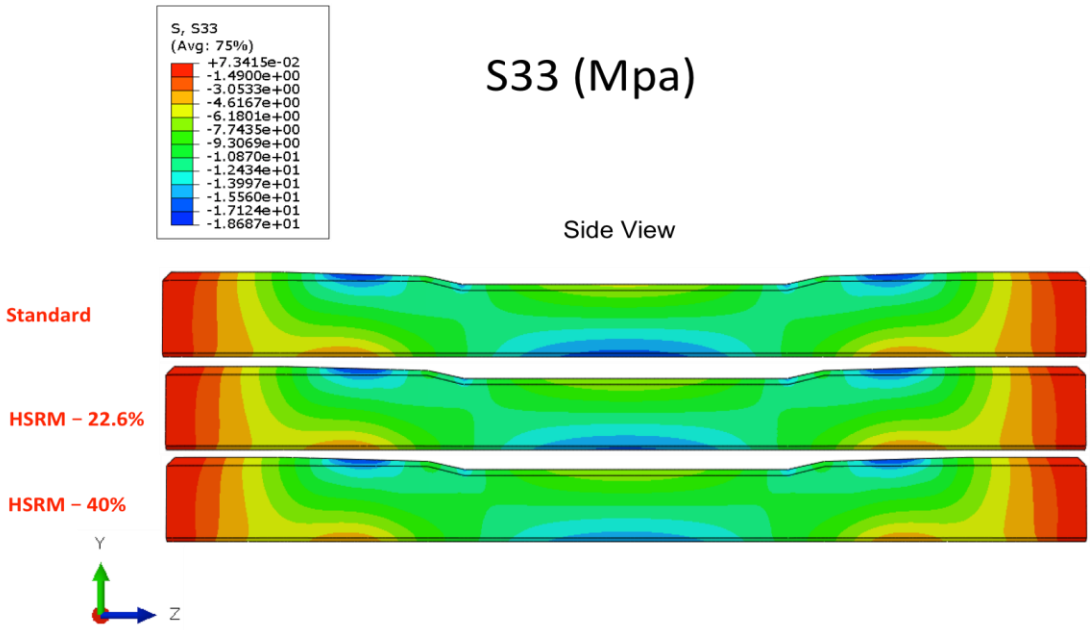

Figure 6.11: Longitudinal stress map with a side view for each concrete tie. Support type: Continuously supported, Load case: L/V = 0

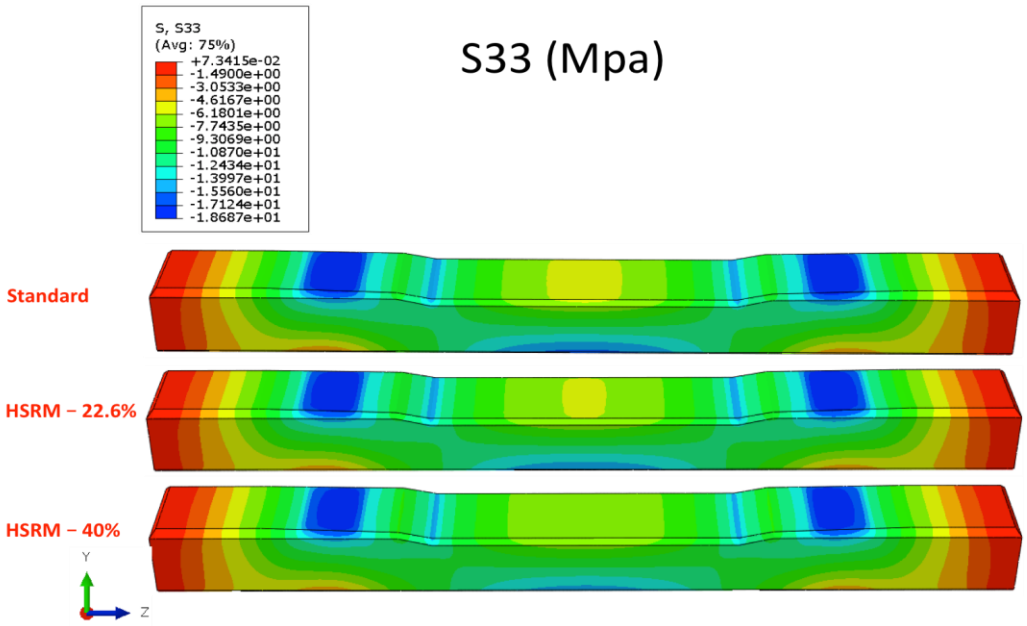

Figure 6.12: Longitudinal stress map with a rotated view for each concrete tie. Support type: Continuously supported, Load case: L/V = 0

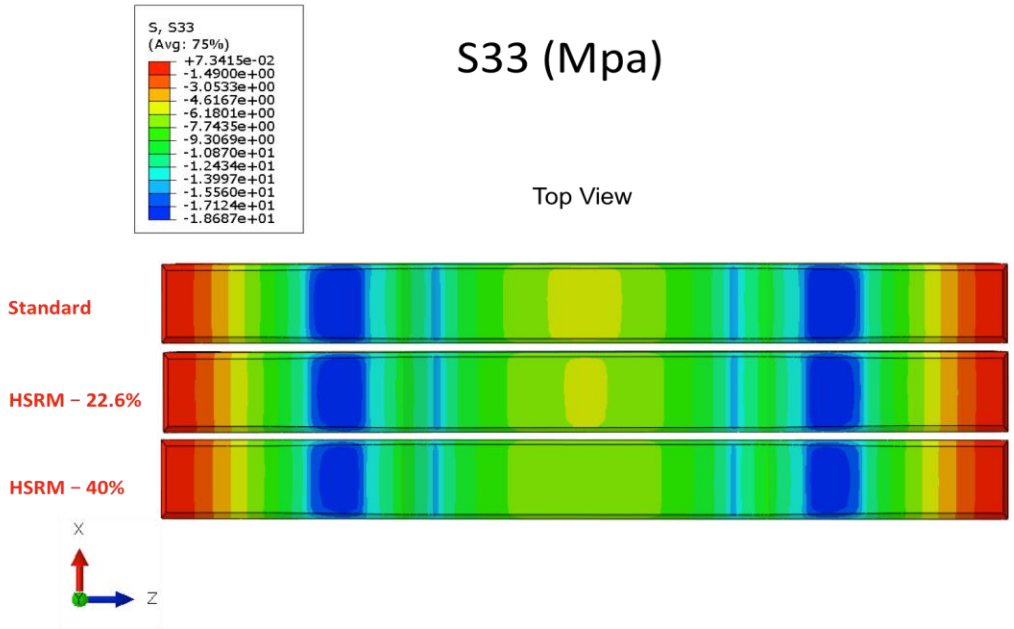

Figure 6.13: Longitudinal stress map with a top view for each concrete tie. Support type: Continuously supported, Load case: L/V = 0

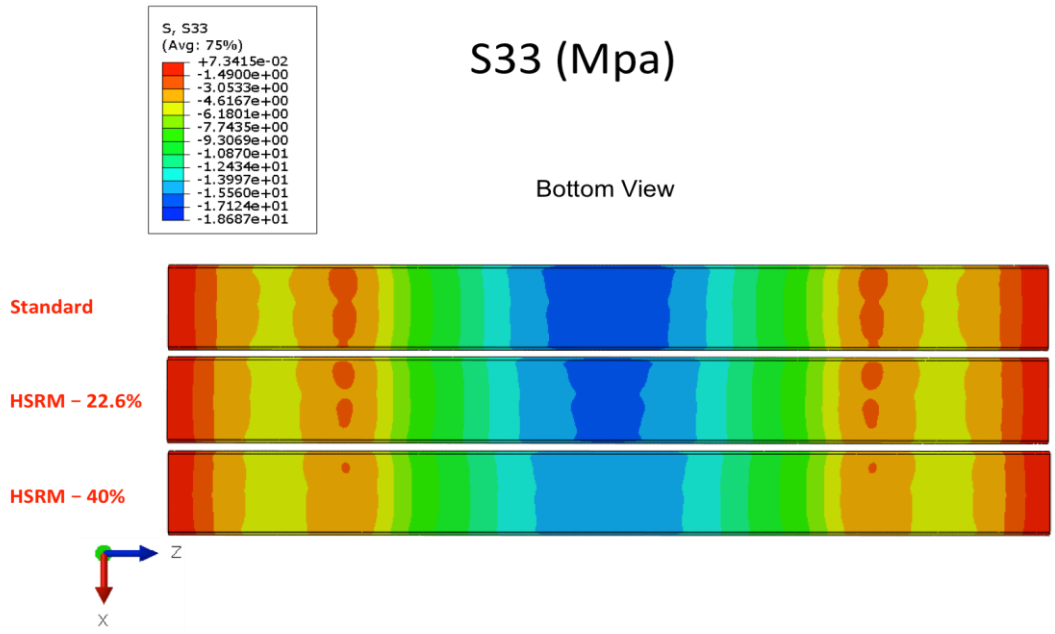

Figure 6.14: Longitudinal stress map with a bottom view for each concrete tie. Support type: Continuously supported, Load case: L/V = 0

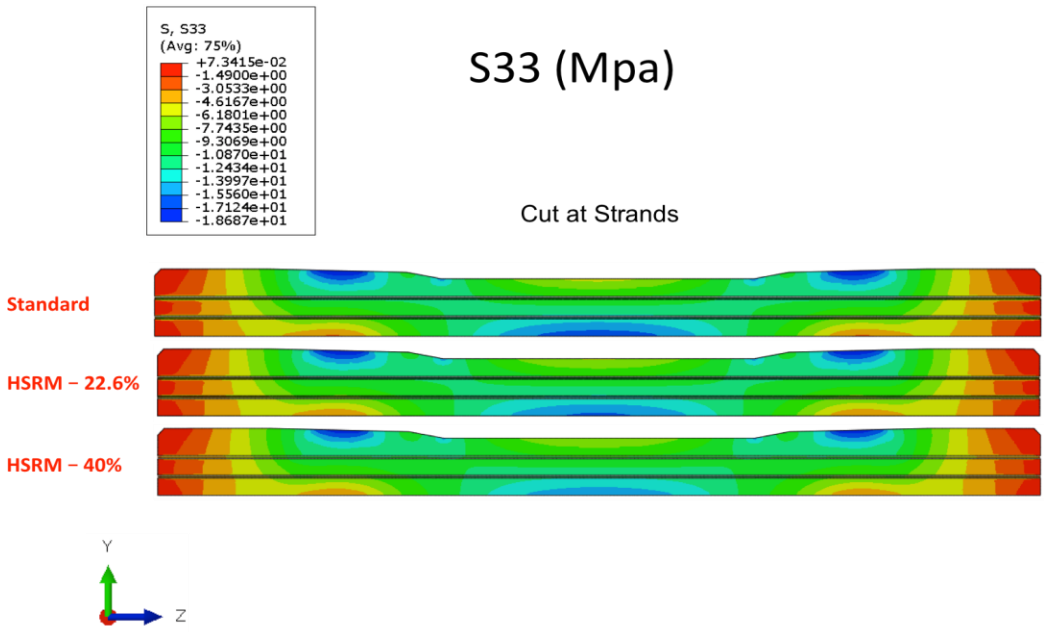

Figure 6.15: Longitudinal stress map inside the tie, at the inside strand, for each concrete tie. Support type: Continuously supported, Load case: L/V = 0

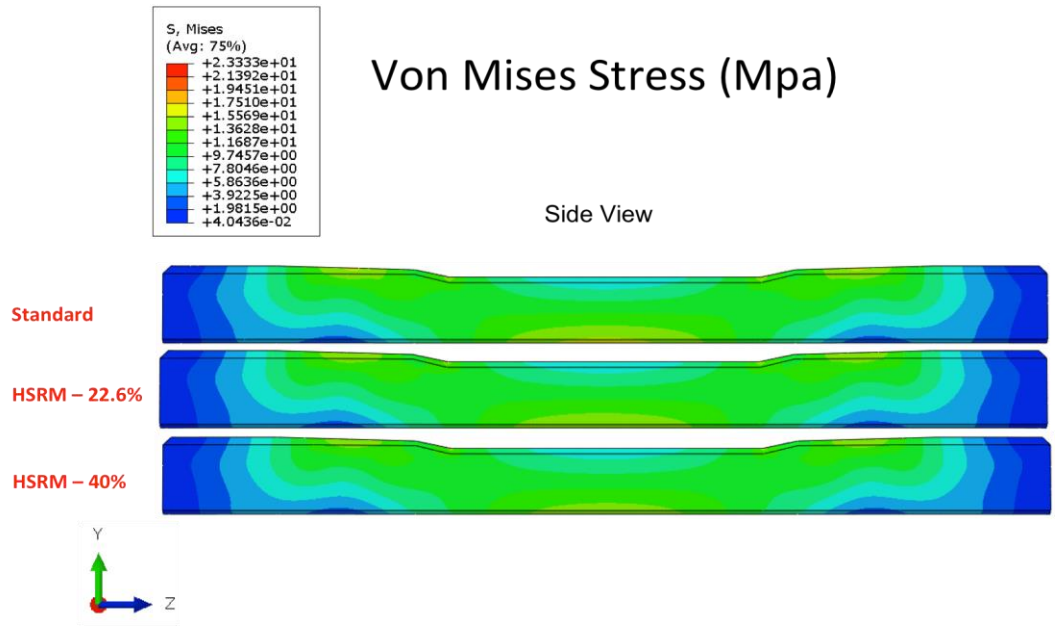

Figure 6.16: Von Mises stress map with a side view for each concrete tie. Support type: Continuously supported, Load case: L/V = 0

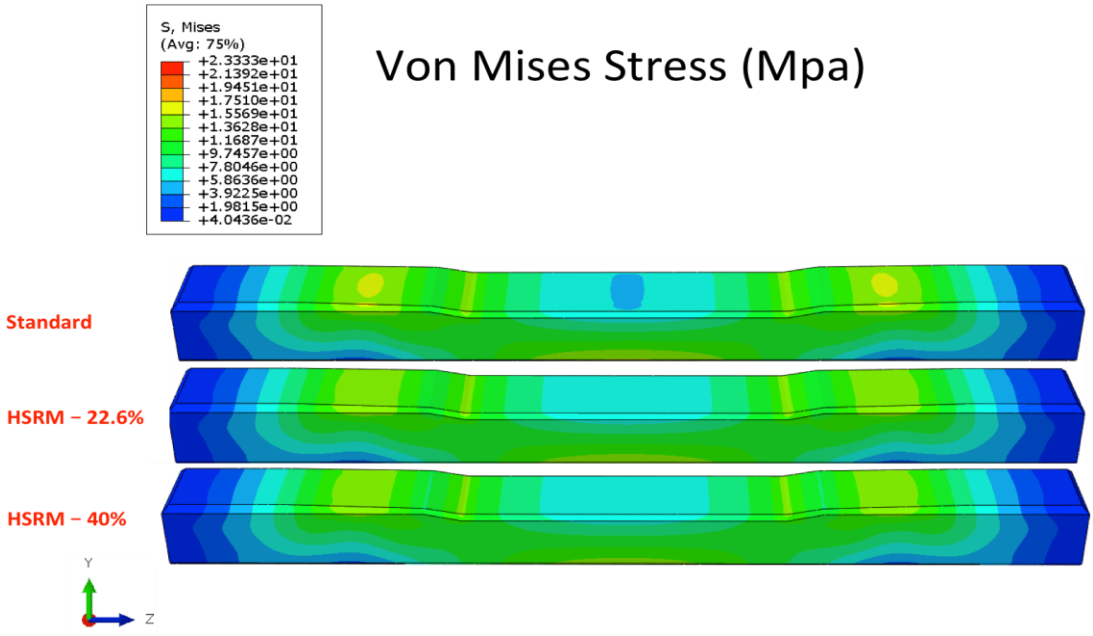

Figure 6.17: Von Mises stress map with a rotated view for each concrete tie. Support type: Continuously supported, Load case: L/V = 0

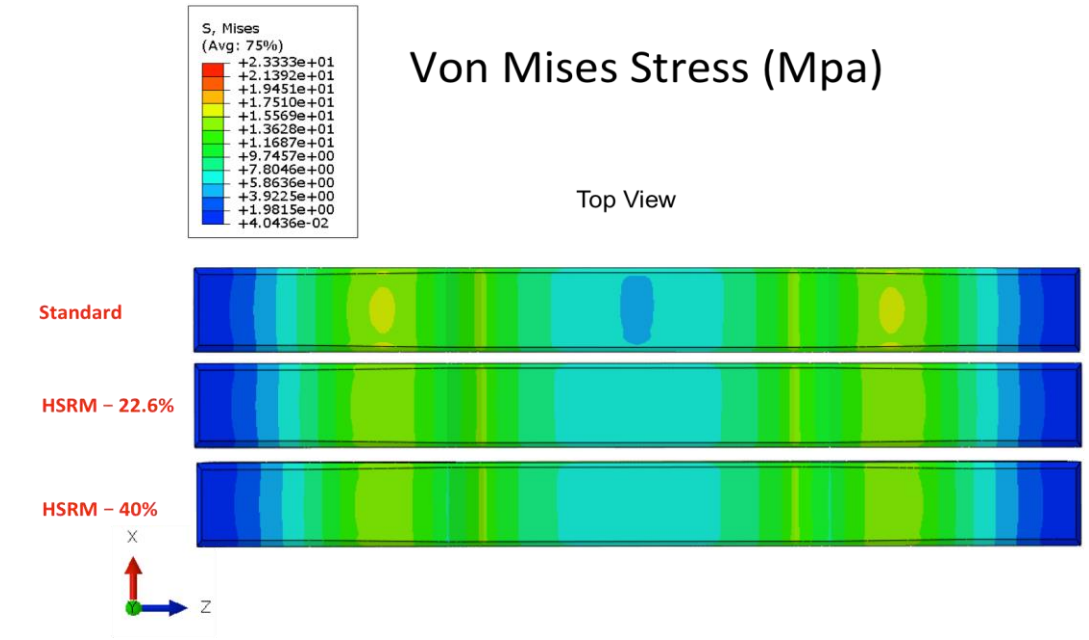

Figure 6.18: Von Mises stress map with a top view for each concrete tie. Support type: Continuously supported, Load case: L/V = 0

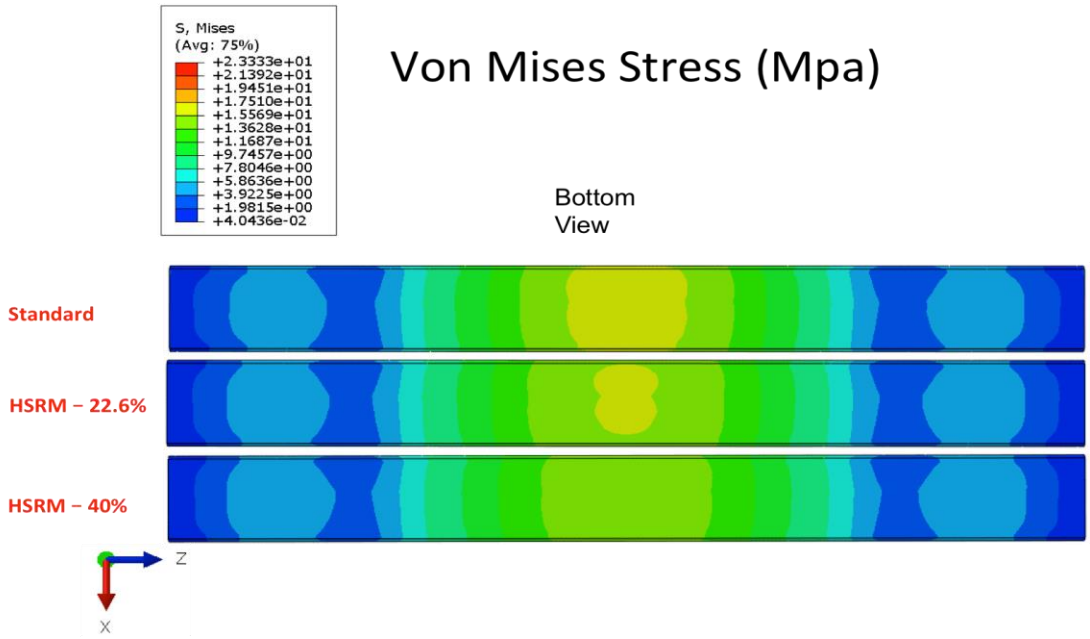

Figure 6.19: Von Mises stress map with a bottom view for each concrete tie. Support type: Continuously supported, Load case: L/V = 0

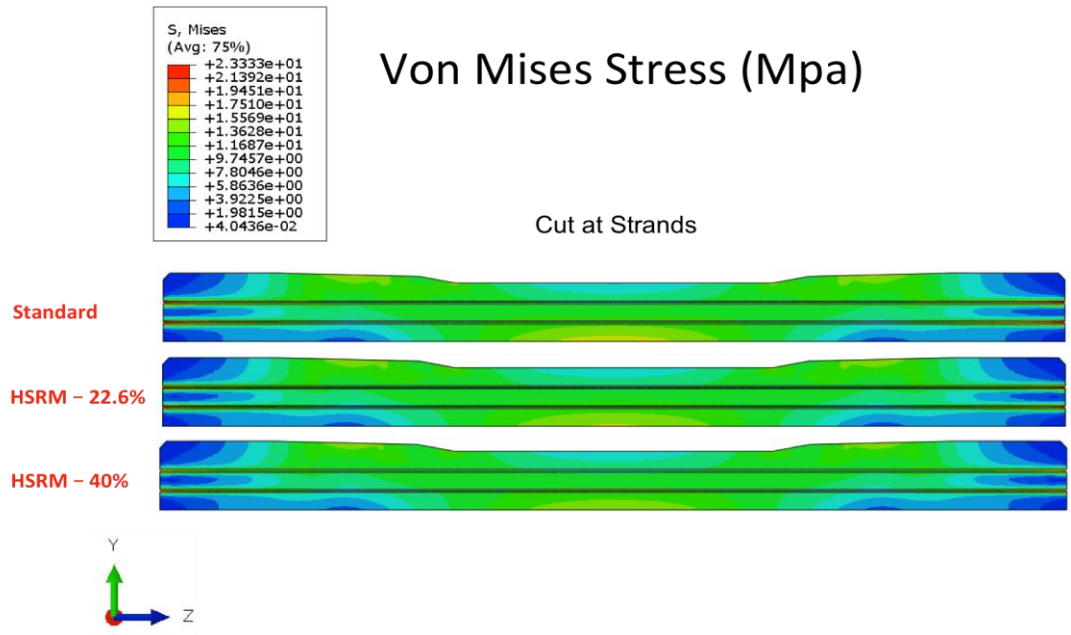

Figure 6.20: Von Mises stress map inside the tie, at the inside strand, for each concrete tie. Support type: Continuously supported, Load case: L/V = 0

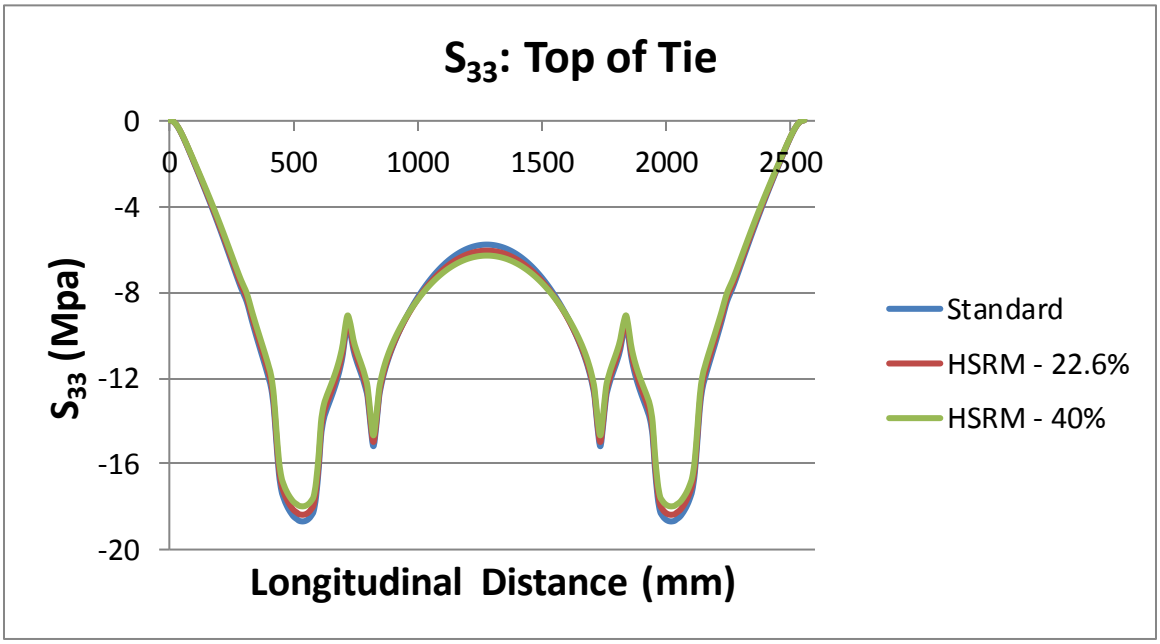

Figure 6.21: Plot of the longitudinal stress along the top fibers of each concrete tie. Support type: Continuously supported, Load case: L/V = 0

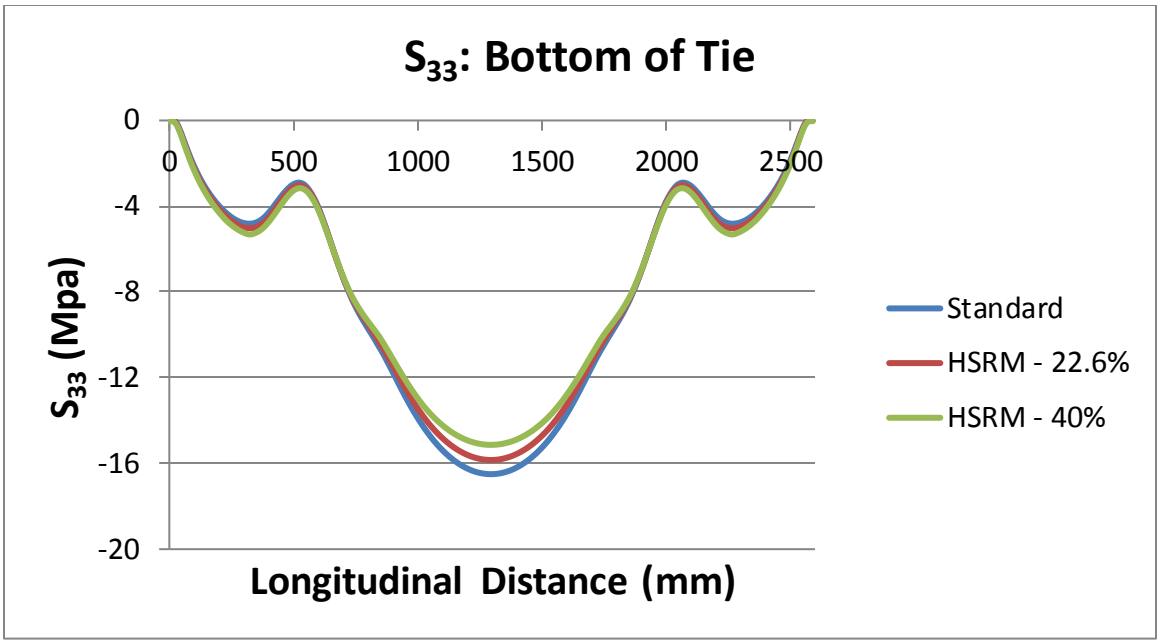

Figure 6.22: Plot of the longitudinal stress along the bottom fibers of each concrete tie. Support type: Continuously supported, Load case: L/V = 0

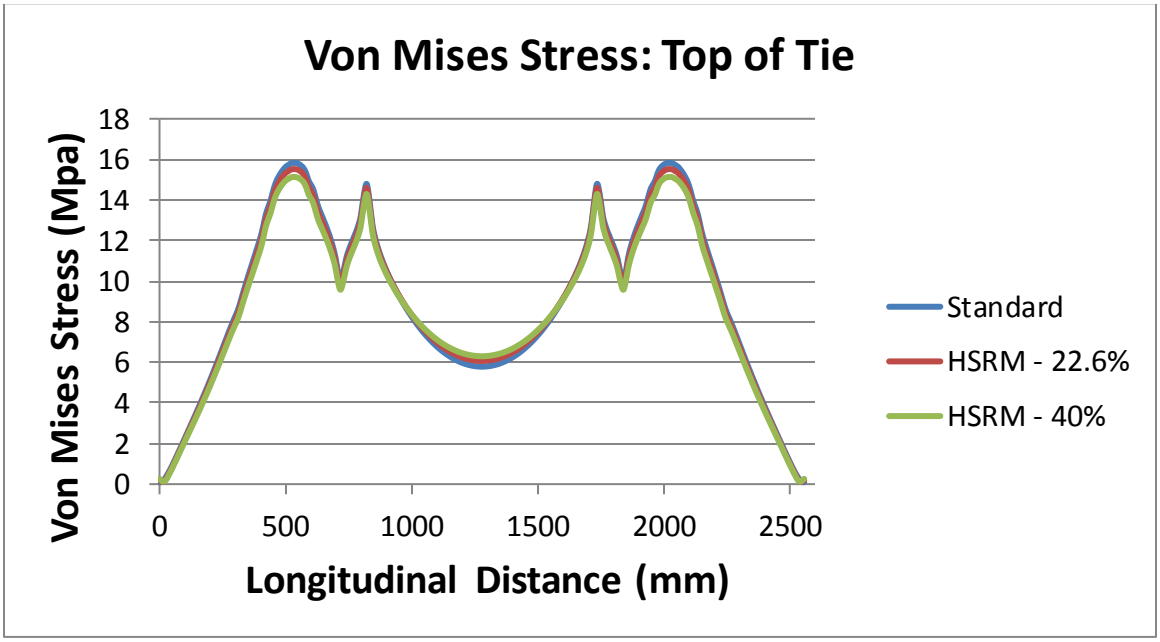

Figure 6.23: Plot of von Mises stress along the top fibers of each concrete tie. Support type: Continuously supported, Load case: L/V = 0

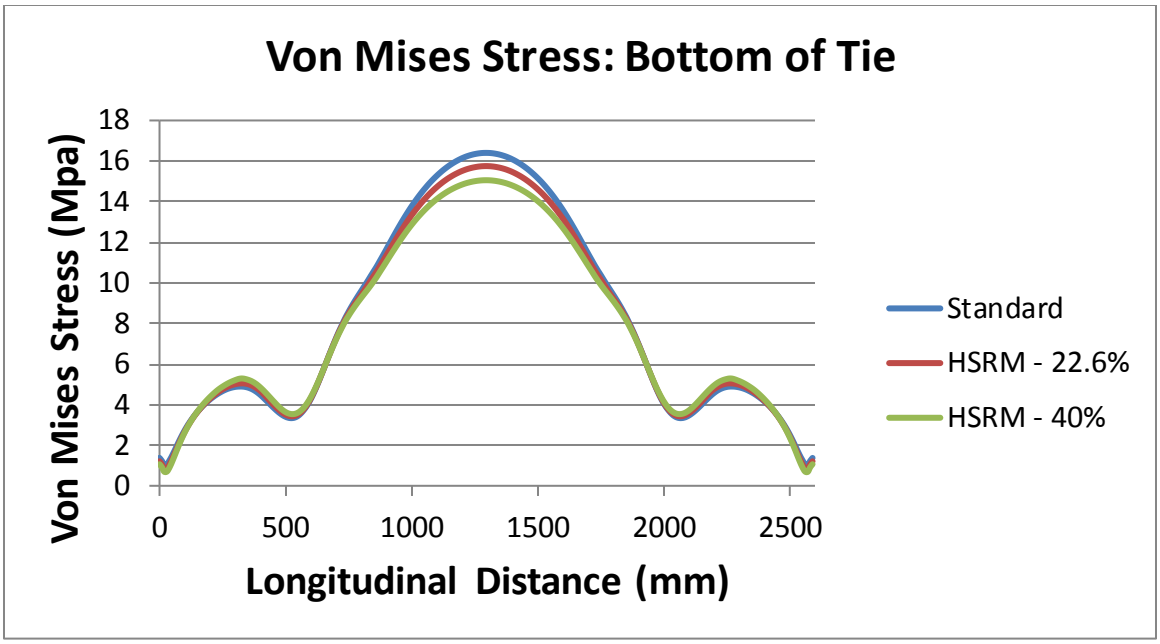

Figure 6.24: Plot of von Mises stress along the bottom fibers of each concrete tie. Support type: Continuously supported, Load case: L/V = 0

Load Case: L/V = .6

A 40 kip vertically applied load is distributed over each rail seat area and one 24 Kip laterally applied load is distributed over one of the rail seat areas for the L/V = .6 load case, as discussed in the "Loads and Boundary Conditions" section of Chapter 5 (Figure 6.25). The deformed shape, longitudinal stresses (S_{33}), and von Mises Stresses throughout the tie are recorded and presented in Figures (6.26-6.36). Stress maps are superimposed onto the tie for visualization. Additionally, stresses along the top and bottom fibers of the concrete tie are measured along its length and are presented in Figures (6.37-6.40). Figures (6.27-6.36) are adjusted to the same scale for comparison.

No tensile damage is observed in the tie during the loading procedure. The standard, HSRM-22.6% and HSRM-40% concrete ties appear to remain in a compressive state after the analysis step has concluded. The deformed shape of the tie illustrates a negative bending moment with a flexural stress distribution comparable to that shown in Figure (6.10a). The deformed shape illustrates that the stresses in the tie are no longer symmetric on either side due to the longitudinal force applied at one of the rail seats. It is intuitively obvious that an increase in the magnitude of the vertical loads applied at each rail seat will results in top fibers of the concrete shifting towards a tensile state and an increase in the magnitude of compressive stresses at the bottom fibers as shown in Figure (6.10b). Based on this behavior, it is clear that of the three concrete models, the tie that exhibits greater compressive stresses in its top fibers and lower compressive stresses in its bottom fibers is more preferred than its counterparts.

The maximum longitudinal stress (S_{33}) measured at the middle top fibers of the standard, HSRM-22.6%, and HSRM-40% concrete tie is -594.9 psi (-4.10 Mpa), -660.4 psi (-4.55 Mpa), and -716.8 psi (-4.94 Mpa). The maximum longitudinal stress (S_{33}) measured at the middle bottom fibers of the standard, HSRM-22.6%, and HSRM-40% concrete tie is -2,307.6 psi (-15.91 Mpa), -2,200.1 psi (-15.17 Mpa), and -2,088.7 psi (-14.40 Mpa). The maximum von Mises Stress measured at the middle top fibers of the standard, HSRM-22.6%, and HSRM-40% is 596.3 psi (4.11 Mpa), 660.8 psi (4.56 Mpa), and 718.5 psi (4.95 Mpa). The maximum von Mises Stress measured at the middle bottom fibers of the standard, HSRM-22.6%, and HSRM-40% is 2,295.2 psi (15.83 Mpa), 2,189.3 psi (15.10 Mpa), and 2,079.4 psi (14.34 Mpa). Both the HSRM-22.6% and HSRM-

40% concrete tie appear to outperform the standard tie, with the HSRM-40% showing the most desirable response of better distributing the stresses throughout the tie. For the HSRM-22.6% concrete tie, an 11% increase and a 4.66% decrease in the compressive stresses were observed at the center top and bottom fibers of the concrete tie, when compared to the standard tie. For the HSRM-40% concrete tie, a 20.37% increase and an 9.48% decrease in the compressive stresses seen at the center top and bottom fibers of the concrete tie were observed, when compared to the standard tie.

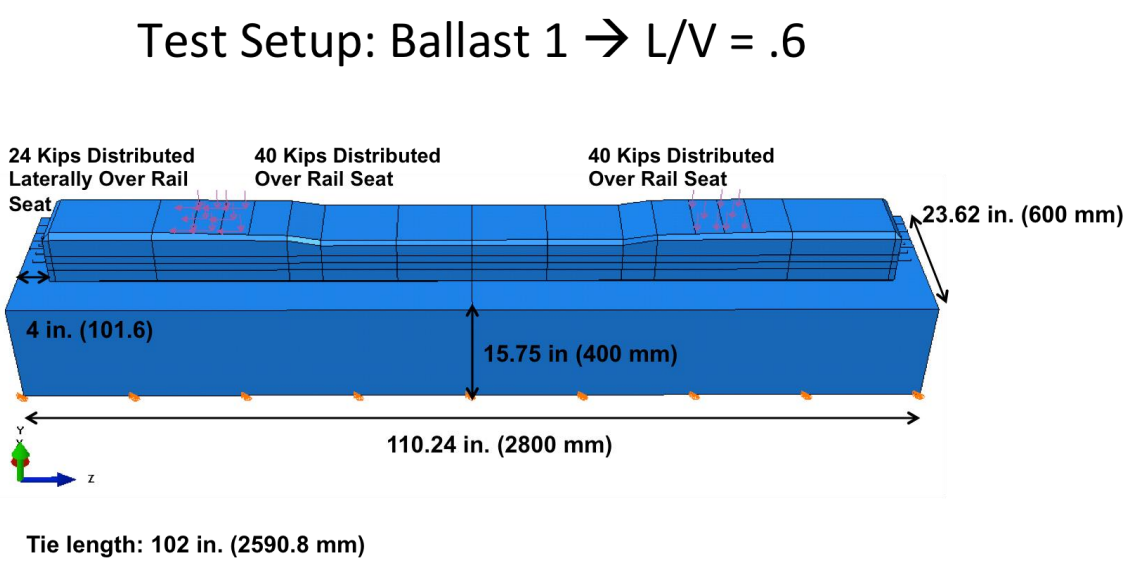

Figure 6.25: Test setup for the continuously supported tie with the load case of L/V = .6

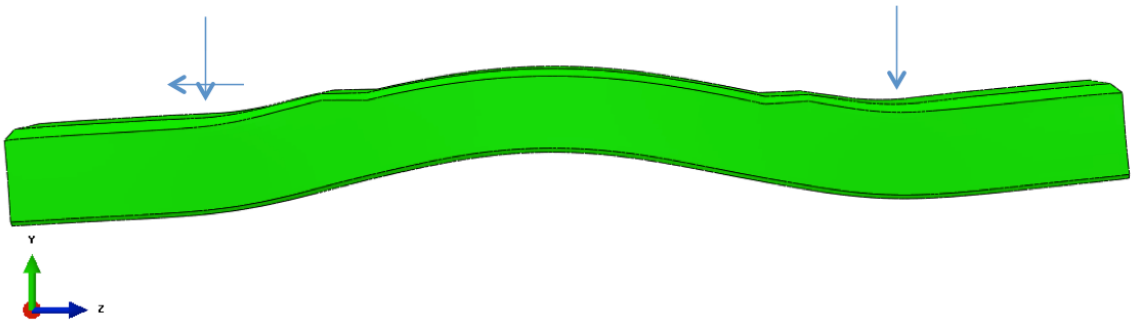

Figure 6.26: Deformed shape of the concrete tie for the continuously supported tie with the L/V = .6 load case

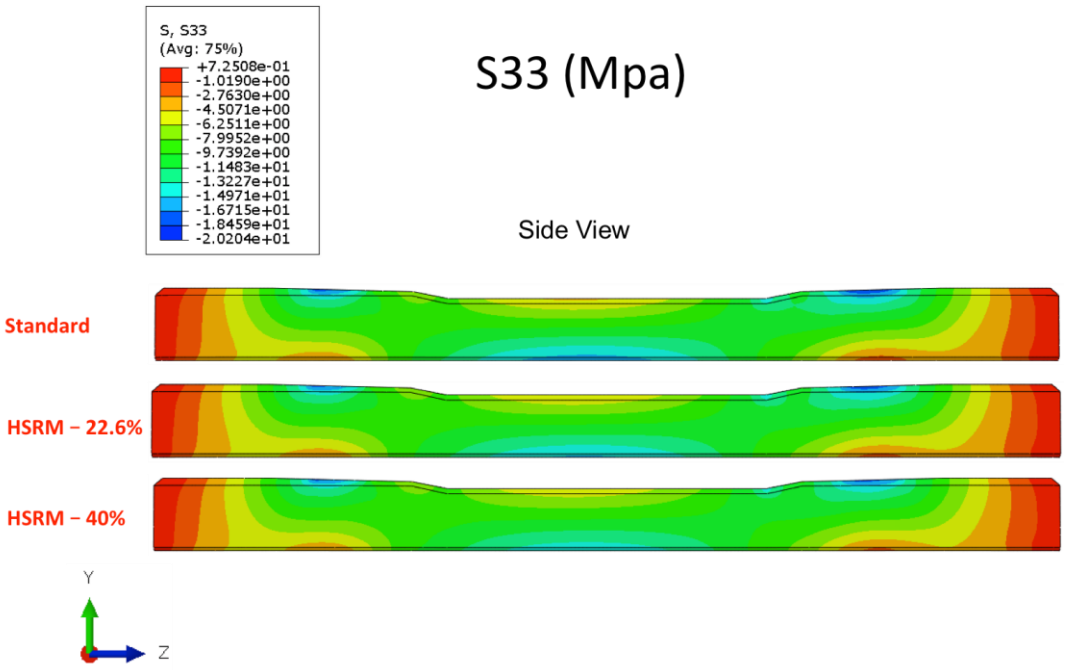

Figure 6.27: Longitudinal stress map with a side view for each concrete tie. Support type: Continuously supported, Load case: L/V = .6

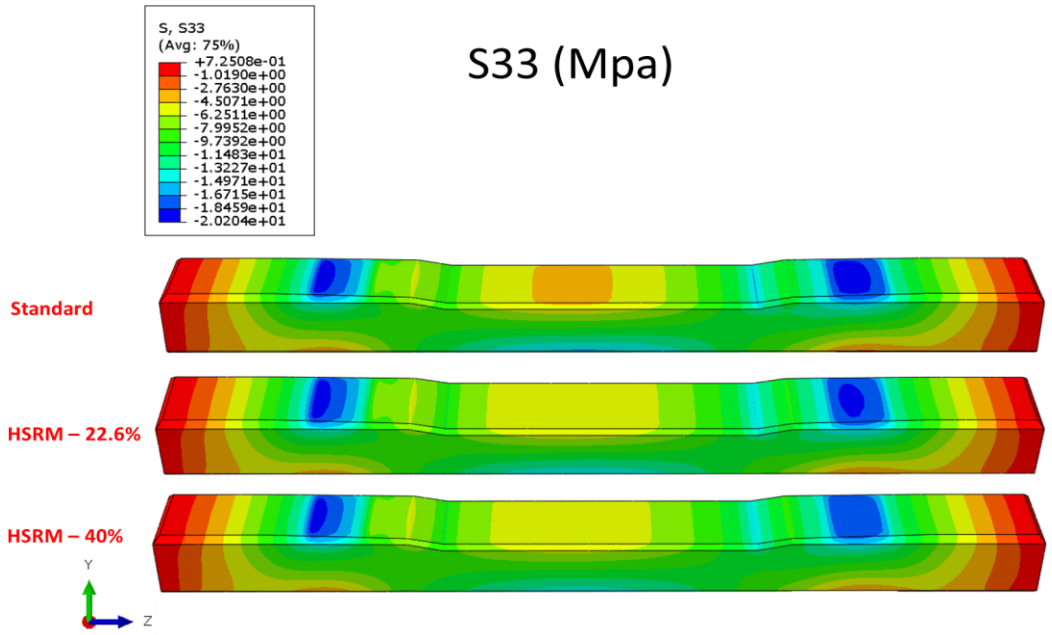

Figure 6.28: Longitudinal stress map with a rotated view for each concrete tie. Support type: Continuously supported, Load case: L/V = .6

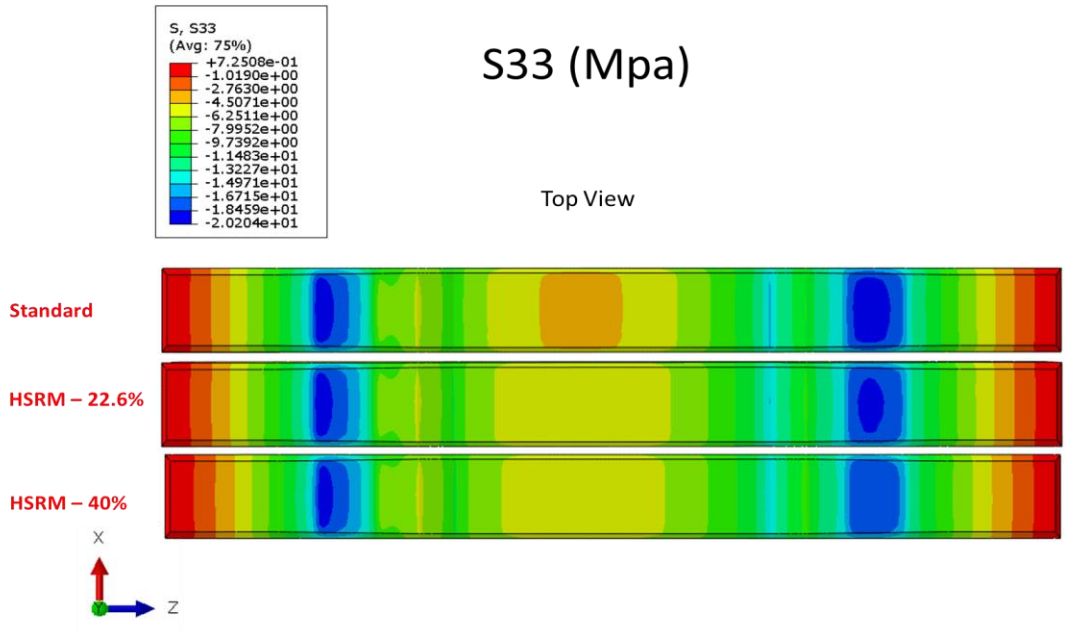

Figure 6.29: Longitudinal stress map with a top view for each concrete tie. Support type: Continuously supported, Load case: L/V = .6

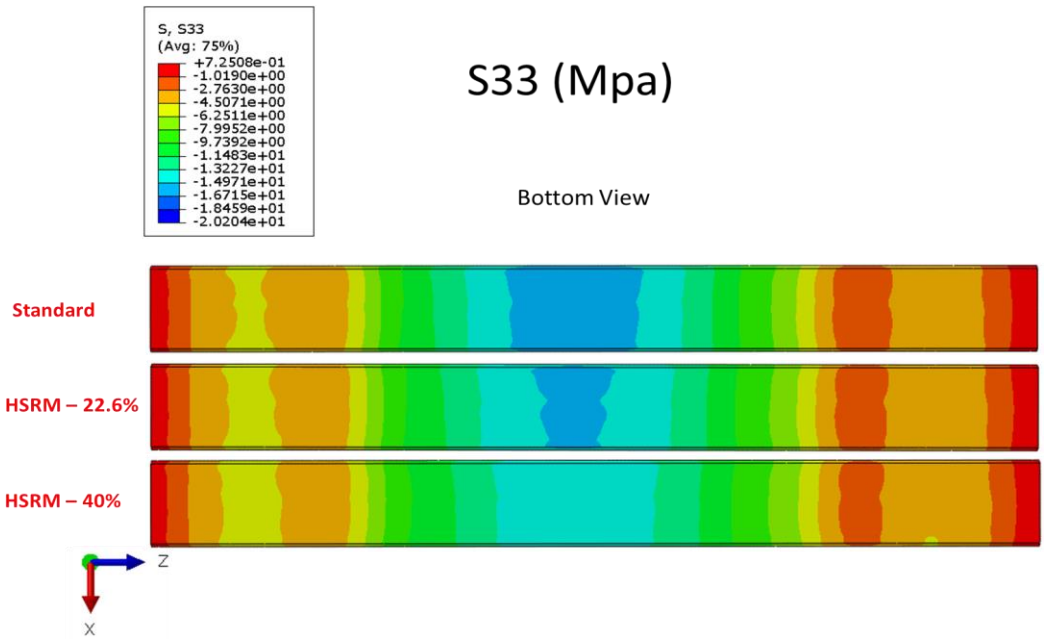

Figure 6.30: Longitudinal stress map with a bottom view for each concrete tie. Support type: Continuously supported, Load case: L/V = .6

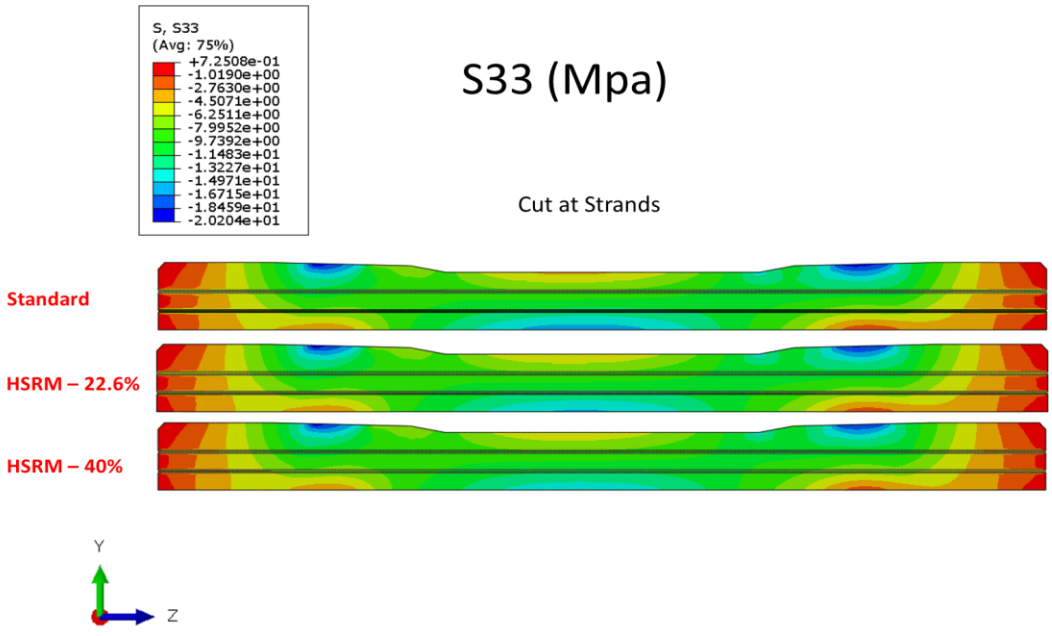

Figure 6.31: Longitudinal stress map inside the tie, at the inside strand, for each concrete tie. Support type: Continuously supported, Load case: L/V = .6

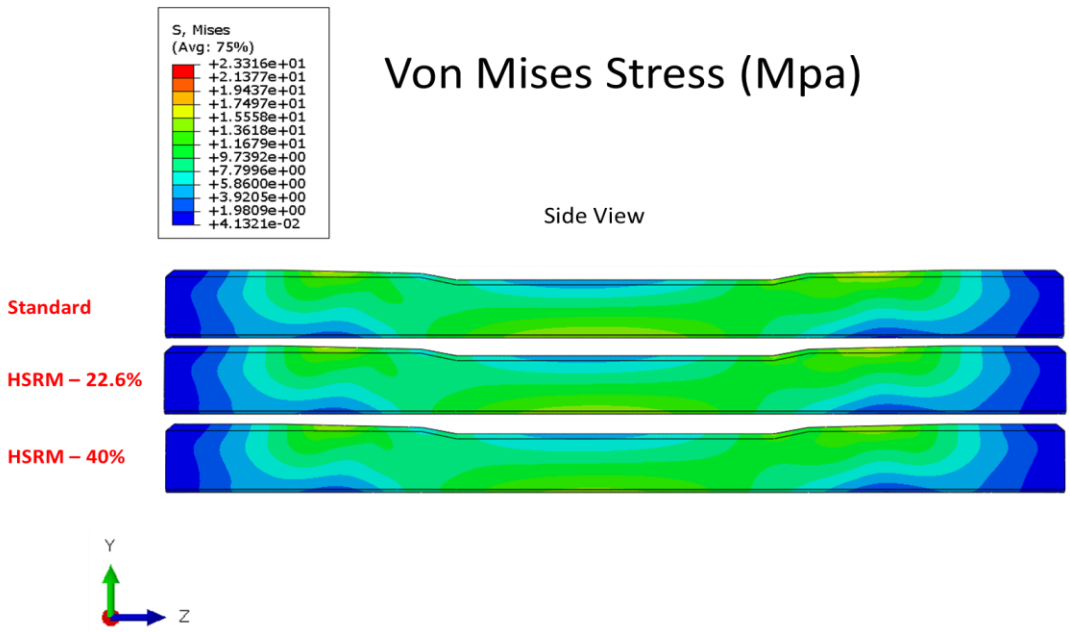

Figure 6.32: Von Mises stress map with a side view for each concrete tie. Support type: Continuously supported, Load case: L/V = .6

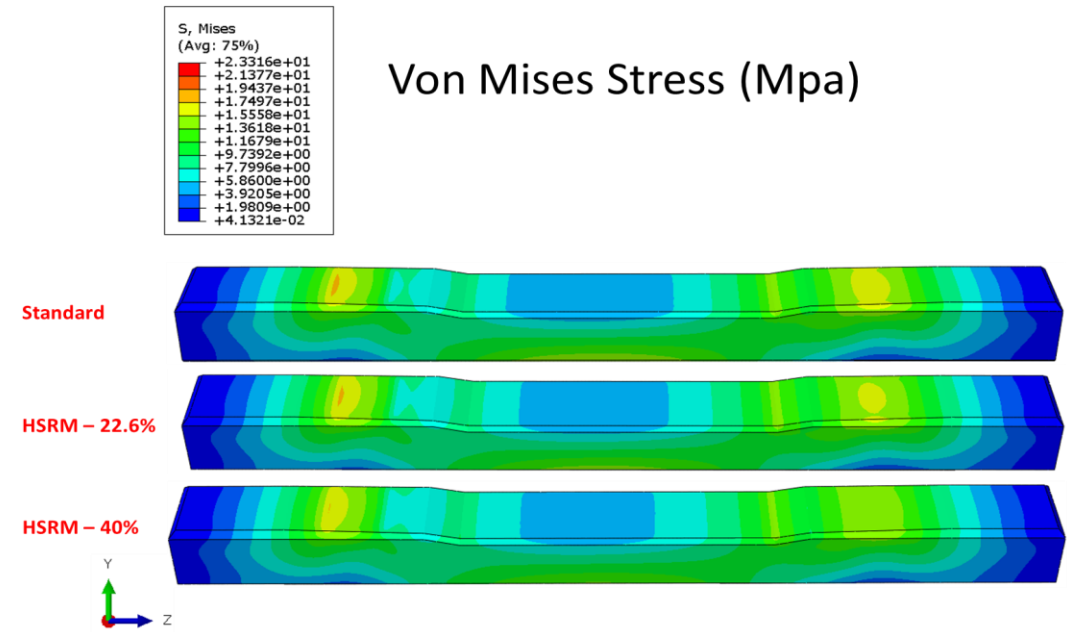

Figure 6.33: Von Mises stress map with a rotated view for each concrete tie. Support type: Continuously supported, Load case: L/V = .6

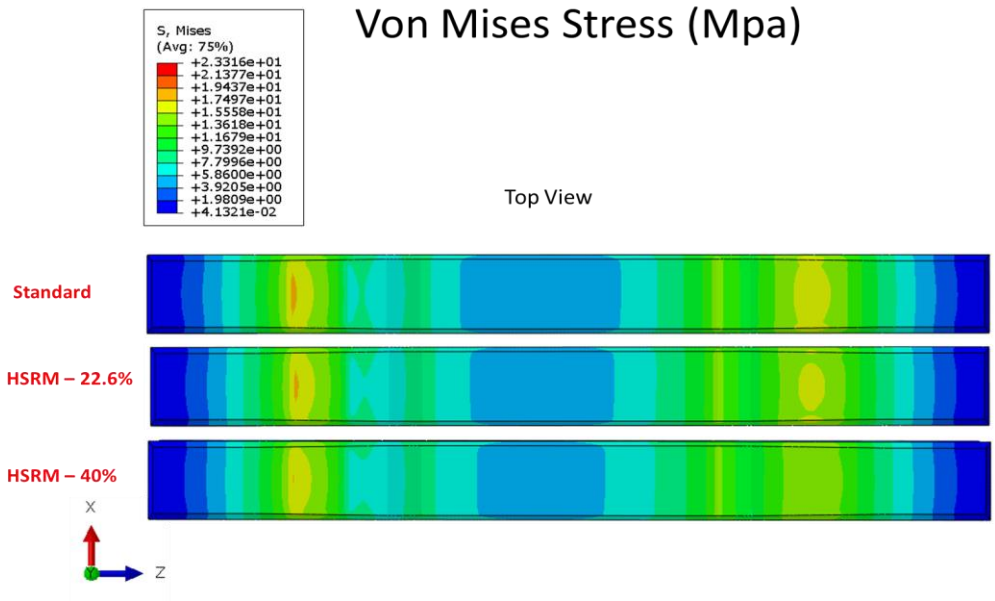

Figure 6.34: Von Mises stress map with a top view for each concrete tie. Support type: Continuously supported, Load case: L/V = .6

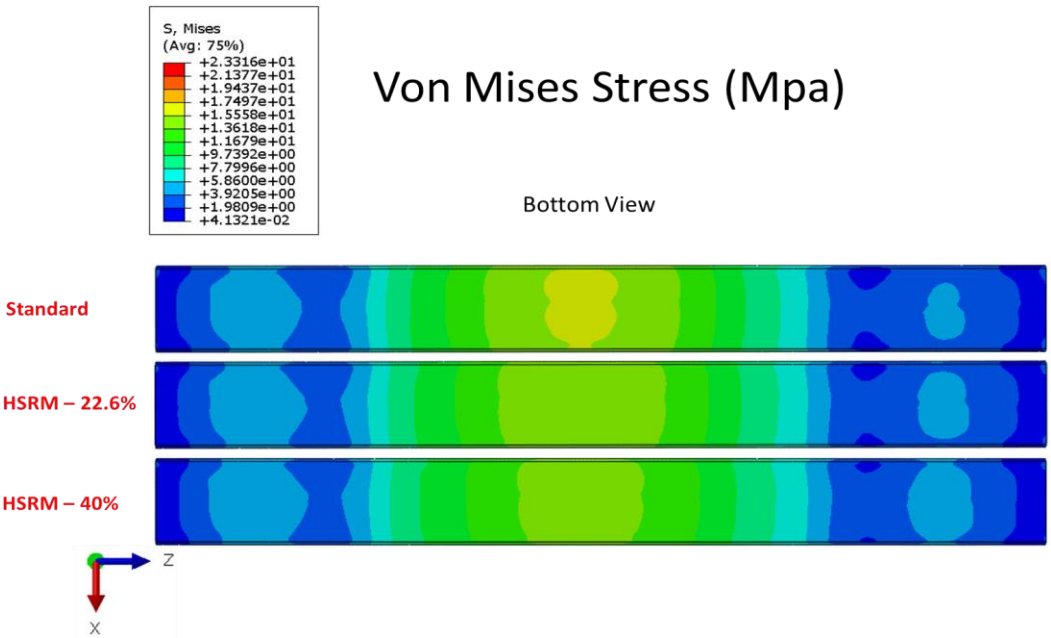

Figure 6.35: Von Mises stress map with a bottom view for each concrete tie. Support type: Continuously supported, Load case: L/V = .6

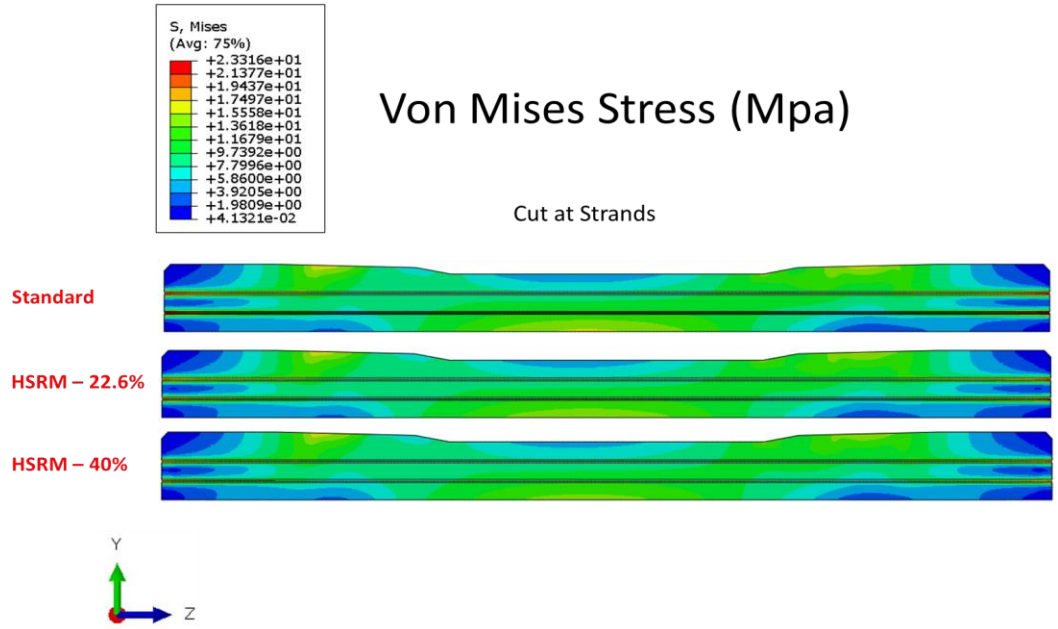

Figure 6.36: Von Mises stress map inside the tie, at the inside strand, for each concrete tie. Support type: Continuously supported, Load case: L/V = .6

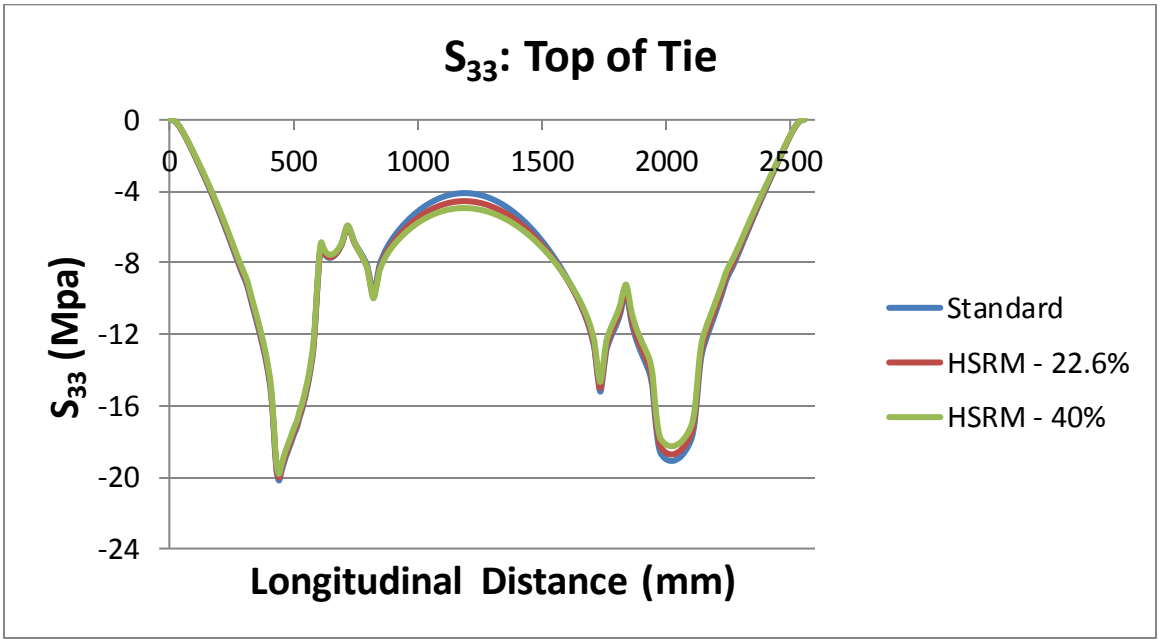

Figure 6.37: Plot of the longitudinal stress along the top fibers of each concrete tie. Support type: Continuously supported, Load case: L/V = .6

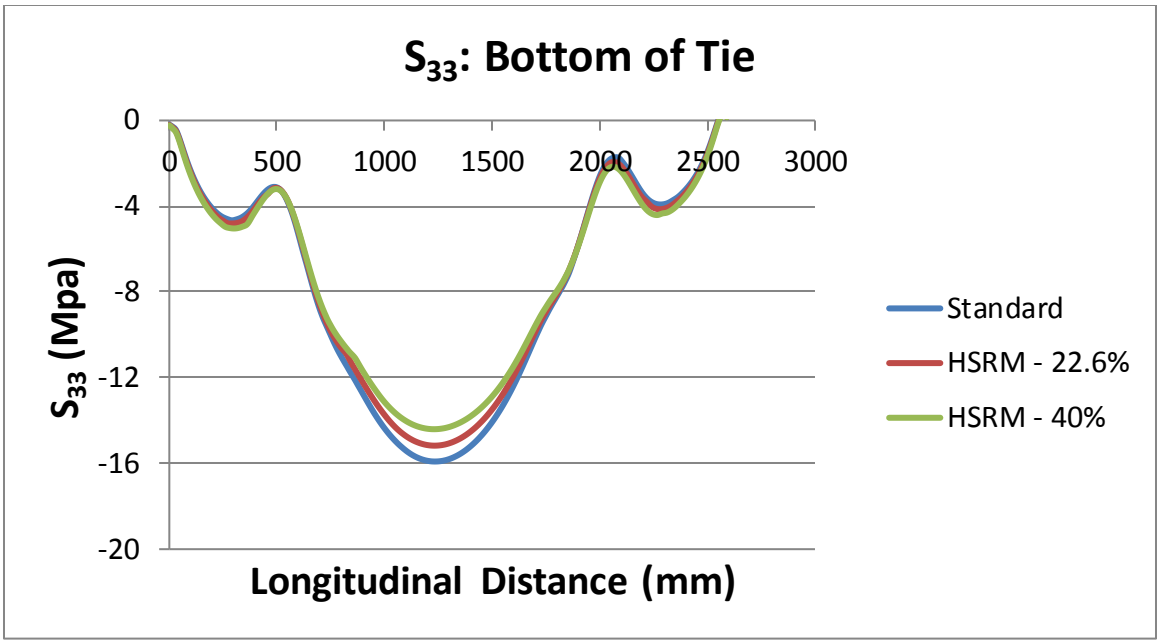

Figure 6.38: Plot of the longitudinal stress along the bottom fibers of each concrete tie. Support type: Continuously supported, Load case: L/V = .6

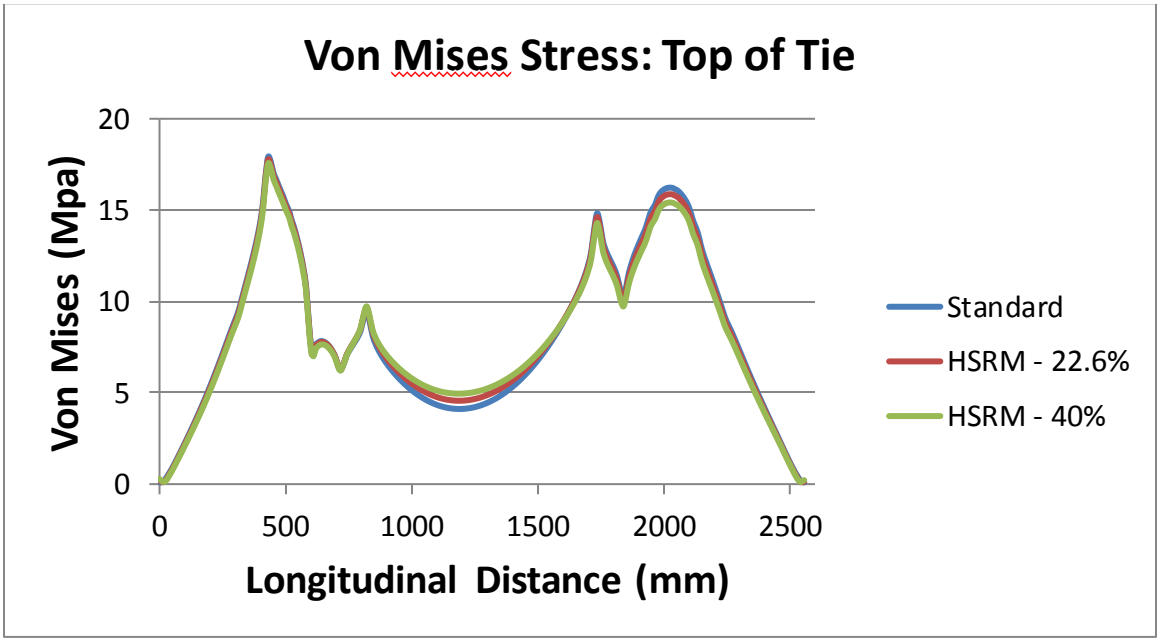

Figure 6.39: Plot of von Mises stress along the top fibers of each concrete tie. Support type: Continuously supported, Load case: L/V = .6

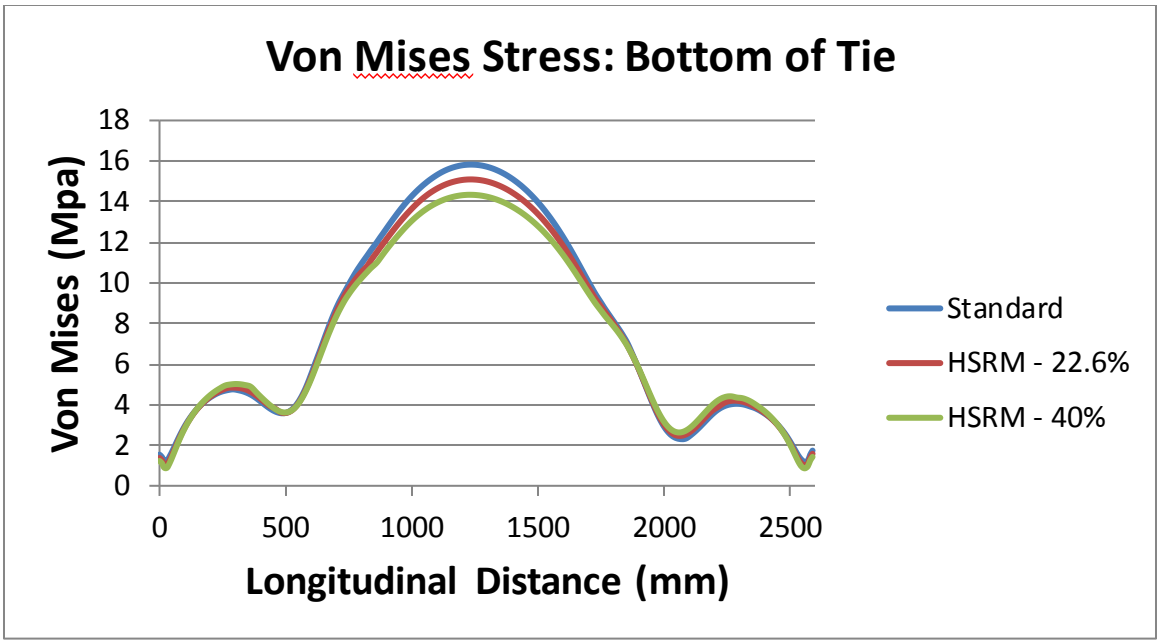

Figure 6.40: Plot of von Mises stress along the bottom fibers of each concrete tie. Support type: Continuously supported, Load case: L/V = .6

End Supported

Load Case: L/V = 0

A 40 kip vertically applied load is distributed over each rail seat area for the L/V = 0 load case, as discussed in the "Loads and Boundary Conditions" section of Chapter 5 (Figure 6.41). The deformed shape, longitudinal stresses (S_{33}), and von Mises Stresses throughout the tie are recorded and presented in Figures (6.42, 6.44-6.53). Stress maps are superimposed onto the tie for visualization. Additionally, stresses along the top and bottom fibers of the concrete tie are measured along its length and are presented in Figures (6.54-6.57). Figures (6.44-6.53) presented below are adjusted to the same scale for comparison.

No damage is observed in the tie during the loading procedure. The standard, HSRM-22.6% and HSRM-40% concrete ties appear to remain in a compressive state after the analysis step has concluded. The deformed shape of the tie illustrates a positive bending moment with a flexural stress distribution similar to that shown in Figure (6.43a). It is intuitively obvious that an increase in the magnitude of the vertical loads applied at each rail seat will results in an increase in the magnitude of the compressive stress seen at the top fibers of the concrete, while the stresses in the bottom fibers will tend to shift towards a tensile state as shown in Figure (6.43b). It is now clear that of the three concrete models, the tie that exhibits lower compressive stresses in its top fibers and higher compressive stresses in its bottom fibers is more preferred than its counterparts.

The longitudinal stress (S_{33}) measured at the middle top fibers of the standard, HSRM-22.6%, and HSRM-40% concrete tie is -2,483.3 psi (-17.12 Mpa), -2,317.8 psi (-15.98 Mpa), and -2,161.8 psi (-14.91 Mpa). The longitudinal stress (S_{33}) measured at the middle bottom fibers of the standard, HSRM-22.6%, and HSRM-40% concrete tie is -1,017.9 psi (-7.02 Mpa), -1,121.4 psi (-7.73 Mpa), and -1,200.2 psi (-8.28 Mpa). The von Mises Stress measured at the middle top fibers of the standard, HSRM-22.6%, and HSRM-40% is 2,485.1 psi (17.13 Mpa), 2,319.4 psi (16.0 Mpa), and 2,163.5 psi (14.92 Mpa). The von Mises Stress measured at the middle bottom fibers of the standard, HSRM-22.6%, and HSRM-40% is 1,019.3 psi (7.03 Mpa), 1,123.0 psi (7.74 Mpa), and 1,201.8 psi (8.29 Mpa). Both the HSRM-22.6% and HSRM-40% concrete tie appear to outperform the standard tie, with the HSRM-40% showing the most desirable response

of better distributing the stresses throughout the tie. For the HSRM-22.6% concrete tie, a 6.67% decrease and a 10.18% increase in the compressive stresses were observed at the center top and bottom fibers of the concrete tie, when compared to the standard tie. For the HSRM-40% concrete tie, a 12.95% decrease and a 17.91% increase in the compressive stresses seen at the center top and bottom fibers of the concrete tie were observed, when compared to the standard tie.

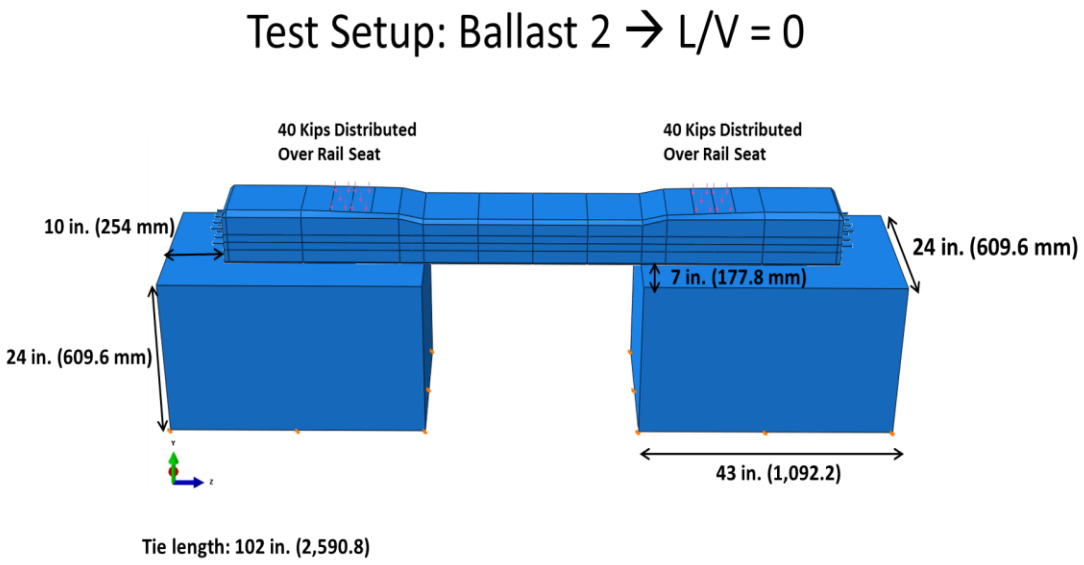

Figure 6.41: Test setup for the end supported tie with the load case of L/V = 0

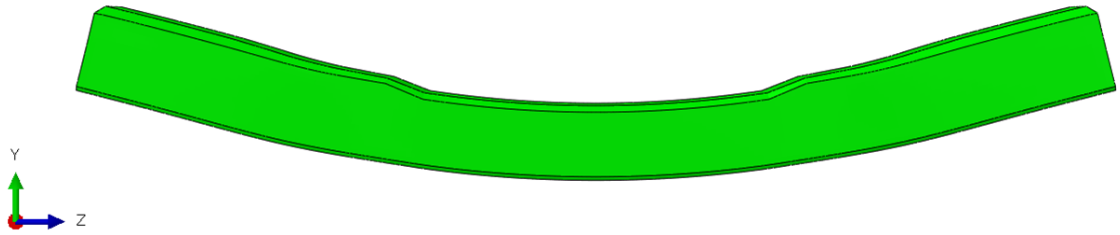

Figure 6.42: Deformed shape of the concrete tie for the end supported tie with the L/V = 0 load case

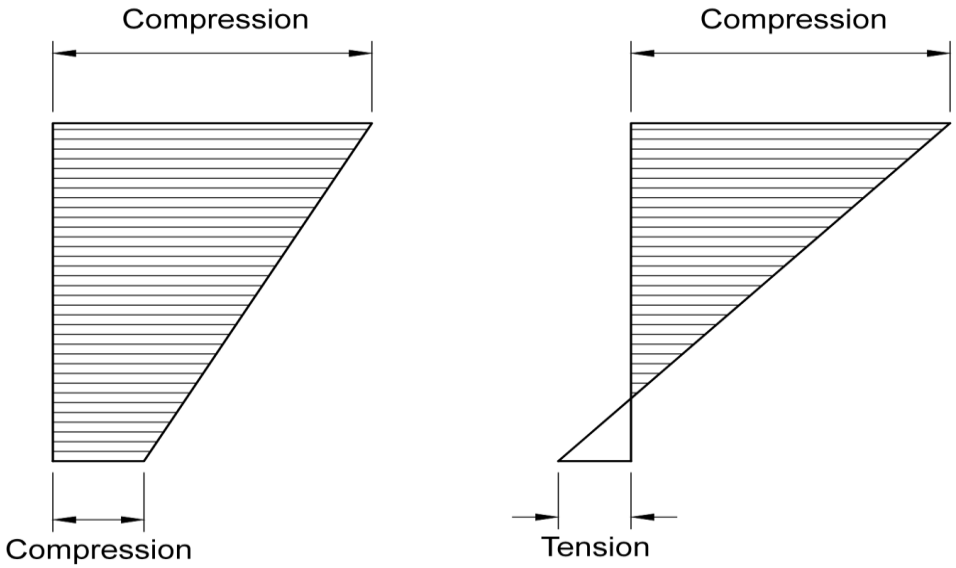

Figure 6.43a & 6.43b: a) Idealized stress distribution for the concrete tie after 80 kips of load has been applied to the rail seat. b) Hypothetical stress distribution if additional load is applied beyond the 80 Kips

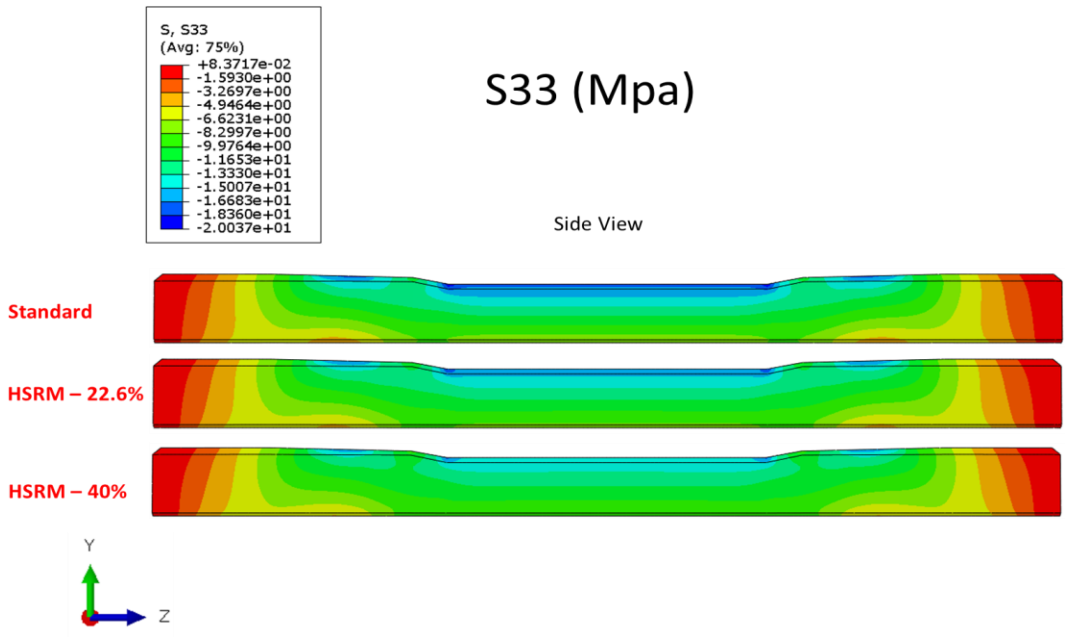

Figure 6.44: Longitudinal stress map with a side view for each concrete tie. Support type: End supported, Load case: L/V = 0

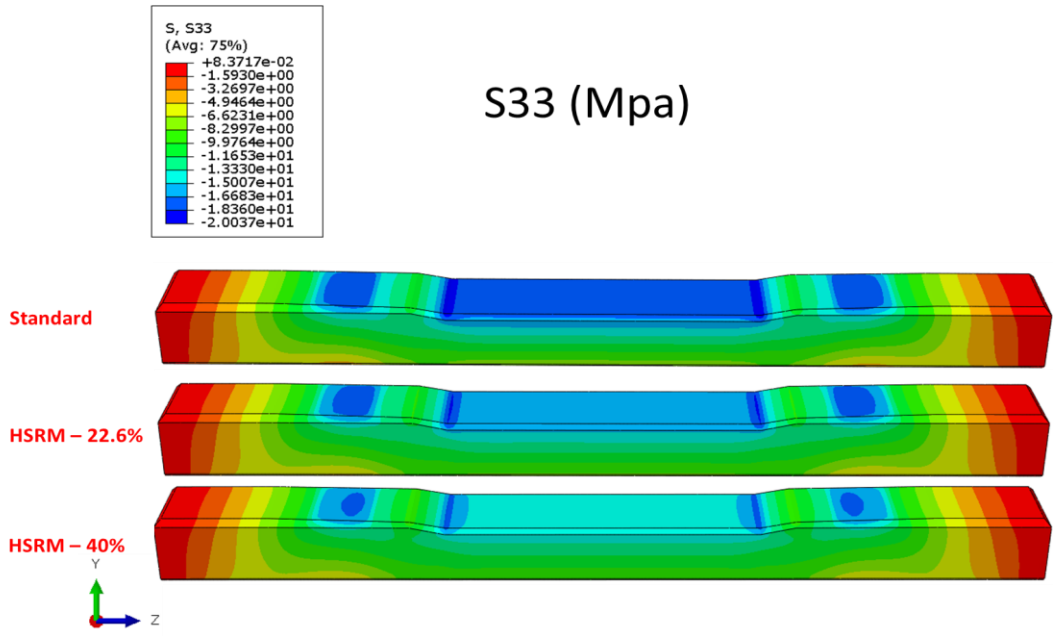

Figure 6.45: Longitudinal stress map with a rotated view for each concrete tie. Support type: End supported, Load case: L/V = 0

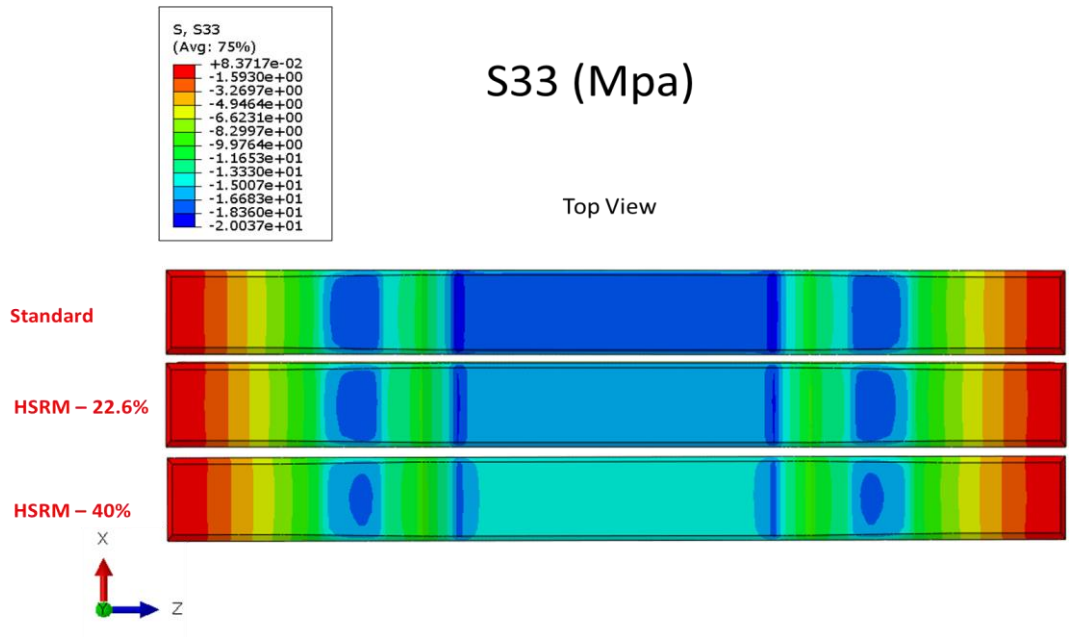

Figure 6.46: Longitudinal stress map with a top view for each concrete tie. Support type: End supported, Load case: L/V = 0

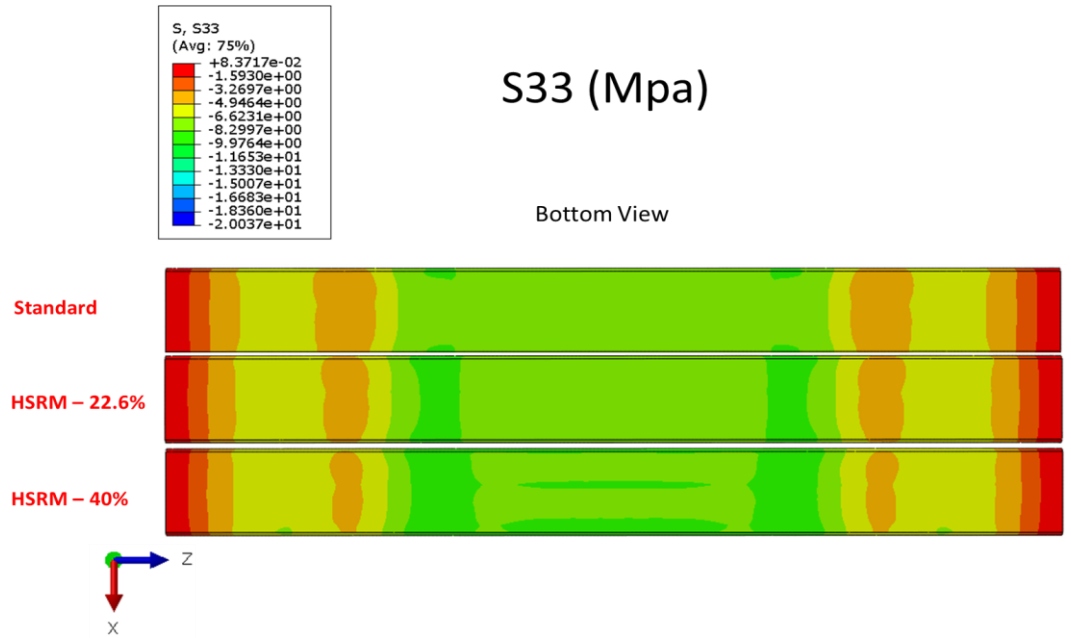

Figure 6.47: Longitudinal stress map with a bottom view for each concrete tie. Support type: End supported, Load case: L/V = 0

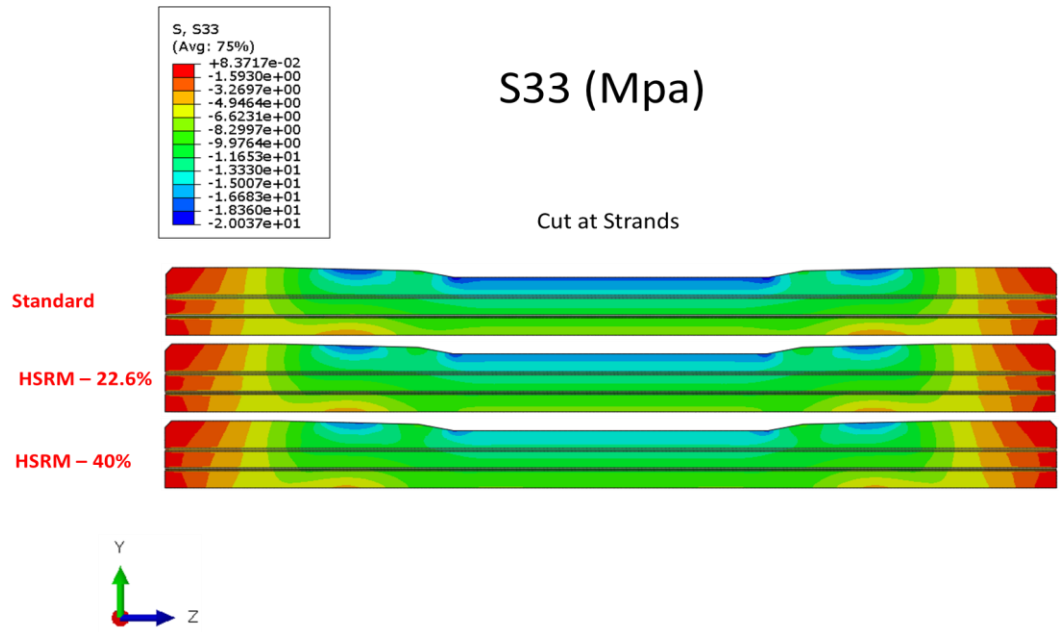

Figure 6.48: Longitudinal stress map inside the tie, at the inside strand, for each concrete tie. Support type: End supported, Load case: L/V = 0

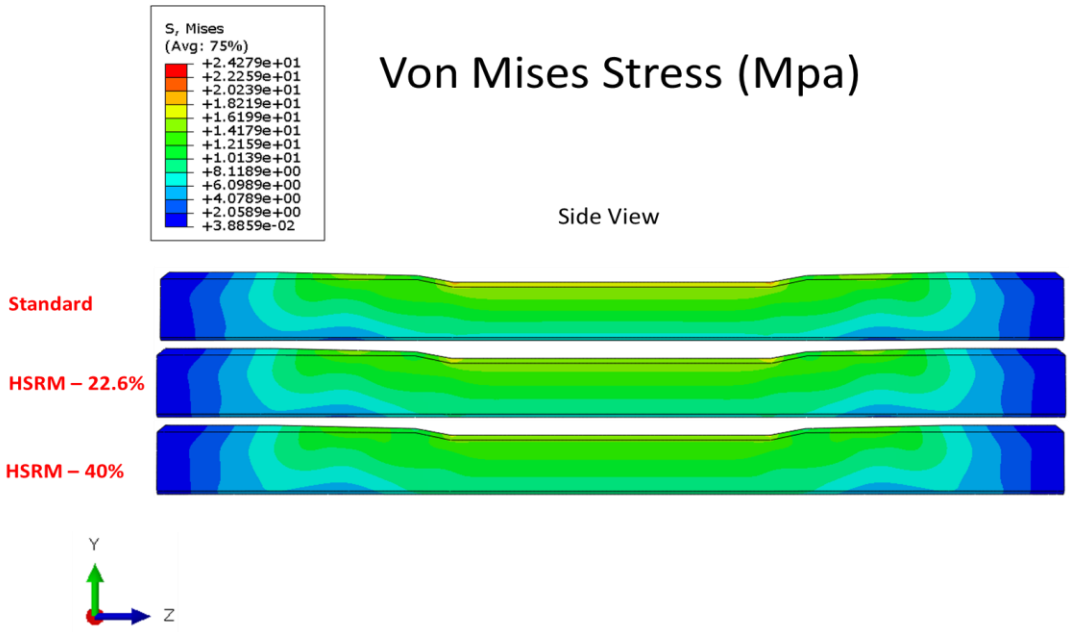

Figure 6.49: Von Mises stress map with a side view for each concrete tie. Support type: End supported, Load case: L/V = 0

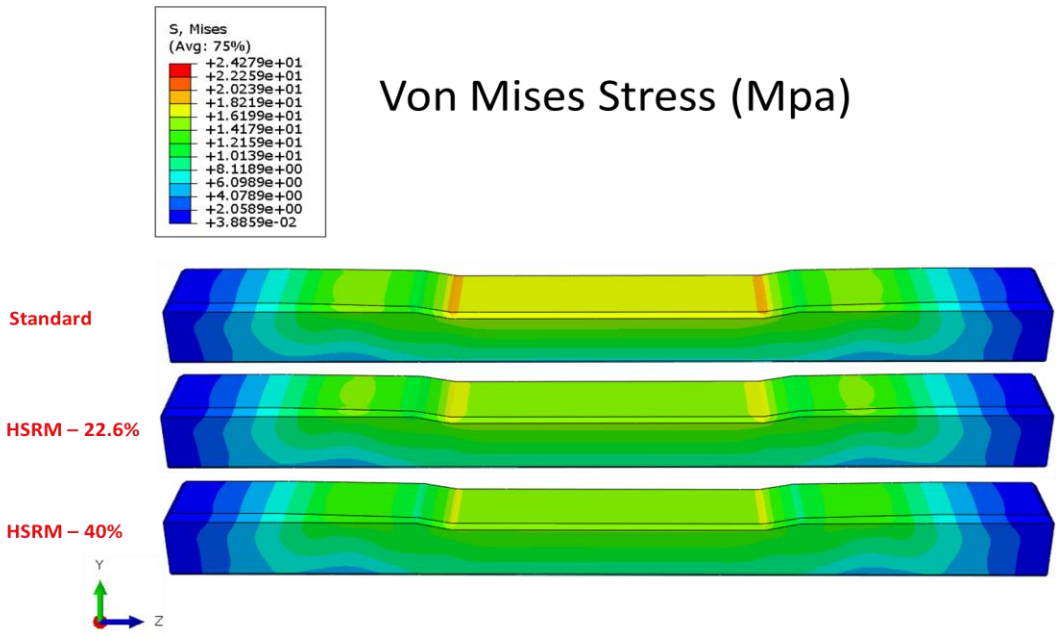

Figure 6.50: Von Mises stress map with a rotated view for each concrete tie. Support type: End supported, Load case: L/V = 0

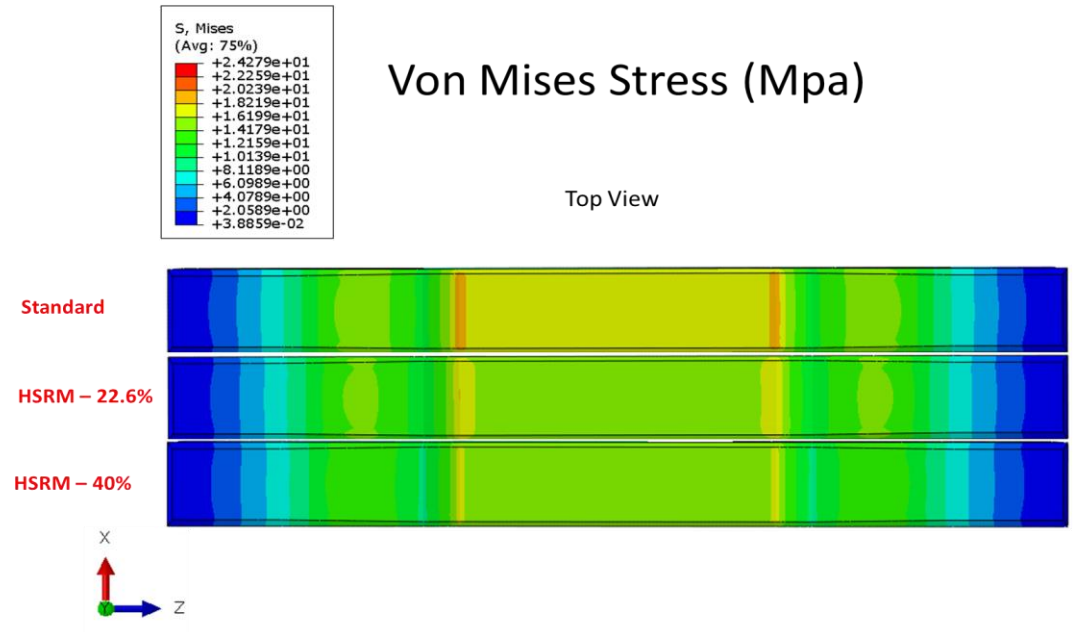

Figure 6.51: Von Mises stress map with a top view for each concrete tie. Support type: End supported, Load case: L/V = 0

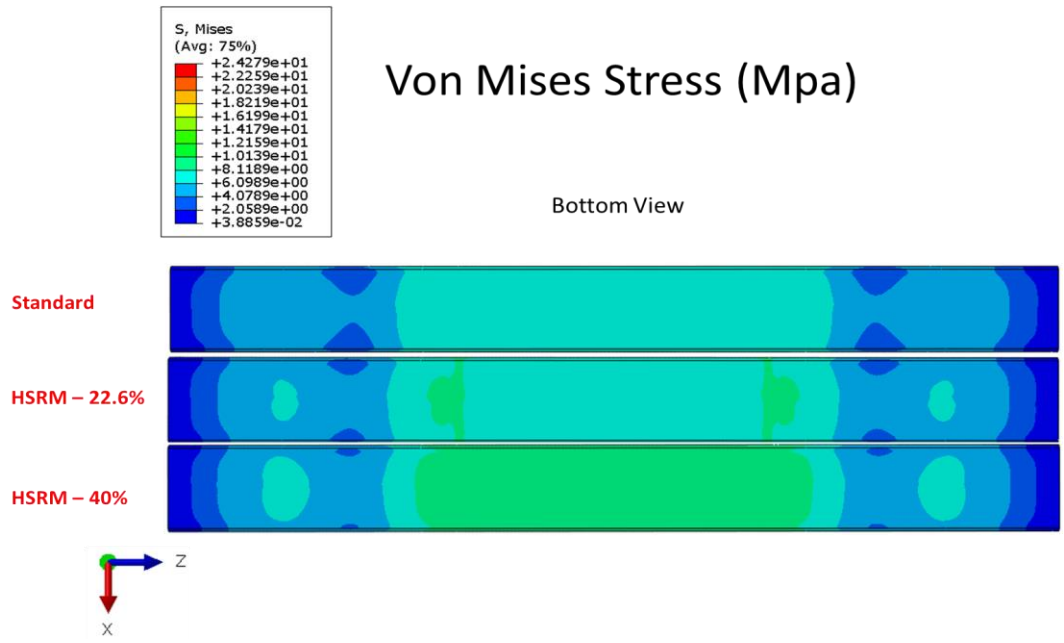

Figure 6.52: Von Mises stress map with a bottom view for each concrete tie. Support type: End supported, Load case: L/V = 0

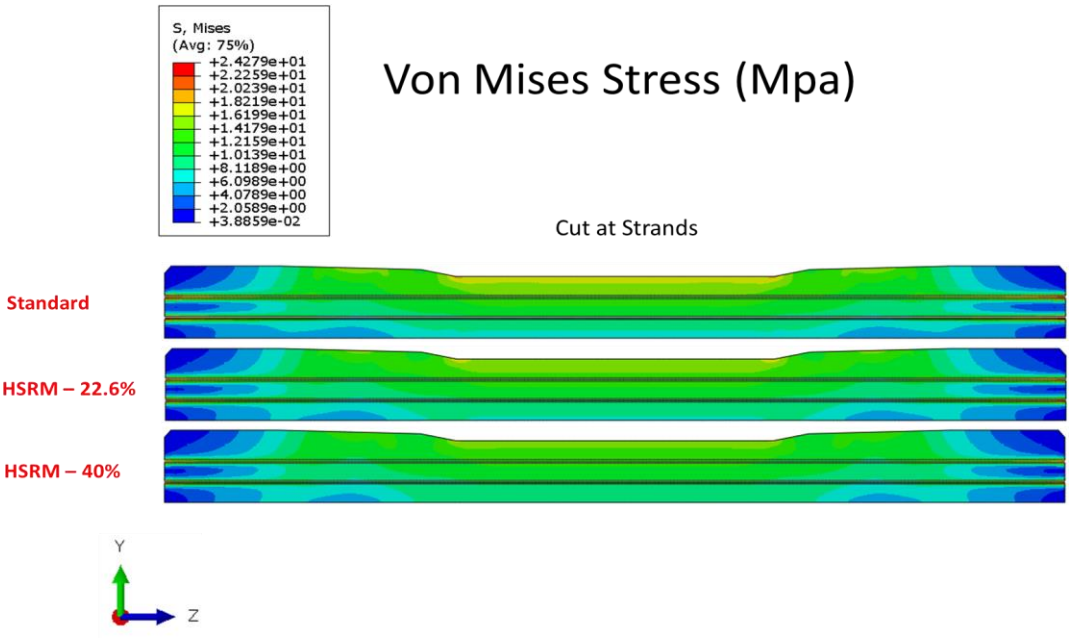

Figure 6.53: Von Mises stress map inside the tie, at the inside strand, for each concrete tie. Support type: End supported, Load case: L/V = 0

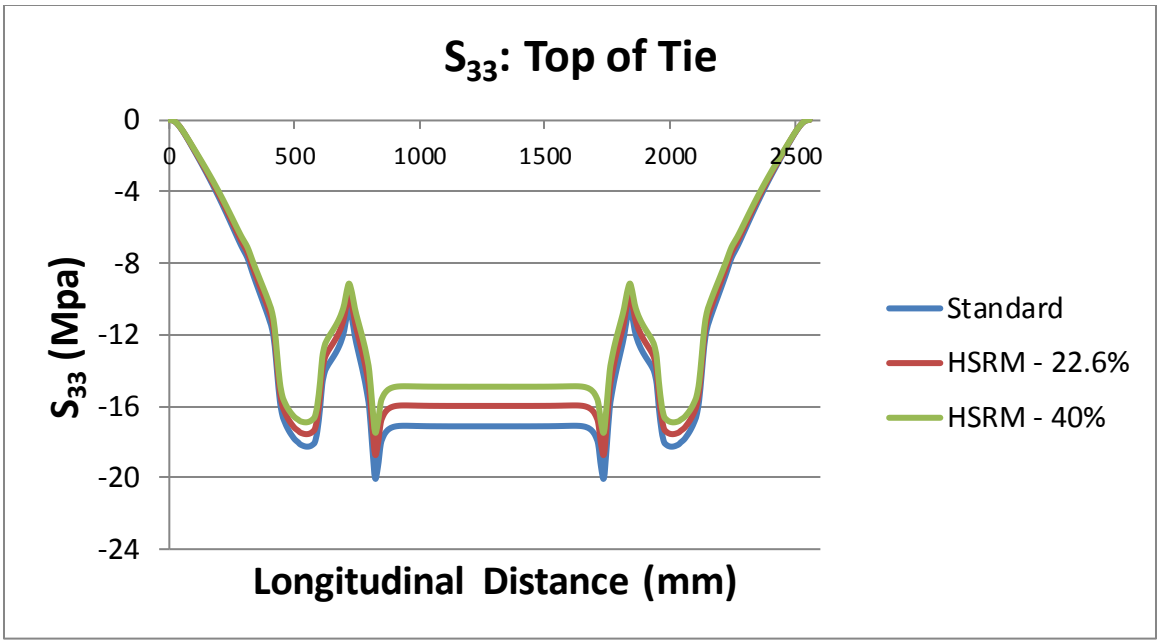

Figure 6.54: Plot of the longitudinal stress along the top fibers of each concrete tie. Support type: End supported, Load case: L/V = 0

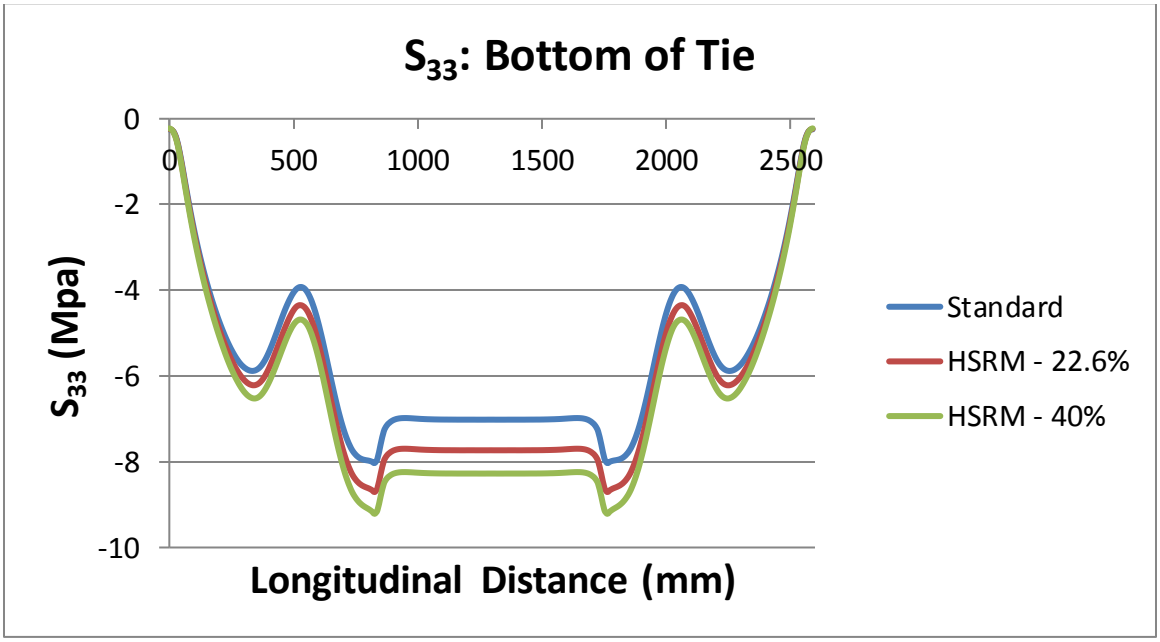

Figure 6.55: Plot of the longitudinal stress along the bottom fibers of each concrete tie. Support type: End supported, Load case: L/V = 0

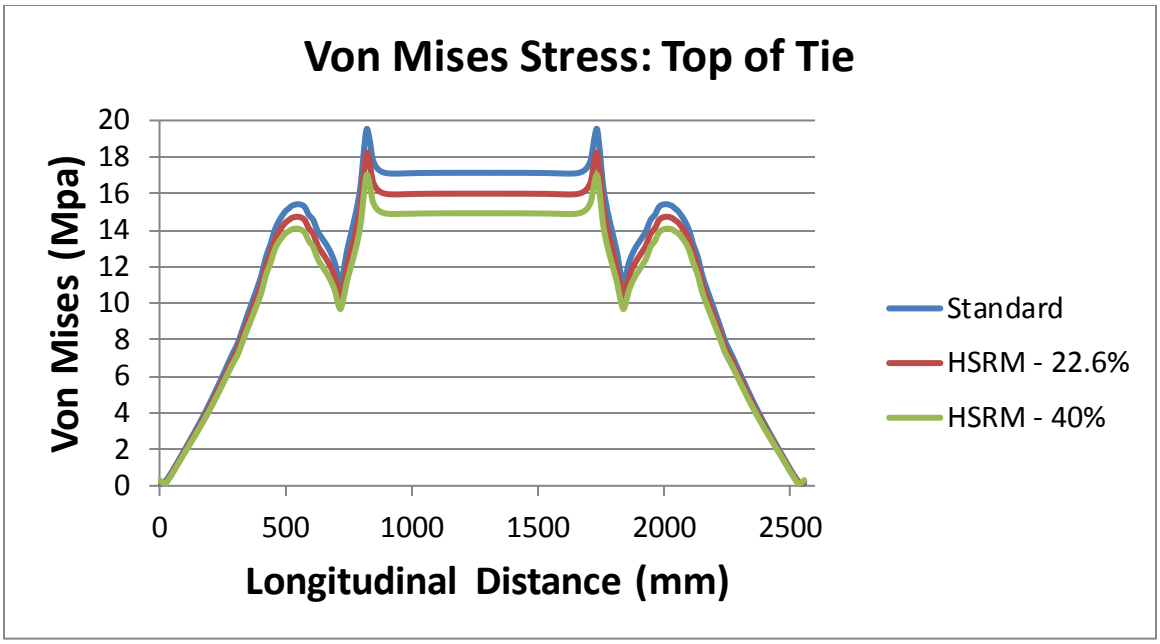

Figure 6.56: Plot of von Mises stress along the top fibers of each concrete tie. Support type: End supported, Load case: L/V = 0

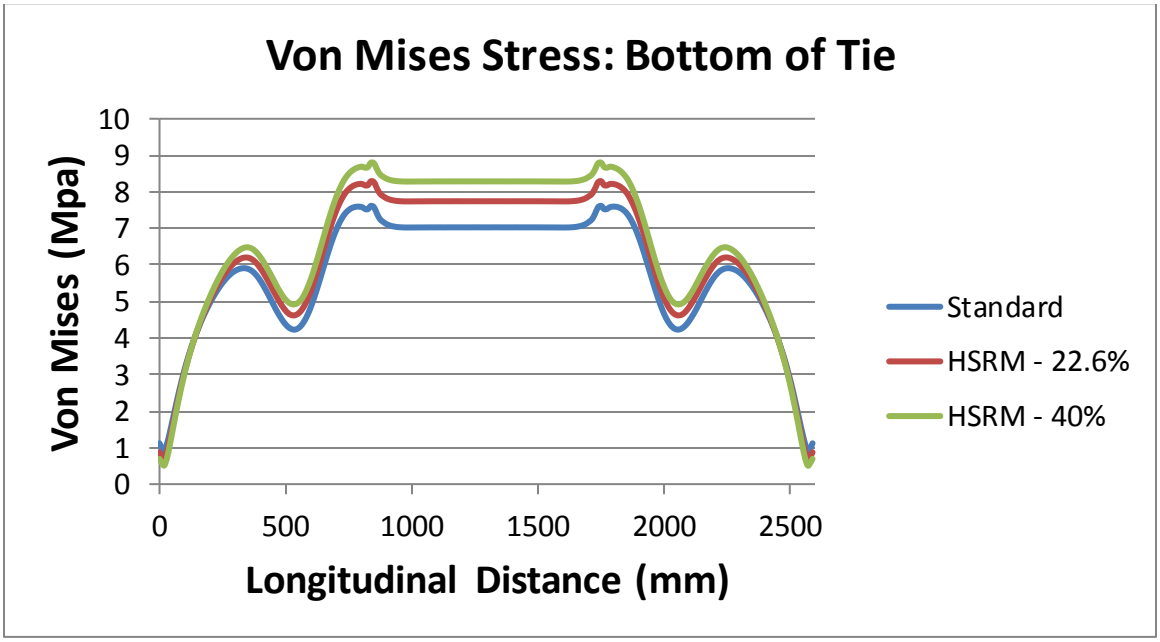

Figure 6.57: Plot of von Mises stress along the bottom fibers of each concrete tie. Support type: End supported, Load case: L/V = 0

Load Case: L/V = .6

A 40 kip vertically applied load is distributed over each rail seat area and one 24 Kip laterally applied load is distributed over one of the rail seat areas for the L/V = .6 load case, as discussed in the "Loads and Boundary Conditions" section of Chapter 5 (Figure 6.58). The deformed shape, longitudinal stresses (S_{33}), and von Mises Stresses throughout the tie are recorded and presented in Figures (6.59-6.69). Stress maps are superimposed onto the tie for visualization. Additionally, stresses along the top and bottom fibers of the concrete tie are measured along its length and are presented in Figures (6.70-6.73). Figures (6.60-6.69) presented below are adjusted to the same scale for comparison.

No damage is observed in the tie during the loading procedure. The standard, HSRM-22.6% and HSRM-40% concrete ties appear to remain in a compressive state after the analysis step has concluded. The deformed shape suggests that an increase in load will cause the bottom region of the concrete tie, underneath the right rail seat or approximately 21.6 in. (548.6 mm) from the tie end, to shift towards a tensile state and presents this region as a likely candidate for crack initiation. This claim is supported by Figure (6.71), which shows the previously described region having almost transitioned to a tensile state. Additionally, the compressive stresses located at the top right region of the concrete tie, approximately 32 in. (812.8 mm) from the tie end, appear to be growing in magnitude with an increase in load. Therefore, the stresses located at these locations are reported and used for comparison. It is obvious that the concrete tie which

exhibits higher and lower compressive stresses in the bottom and top regions mentioned above is preferred.

The longitudinal stress (S_{33}) measured in the top fibers, approximately 32 in. (812.8 mm) from the right tie end, of the standard, HSRM-22.6%, and HSRM-40% concrete tie is -3,315.6 psi (-22.86 Mpa), -3,114.1 psi (-21.5 Mpa), and -2,916.1 psi (-20.1 Mpa). The longitudinal stress (S_{33}) measured in the bottom fibers, approximately 21.6 in. (548.6 mm) from the right tie end, of the standard, HSRM-22.6%, and HSRM-40% concrete tie is -110.7 psi (-.763 Mpa), -196.8 psi (-1.36 Mpa), and -275.7 psi (-1.90 Mpa). The von Mises Stress measured in the top fibers, approximately 32 in. (812.8 mm) from the right tie end, of the standard, HSRM-22.6%, and HSRM-40% is 3,228.4 psi (22.26 Mpa), 3,032.2 psi (20.91 Mpa), and 2,839.5 psi (19.58 Mpa). The von Mises Stress measured in the bottom fibers, approximately 21.6 in. (548.6 mm) from the right tie end, of the standard, HSRM-22.6%, and HSRM-40% is 227.4 psi (1.57 Mpa), 281.1 psi (1.94 Mpa), and 340.3 psi (2.35 Mpa). Both the HSRM-22.6% and HSRM-40% concrete tie appear to outperform the standard tie, with the HSRM-40% showing the most desirable response of better distributing the stresses throughout the tie. For the HSRM-22.6% concrete tie, an approximate 6.1% decrease and 77.8% increase in the magnitude of the compressive stresses at the top and bottom fibers of the concrete tie are observed, when compared to the standard tie. For the HSRM-40% concrete tie, an approximate 12.1% decrease and 149.2% increase in the compressive stresses seen at the center top and bottom fibers of the concrete tie are observed, when compared to the standard tie.

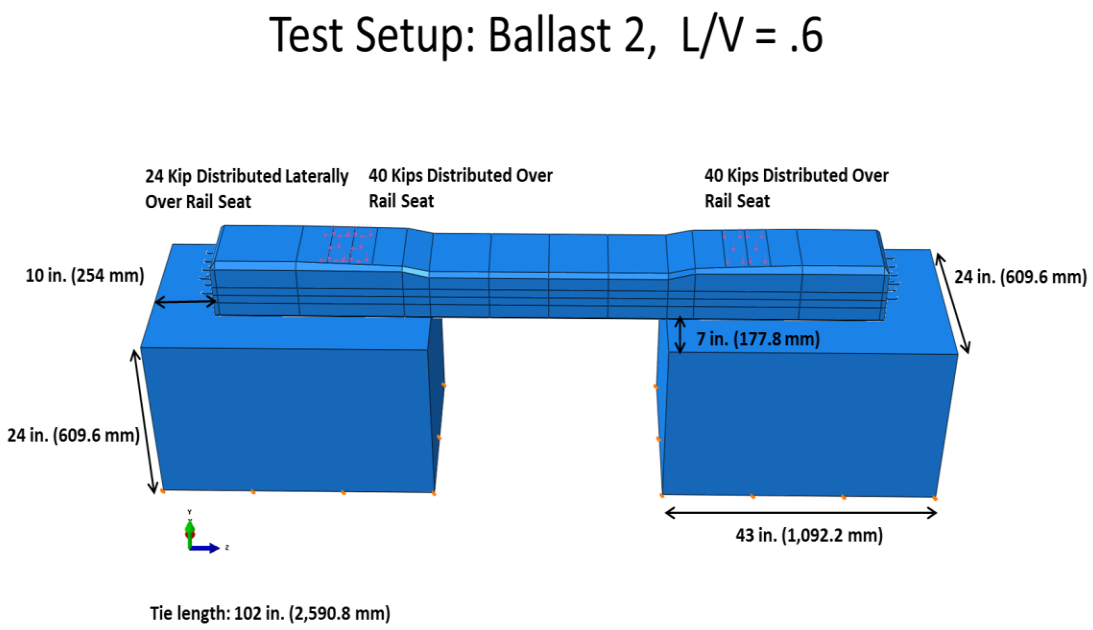

Figure 6.58: Test setup for the end supported tie with the load case of L/V = .6

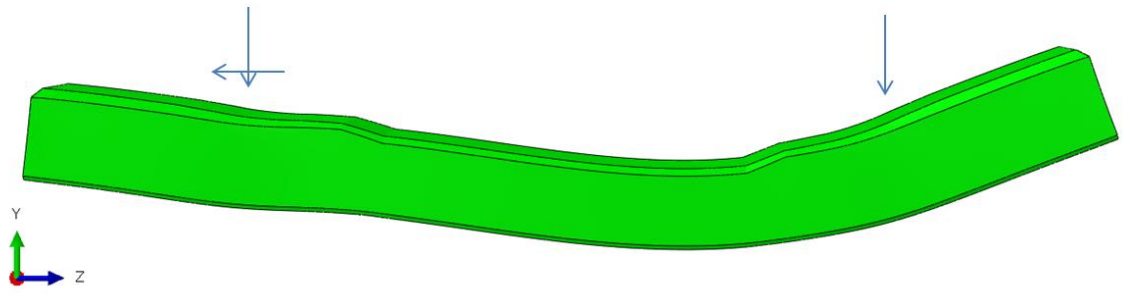

Figure 6.59: Deformed shape of the concrete tie for the end supported tie with the L/V = .6 load case

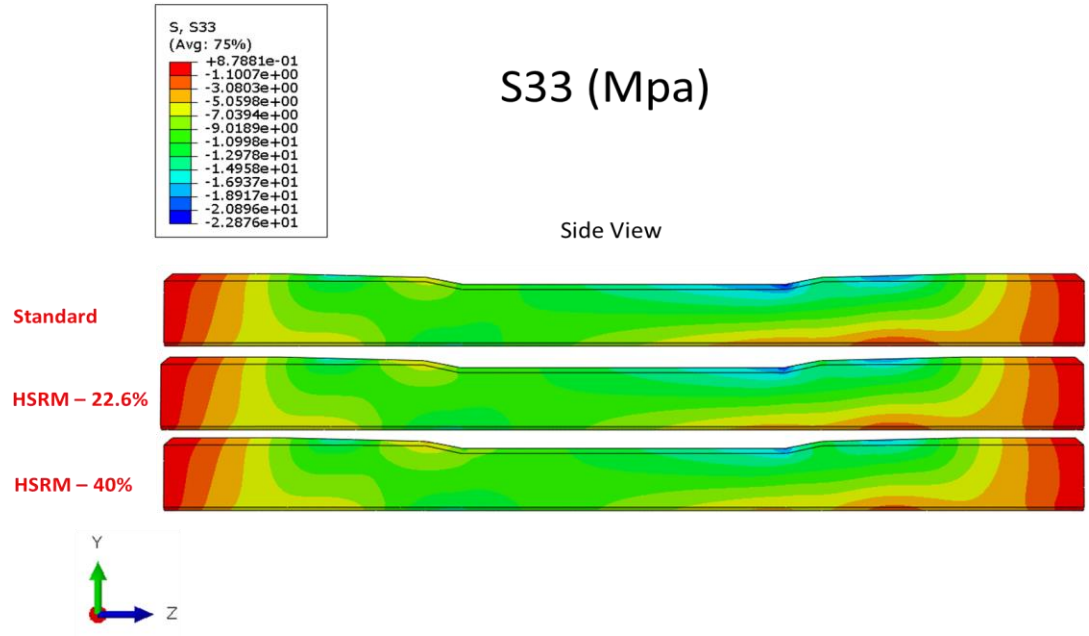

Figure 6.60: Longitudinal stress map with a side view for each concrete tie. Support type: End supported, Load case: L/V = .6

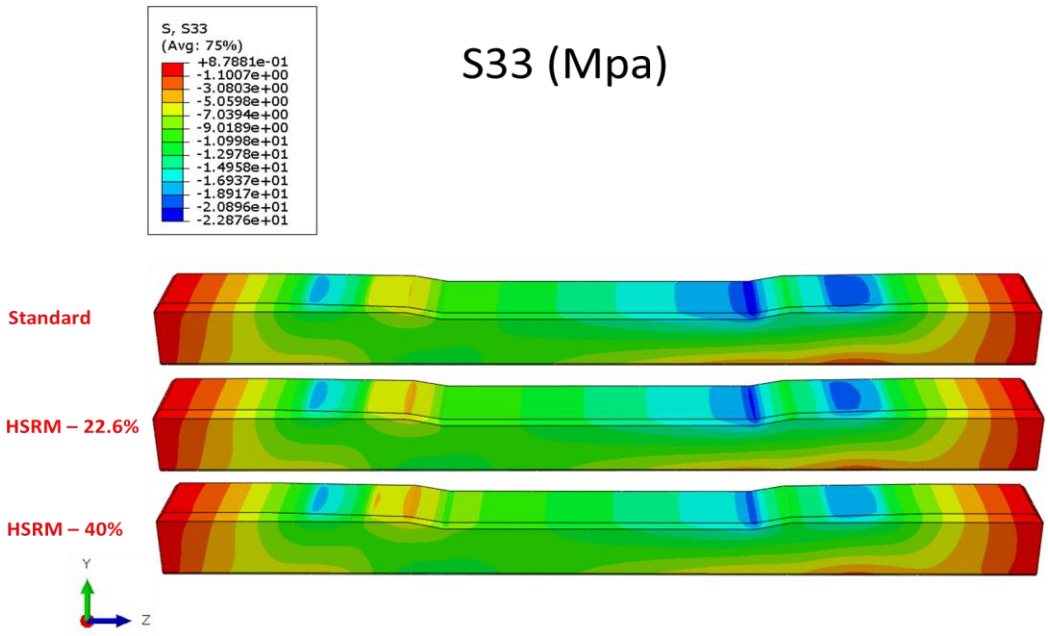

Figure 6.61: Longitudinal stress map with a rotated view for each concrete tie. Support type: End supported, Load case: L/V = .6

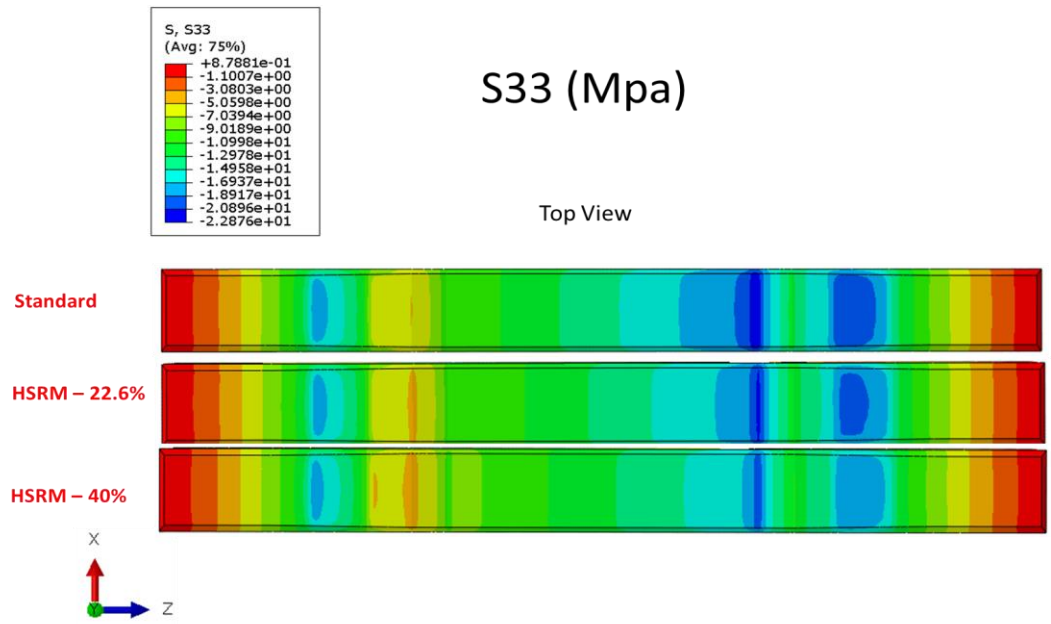

Figure 6.62: Longitudinal stress map with a top view for each concrete tie. Support type: End supported, Load case: L/V = .6

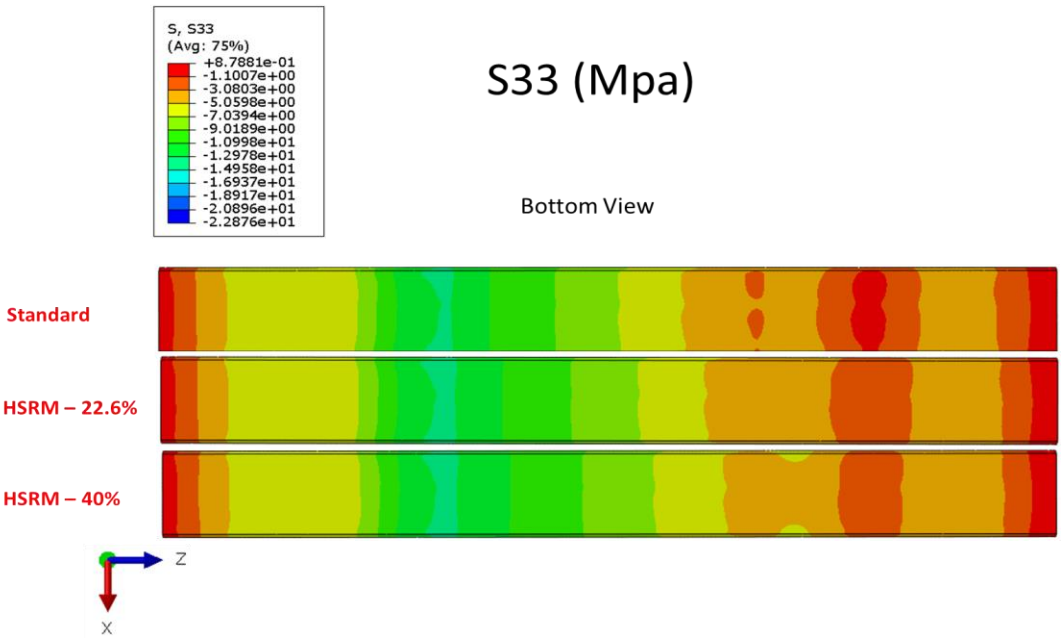

Figure 6.63: Longitudinal stress map with a bottom view for each concrete tie. Support type: End supported, Load case: L/V = .6

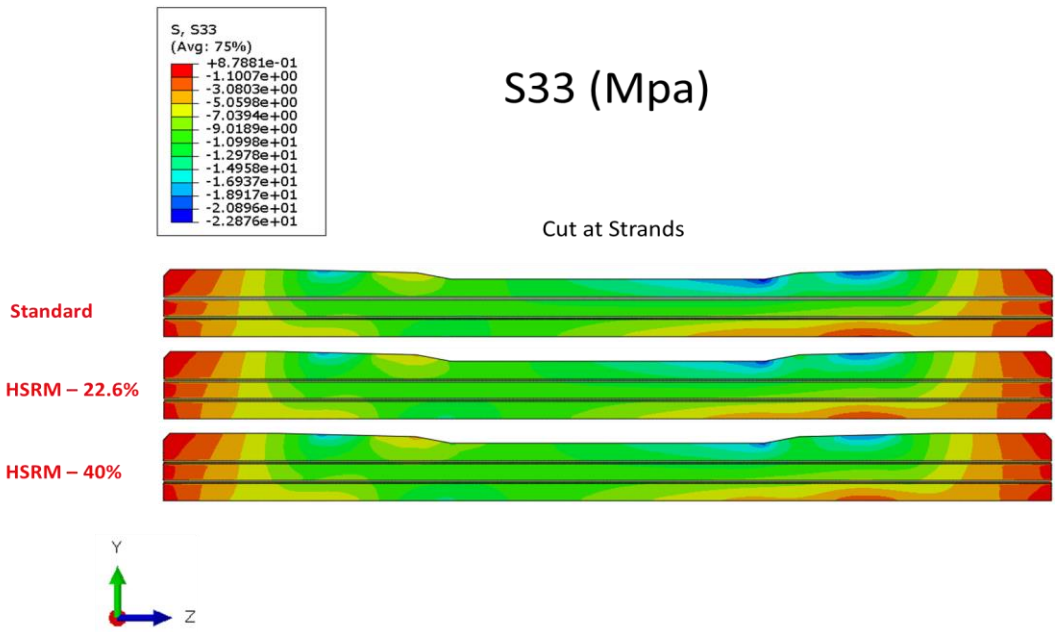

Figure 6.64: Longitudinal stress map inside the tie, at the inside strand, for each concrete tie. Support type: End supported, Load case: L/V = .6

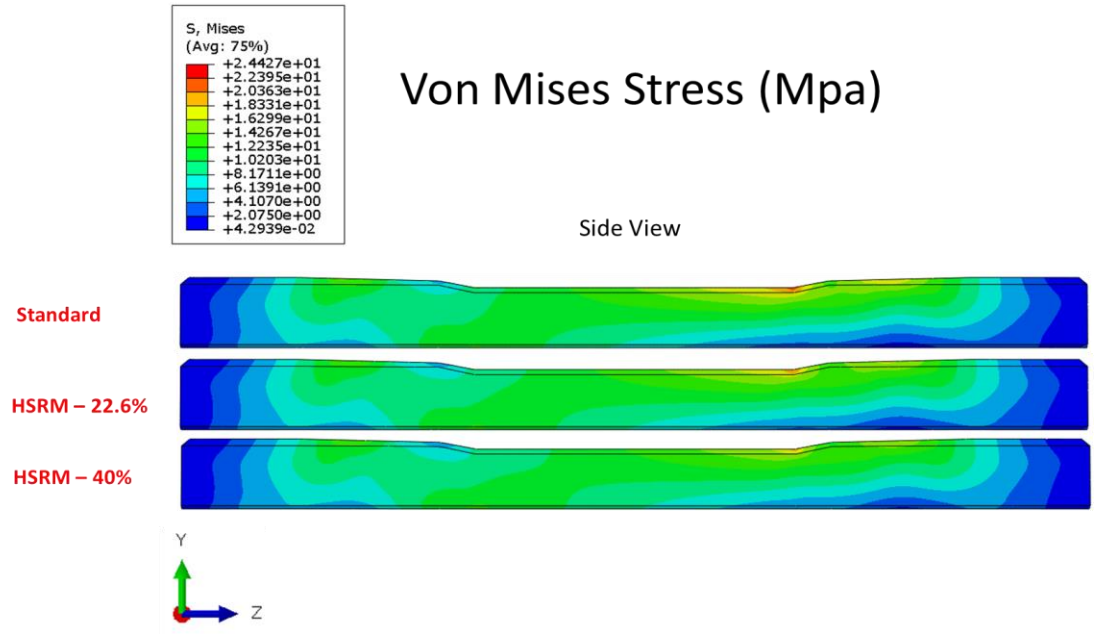

Figure 6.65: Von Mises stress map with a side view for each concrete tie. Support type: End supported, Load case: L/V = .6

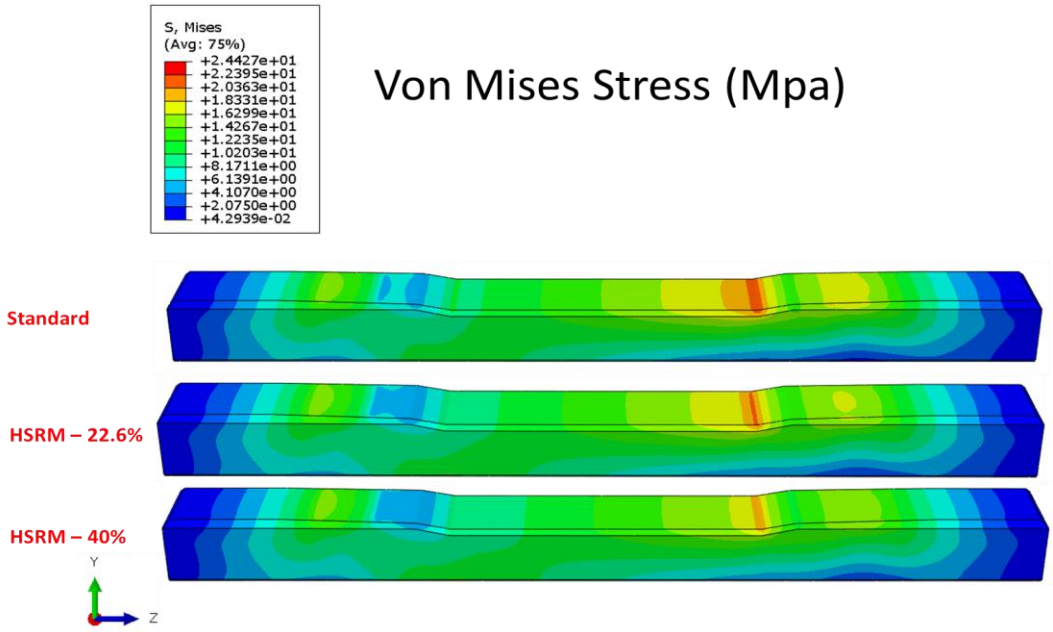

Figure 6.66: Von Mises stress map with a rotated view for each concrete tie. Support type: End supported, Load case: L/V = .6

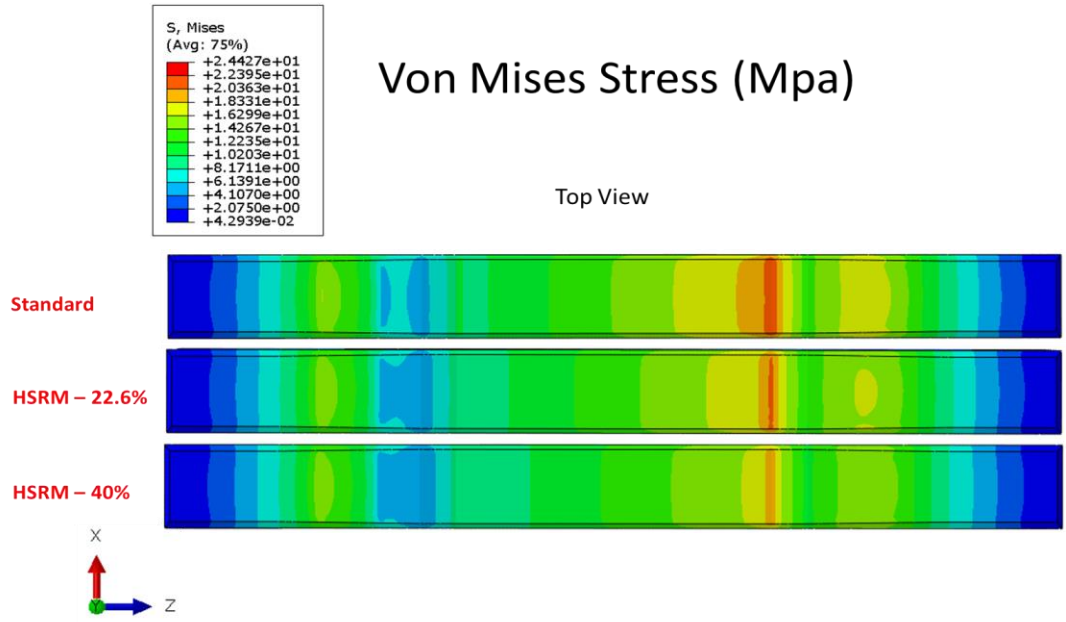

Figure 6.67: Von Mises stress map with a top view for each concrete tie. Support type: End supported, Load case: L/V = .6

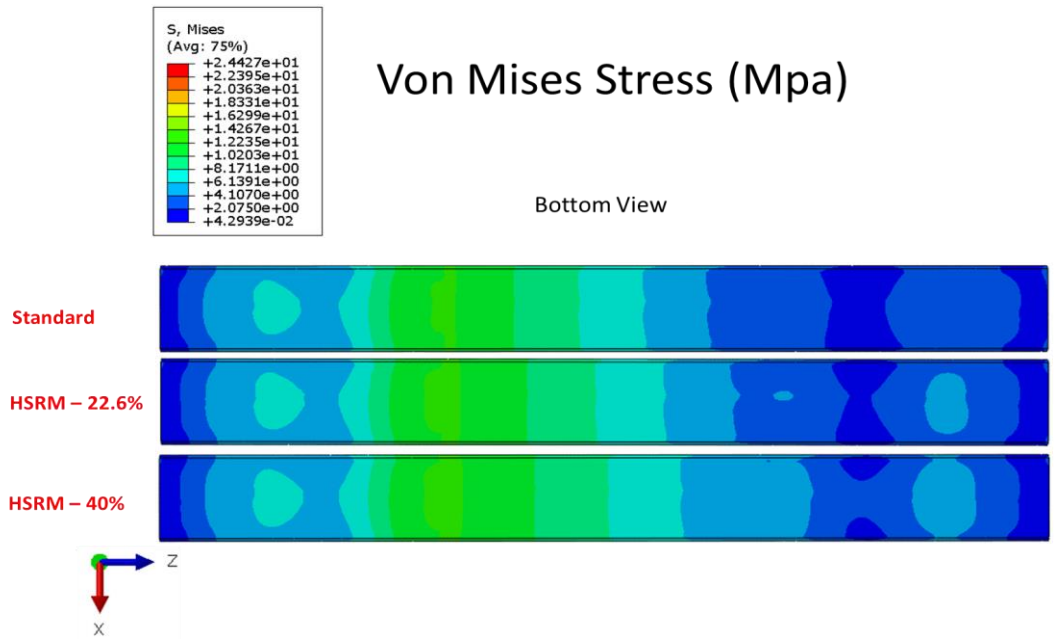

Figure 6.68: Von Mises stress map with a bottom view for each concrete tie. Support type: End supported, Load case: L/V = .6

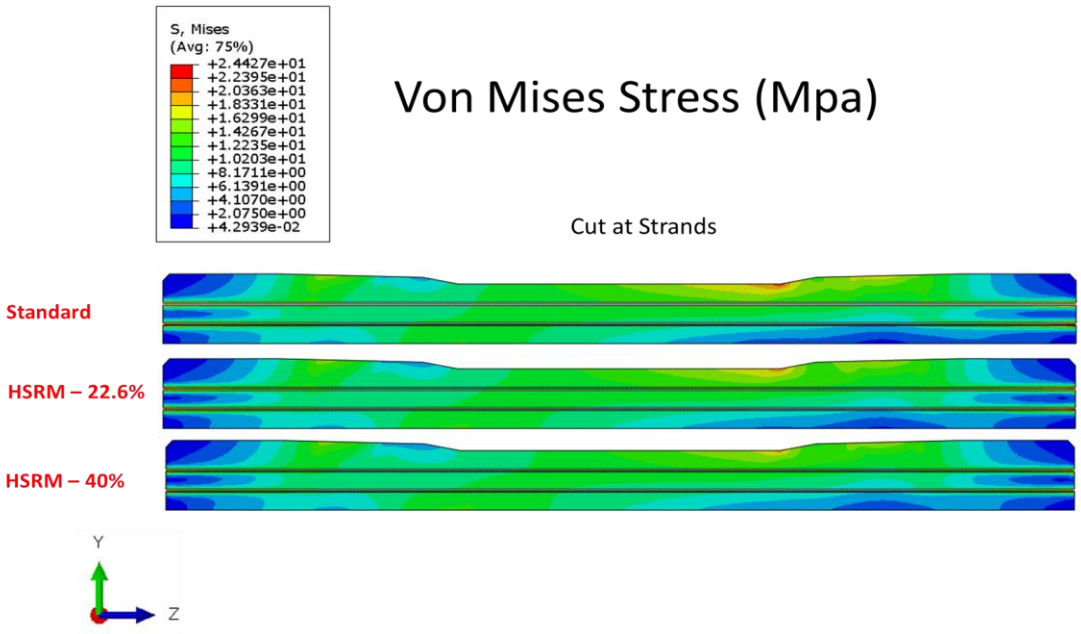

Figure 6.69: Von Mises stress map inside the tie, at the inside strand, for each concrete tie. Support type: End supported, Load case: L/V = .6

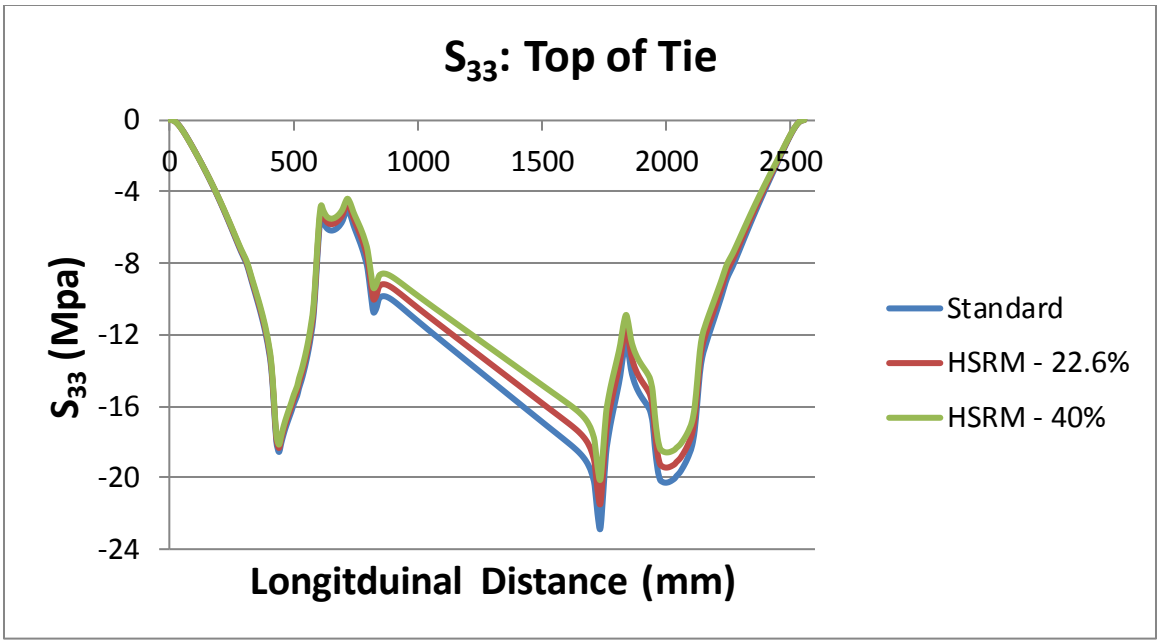

Figure 6.70: Plot of the longitudinal stress along the top fibers of each concrete tie. Support type: End supported, Load case: L/V = .6

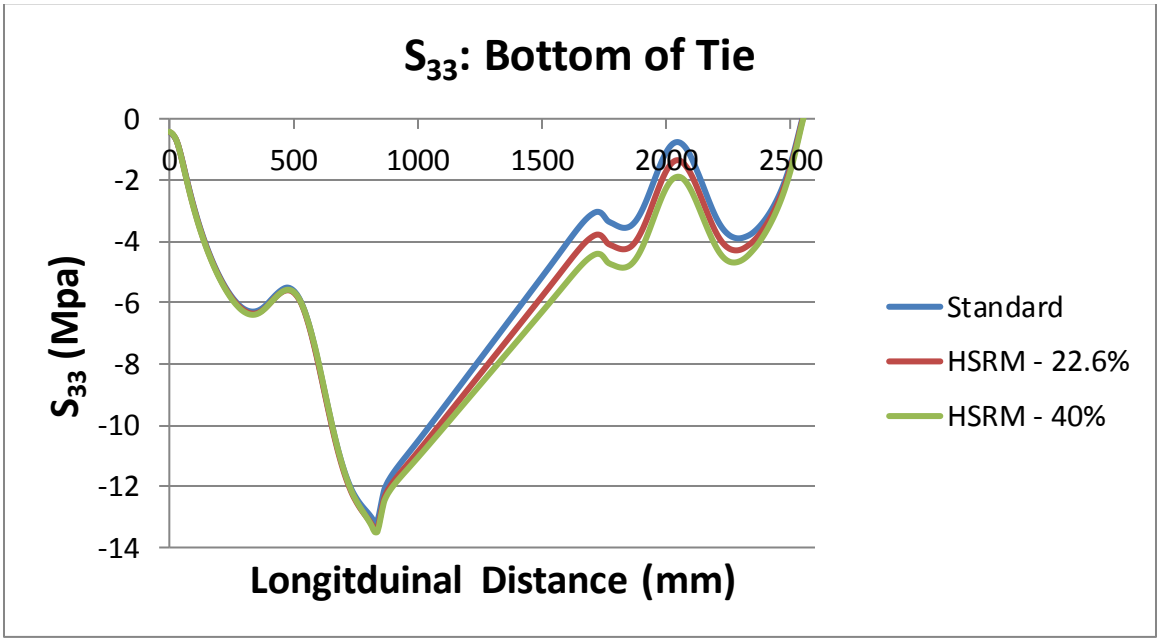

Figure 6.71: Plot of the longitudinal stress along the bottom fibers of each concrete tie. Support type: End supported, Load case: L/V = .6

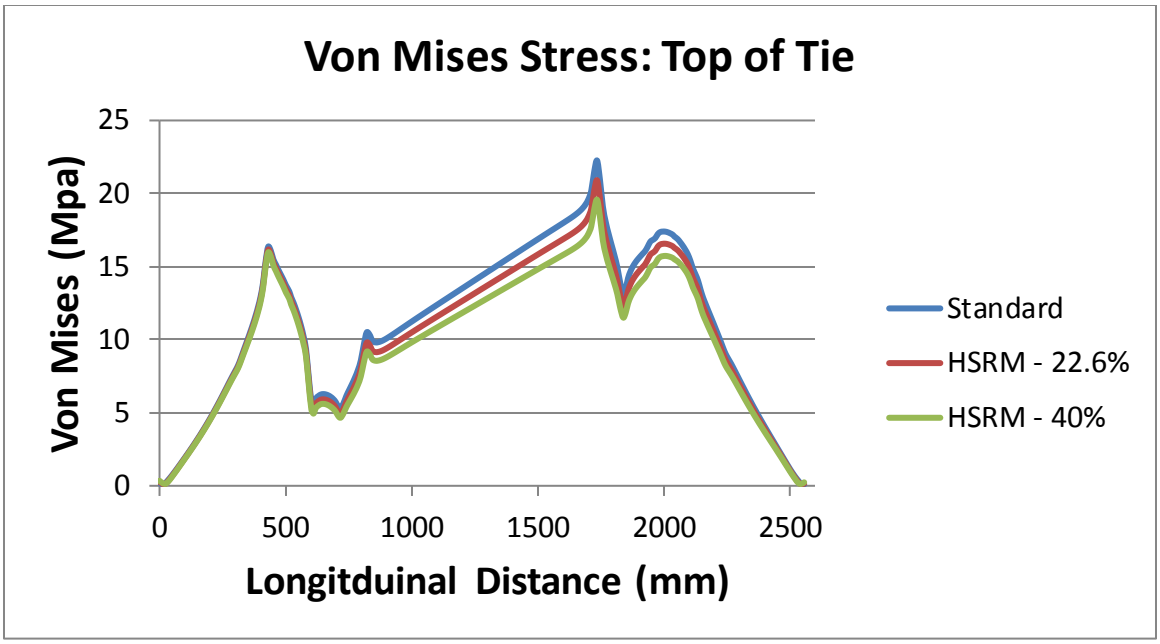

Figure 6.72: Plot of von Mises stress along the top fibers of each concrete tie. Support type: End supported, Load case: L/V = .6

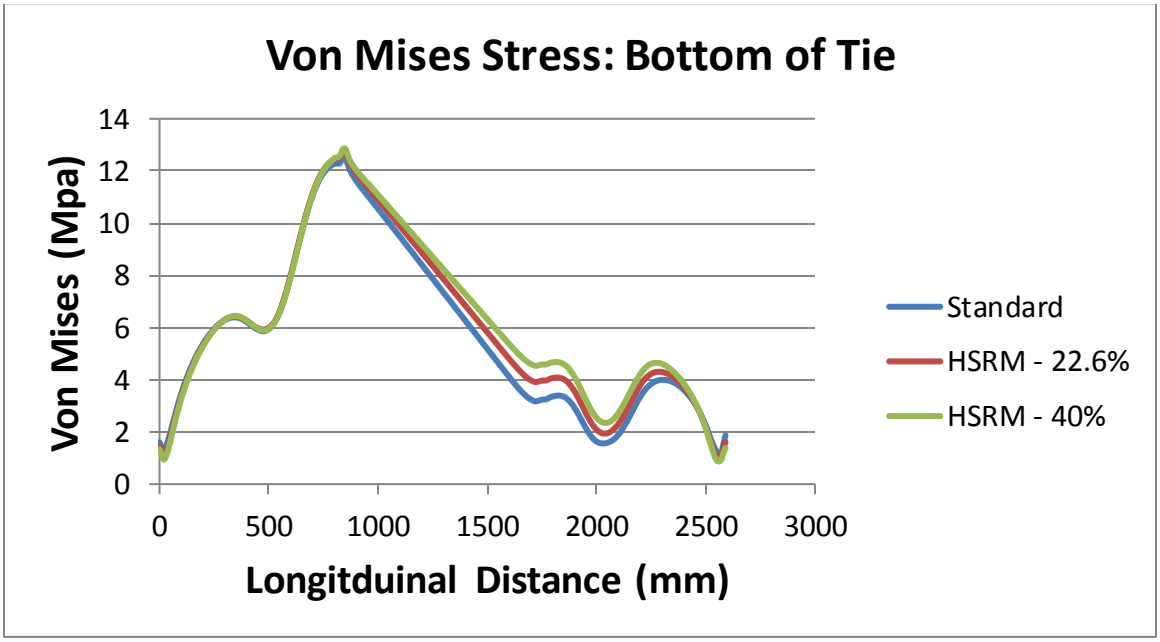

Figure 6.73: Plot of von Mises stress along the bottom fibers of each concrete tie. Support type: End supported, Load case: L/V = .6

Center Binding Support

Load Case: L/V = 0

A 40 kip, vertically applied load, is distributed over each rail seat area for the L/V = 0 load case, as discussed in the "Loads and Boundary Conditions" section of Chapter 5 (Figure 6.74). However, the analysis step for each of the three tie models aborted due to convergence issues, which is attributed to the onset of cracks and damage in the concrete ties during the loading procedure. Consequently, the deformed shape, longitudinal stress (S_{33}), and von Mises Stresses throughout the tie are recorded due to a total vertically applied load of 36 Kips because no cracking has taken place at this load (Figures (6.75-6.85). This gives insight into the behavior of the concrete ties before any damage has initiated. The deformed shape, longitudinal stress maps, and von Mises stress maps are presented in the figures below by superimposing the stresses onto the tie for visualization. Longitudinal and von Mises stresses at 36 Kips of total applied load are recorded along the top and bottom fibers of the concrete and graphed in Figures (6.86-6.89). Furthermore, longitudinal stresses along the top fibers of the concrete tie are recorded and graphed for a series of different loads to demonstrate the behavior of the tie before cracking has taken place and the redistribution of stresses after cracking (Figures 6.90-6.92). Finally, the progression of tensile damage in the concrete is documented and presented in Figures (6.93-6.95).

The deformed shape of the tie depicts a negative bending moment causing the top fibers to be inclined to a tensile behavior and the bottom fibers to be inclined to a

compressive behavior. With regards to the three concrete tie models, it is apparent that the concrete tie that has a lower magnitude of tensile stress in its top fibers and lower magnitude of compressive stresses in its bottom fibers, under the same load, is preferred.

The longitudinal stress (S_{33}) measured at the top middle fibers of the standard, HSRM-22.6%, and HSRM-40% concrete tie, due to a total applied load of 36 Kips or 18 Kips applied at each rail seat, is 744.0 psi (5.13 Mpa), 551.3 psi (3.80 Mpa), and 358.7 (2.47 Mpa). The longitudinal stress (S_{33}) measured at the bottom middle fibers of the standard, HSRM-22.6%, and HSRM-40% concrete tie, due to a total applied load of 36 Kips or 18 Kips applied at each rail seat, is -3,795.3 psi (-26.17 Mpa), -3,537.6 psi (-24.39 Mpa), and -3,270.0 psi (-22.55 Mpa). The von Mises Stress measured at the top middle fibers of the standard, HSRM-22.6%, and HSRM-40% concrete tie is 743.8 psi (5.13 Mpa), 551.4 psi (3.80 Mpa), and 359.0 psi (2.48 Mpa). The von Mises Stress measured at the bottom middle fibers of the standard, HSRM-22.6%, and HSRM-40% concrete tie is 3,792.6 psi (26.15 Mpa), 3,537.5 psi (24.39 Mpa), and 3,272.2 psi (22.56 Mpa). Both the HSRM-22.6% and HSRM-40% concrete tie appear to outperform the standard tie, with the HSRM-40% showing the most desirable response of better distributing the stresses throughout the tie, at a load of 36 Kips. For the HSRM-22.6% concrete tie, a 25.9% decrease in the tensile stresses and a 6.79% decrease in the compressive stresses are observed at the middle top and bottom fibers of the concrete tie, when compared to the standard tie. For the HSRM-40% concrete tie, a 51.8% decrease in the tensile stresses and a 13.8% decrease in the compressive stresses are observed at the middle

top and bottom fibers of the concrete tie, when compared to the standard tie. Due to the higher tensile stresses observed in the standard concrete tie at an applied load of 36 Kips, one would expect cracks to initiate in the standard tie at a lower load than the two HSRM ties. Such was the case observed.

Tensile damage is observed in each of the three concrete tie simulations. The first crack is initiated in the standard concrete tie at a total applied load of 39 Kips or 19.5 Kips applied at each rail seat. The first crack is initiated in the HSRM-22.6% concrete tie at a total applied load of 41.84 Kips or 20.92 Kips applied at each rail seat. The first crack is initiated in the HSRM-40% concrete tie at a total applied load of 43.7 Kips or 21.85 Kips applied at each rail seat. Ensuing loading at each rail seat generates additional cracks, resulting in a redistribution of stresses throughout the tie. The damage evolution for the standard, HSRM-22.6%, and HSRM-40% tie is shown in Figures (6.93-6.95). The standard tie endured approximately 58.5 Kips of load before the simulation aborted due to convergence difficulties. The HSRM-22.6% tie endured approximately 61.47 Kips of load before the simulation aborted due to convergence difficulties. Finally, the HSRM-40% tie endured approximately 70.0 Kips of load before the simulation aborted due to convergence difficulties. The redistribution of stresses throughout the load history can be visualized in Figures (6.90-6.92). For the standard tie, the 12 Kip and 24 Kip load response show the linear behavior of the tie. The 36 Kip load response shows the response before the first crack has been initiated (39 kips). The 39 Kip, 41.73 Kip, 43 Kip, and 58.5 Kip load responses depict the redistribution of stresses in the top fibers of the concrete tie due to the formation of cracks. For the HSRM-22.6%

tie, the 12 Kip and 24 Kip load response show the linear behavior of the tie. The 40 Kip load response shows the response before the first crack has been initiated (41.84 kips). The 41.84 Kip, 43.5 Kip, 51.32 Kip, and 61.47 Kip load responses depict the redistribution of stresses in the top fibers of the concrete tie due to the formation of cracks. For the HSRM-40% tie, the 12 Kip and 24 Kip load response show the linear behavior of the tie. The 40 Kip load response shows the response before the first crack has been initiated (43.7 kips). The 43.7 Kip, 45.7 Kip, 55.7 Kip, and 70.0 Kip load responses depict the redistribution of stresses in the top fibers of the concrete tie due to the formation of cracks.

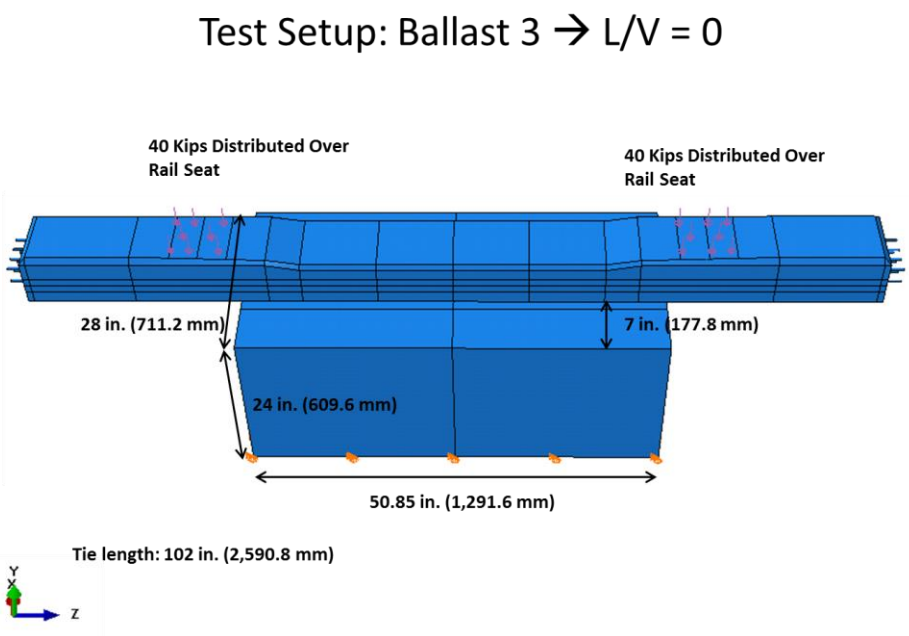

Figure 6.74: Test setup for the center binding supported tie with the load case of L/V = 0

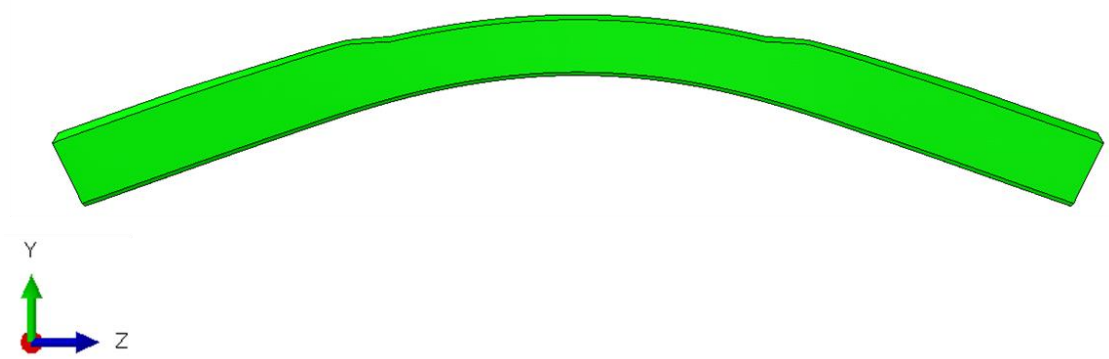

Figure 6.75: Deformed shape of the concrete tie for the center binding supported tie with the L/V = 0 load case

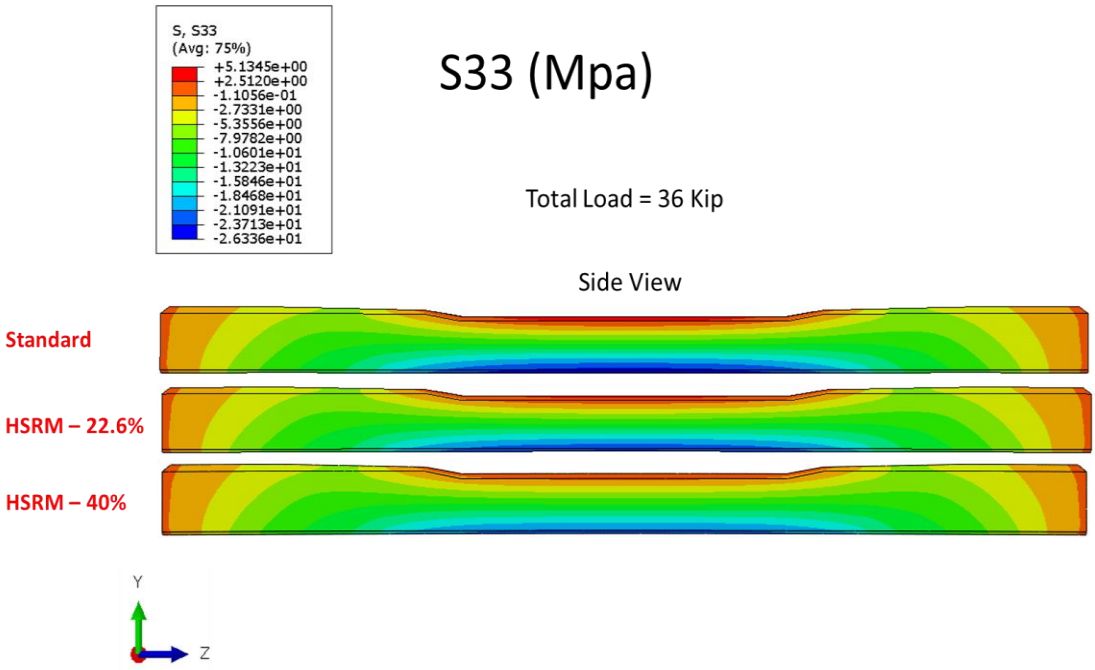

Figure 6.76: Longitudinal stress map with a side view for each concrete tie. Support type: Center binding support, Load case: L/V = 0. (Stresses are an outcome of 36 Kips of total load applied at the rail seats)

Figure 6.77: Longitudinal stress map with a rotated view for each concrete tie. Support type: Center binding support, Load case: L/V = 0. (Stresses are an outcome of 36 Kips of total load applied at the rail seats)

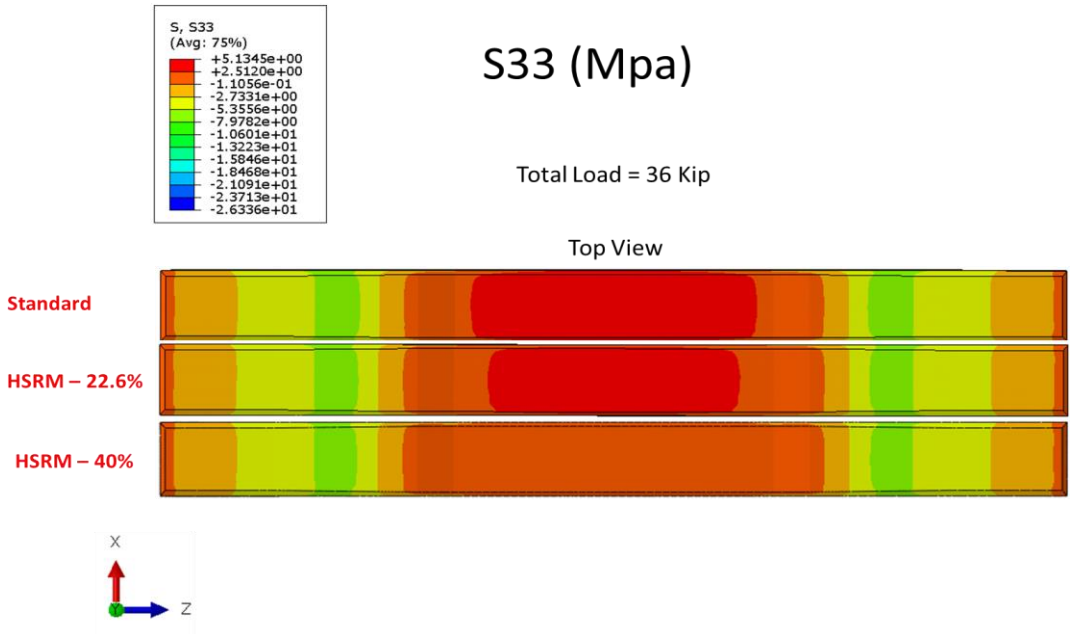

Figure 6.78: Longitudinal stress map with a top view for each concrete tie. Support type: Center binding support, Load case: L/V = 0. (Stresses are an outcome of 36 Kips of total load applied at the rail seats)

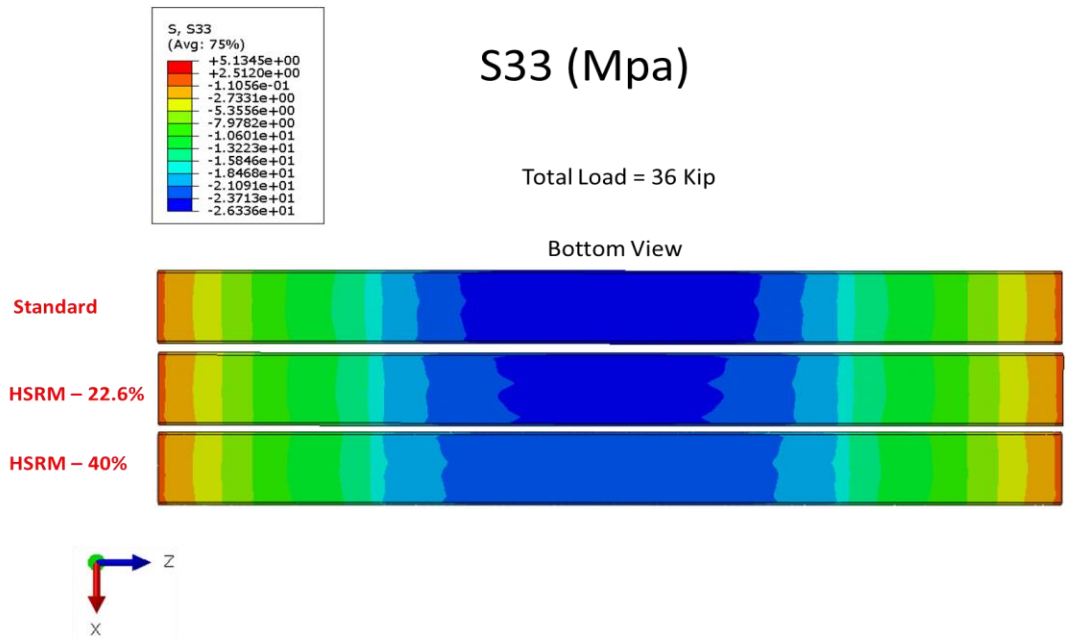

Figure 6.79: Longitudinal stress map with a bottom view for each concrete tie. Support type: Center binding support, Load case: L/V = 0. (Stresses are an outcome of 36 Kips of total load applied at the rail seats)

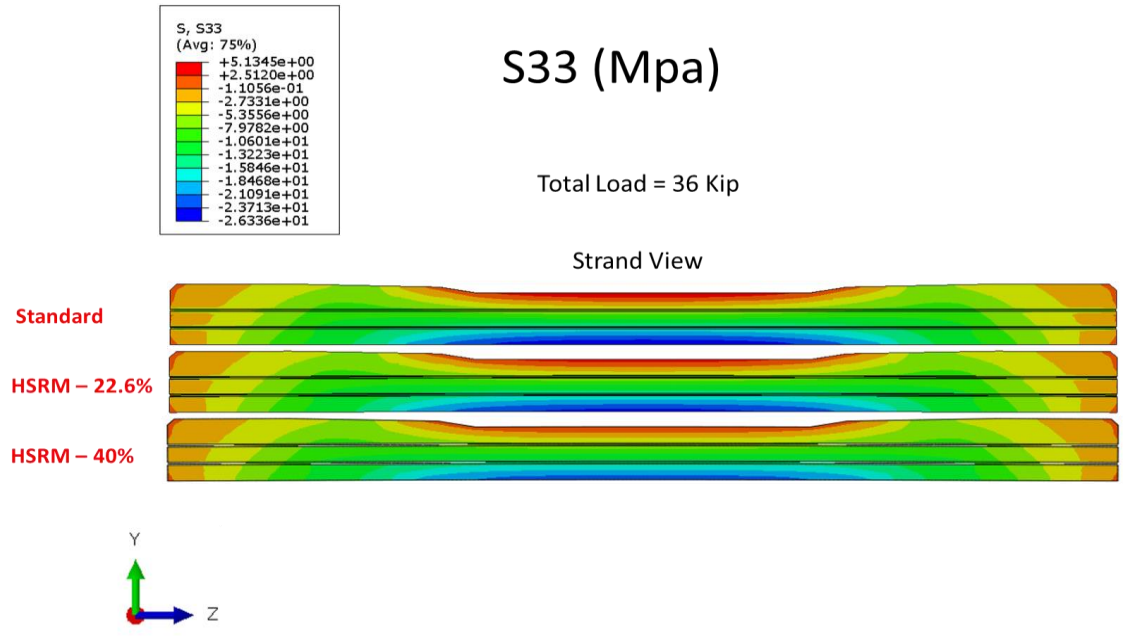

Figure 6.80: Longitudinal stress map inside the tie, at the inside strand, for each concrete tie. Support type: Center binding support, Load case: L/V = 0. (Stresses are an outcome of 36 Kips of total load applied at the rail seats)

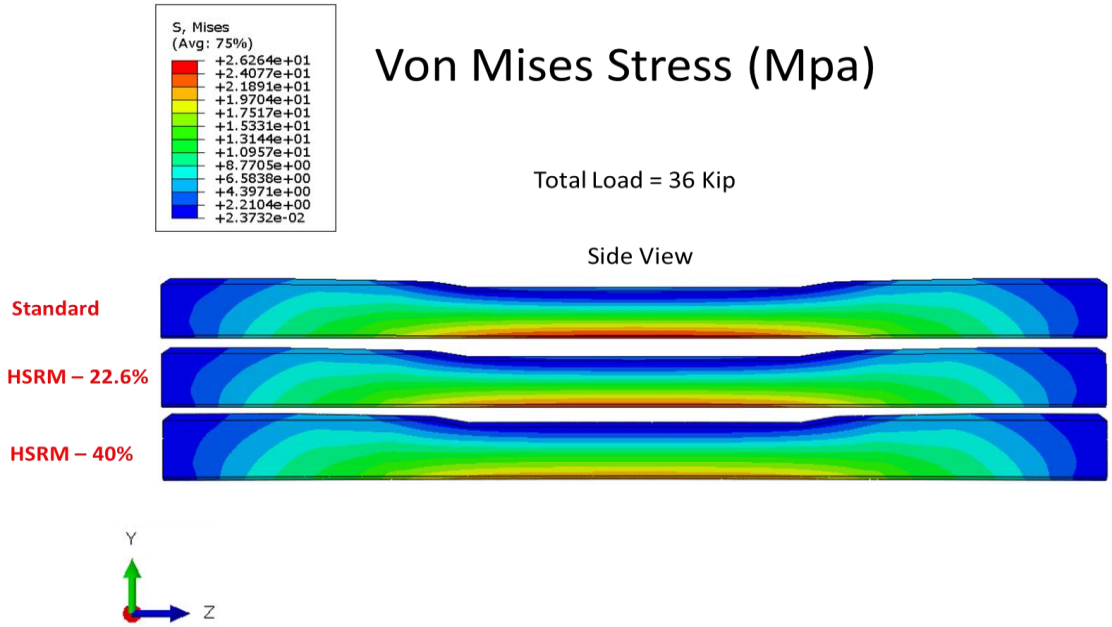

Figure 6.81: Von Mises stress map with a side view for each concrete tie. Support type: Center binding support, Load case: L/V = 0. (Stresses are an outcome of 36 Kips of total load applied at the rail seats)

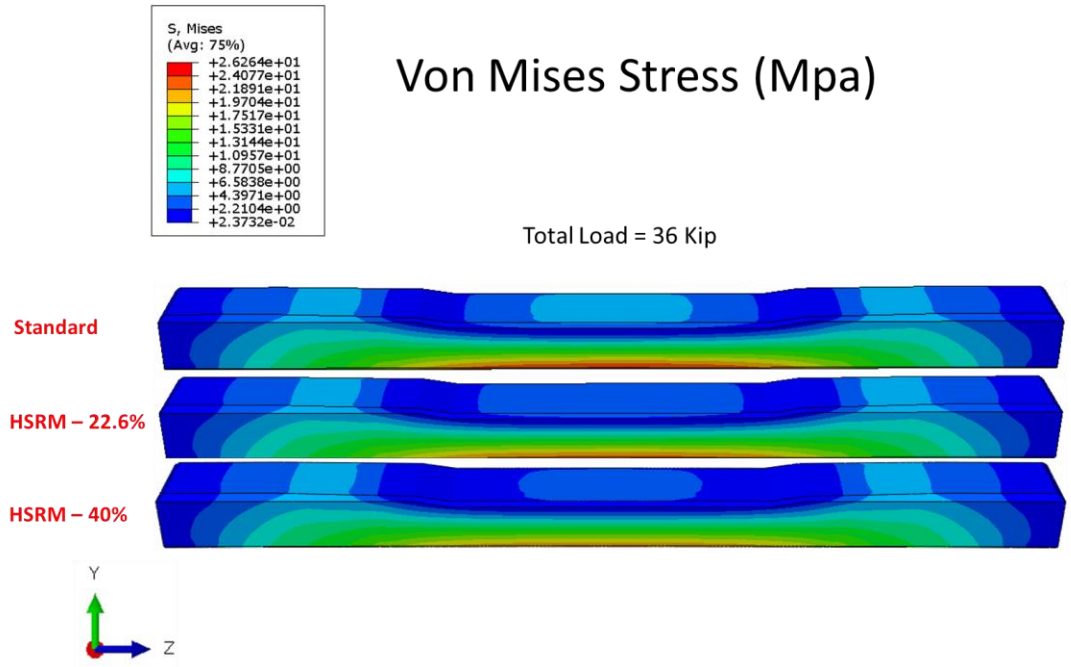

Figure 6.82: Von Mises stress map with a rotated view for each concrete tie. Support type: Center binding support, Load case: L/V = 0. (Stresses are an outcome of 36 Kips of total load applied at the rail seats)

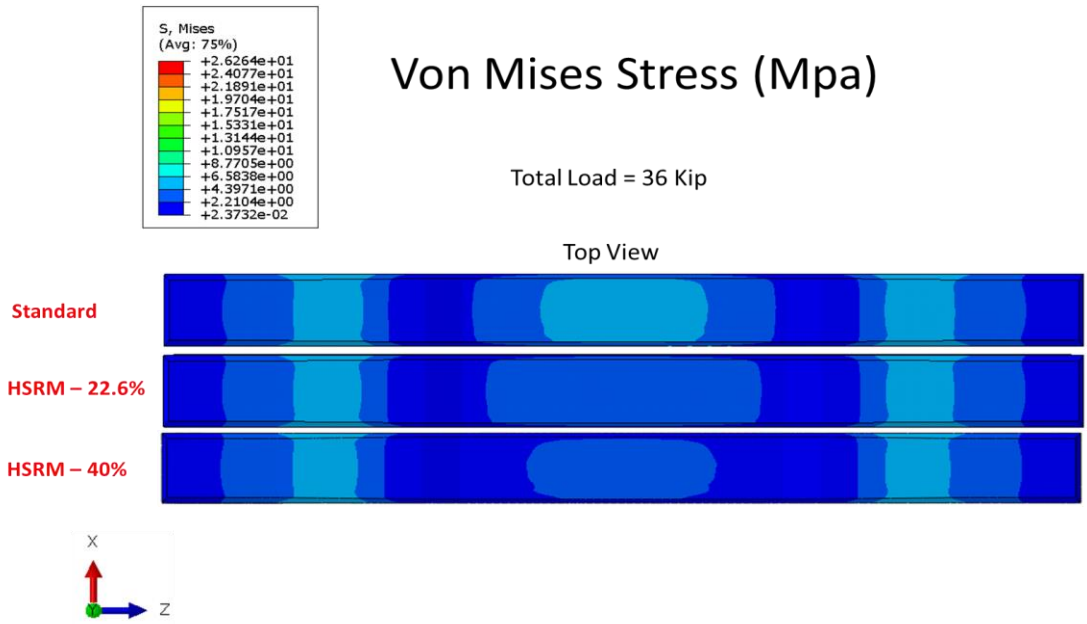

Figure 6.83: Von Mises stress map with a top view for each concrete tie. Support type: Center binding support, Load case: L/V = 0. (Stresses are an outcome of 36 Kips of total load applied at the rail seats)

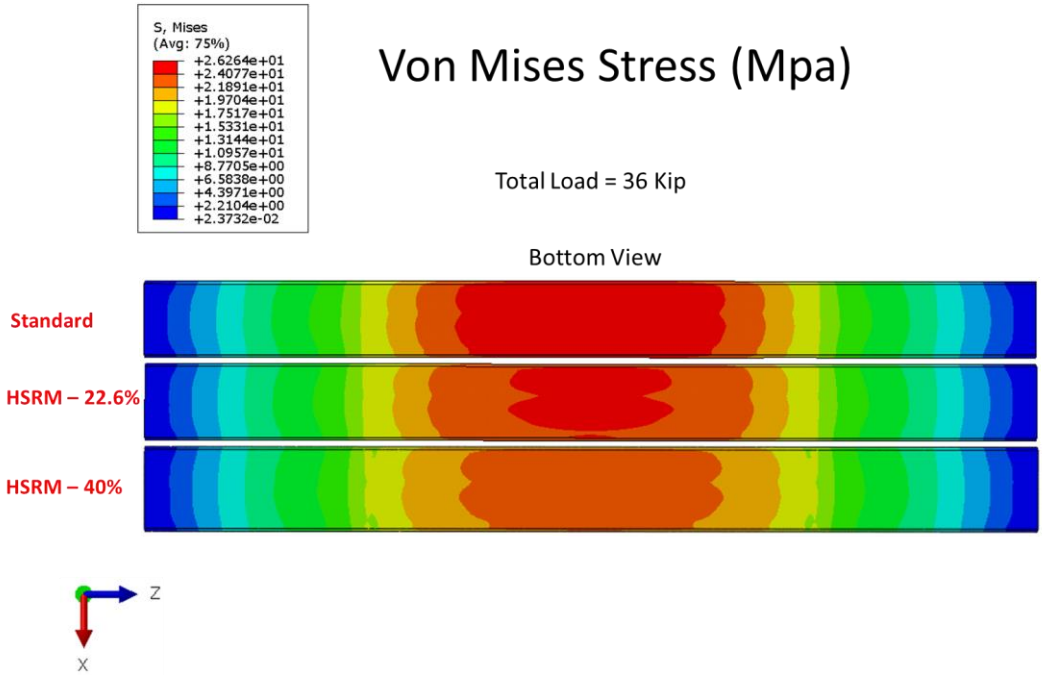

Figure 6.84: Von Mises stress map with a bottom view for each concrete tie. Support type: Center binding support, Load case: L/V = 0. (Stresses are an outcome of 36 Kips of total load applied at the rail seats)

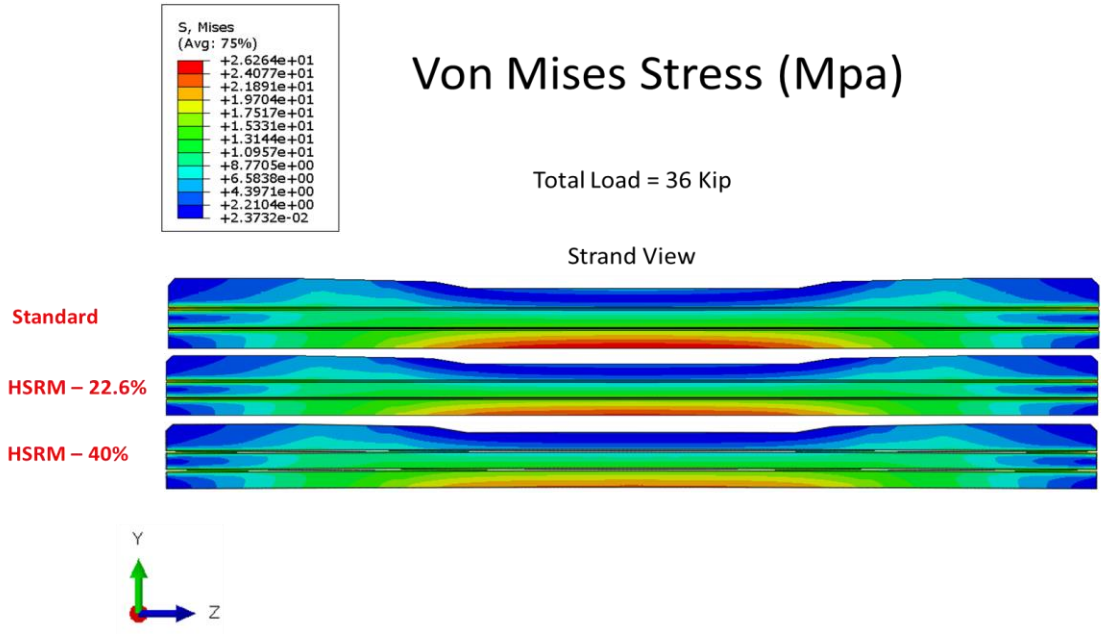

Figure 6.85: Von Mises stress map inside the tie, at the inside strand, for each concrete tie. Support type: Center binding support, Load case: L/V = 0. (Stresses are an outcome of 36 Kips of total load applied at the rail seats)

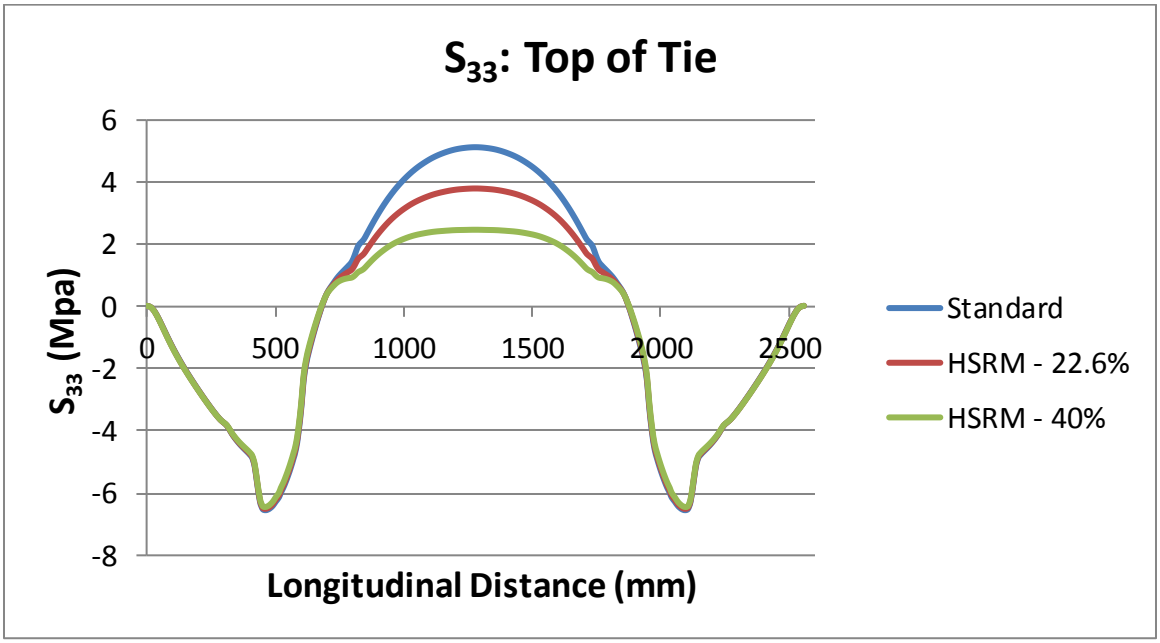

Figure 6.86: Plot of the longitudinal stress along the top fibers of each concrete tie. Support type: Center binding support, Load case: L/V = 0. (Stresses are an outcome of 36 Kips of total load applied at the rail seats)

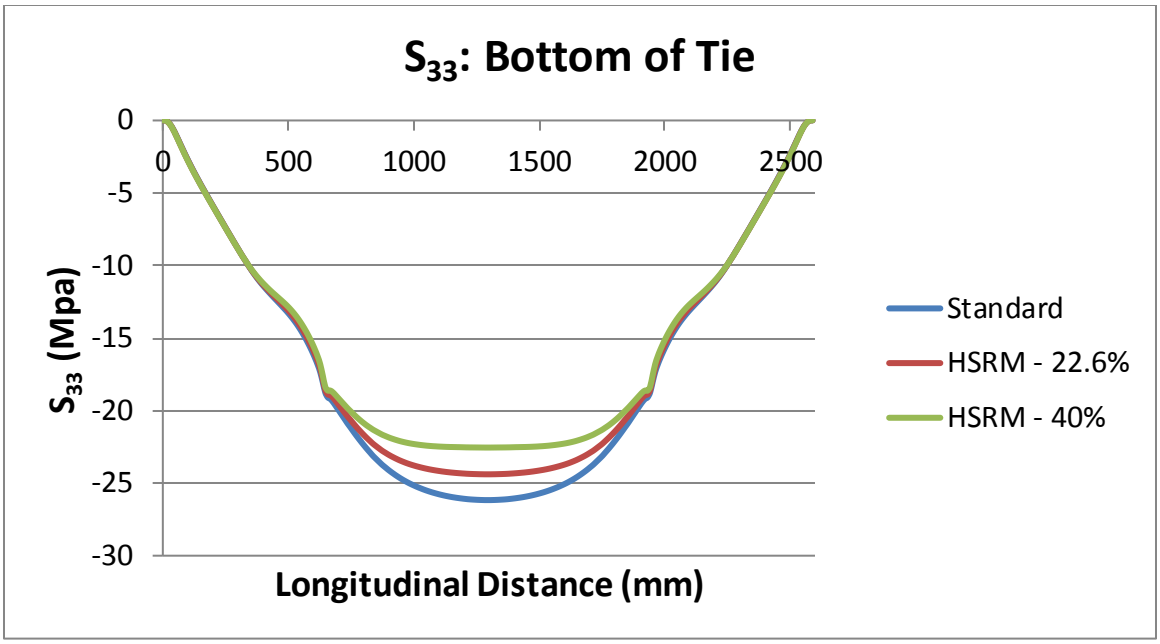

Figure 6.87: Plot of the longitudinal stress along the bottom fibers of each concrete tie. Support type: Center binding support, Load case: L/V = 0. (Stresses are an outcome of 36 Kips of total load applied at the rail seats)

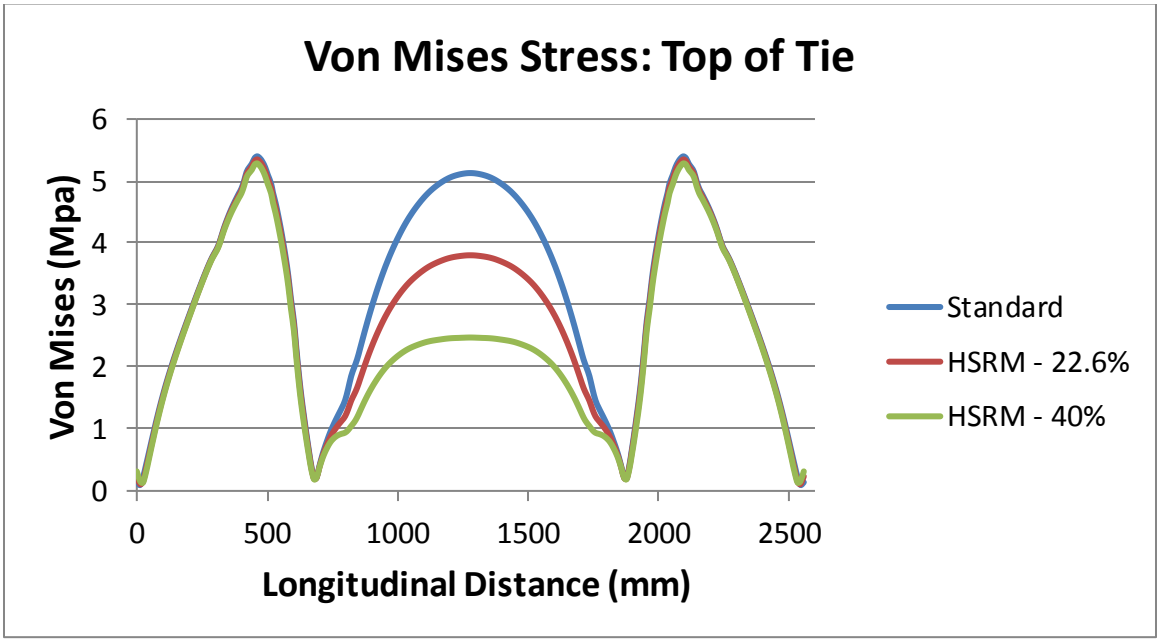

Figure 6.88: Plot of von Mises stress along the top fibers of each concrete tie. Support type: Center binding support, Load case: L/V = 0. (Stresses are an outcome of 36 Kips of total load applied at the rail seats)

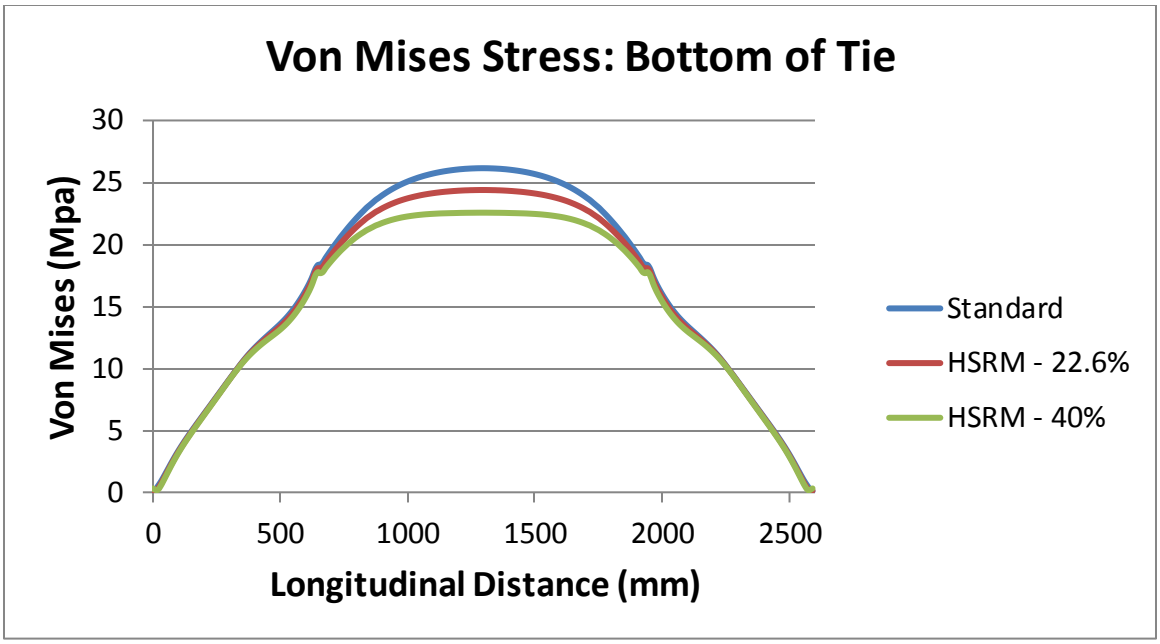

Figure 6.89: Plot of von Mises stress along the bottom fibers of each concrete tie. Support type: Center binding support, Load Case: L/V = 0. (Stresses are an outcome of 36 Kips of total load applied at the rail seats)

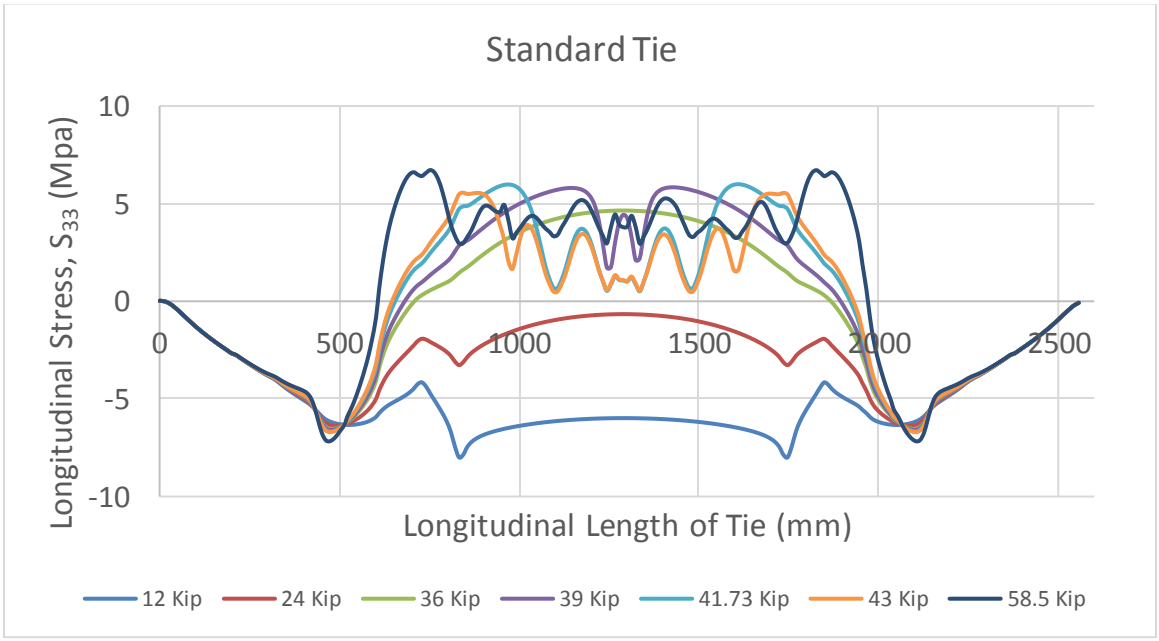

Figure 6.90: Longitudinal stress distribution at various loads for the standard concrete tie. Support type: Center binding support, Load Case: L/V = 0

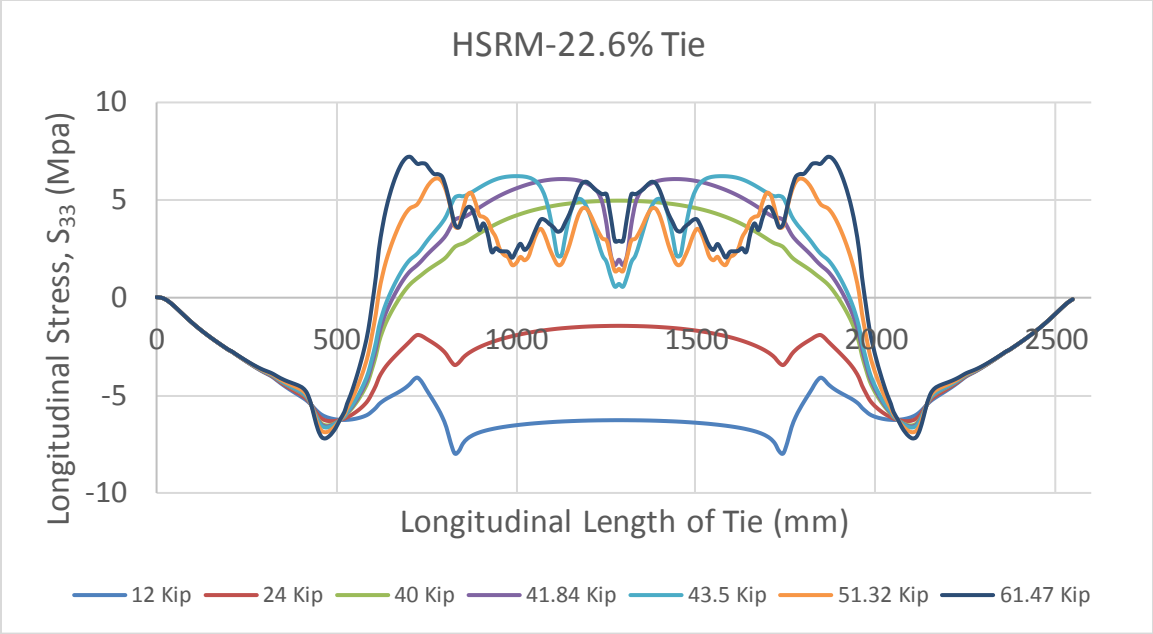

Figure 6.91: Longitudinal stress distribution at various loads for the HSRM-22.6% concrete tie. Support type: Center binding support, Load Case: L/V = 0

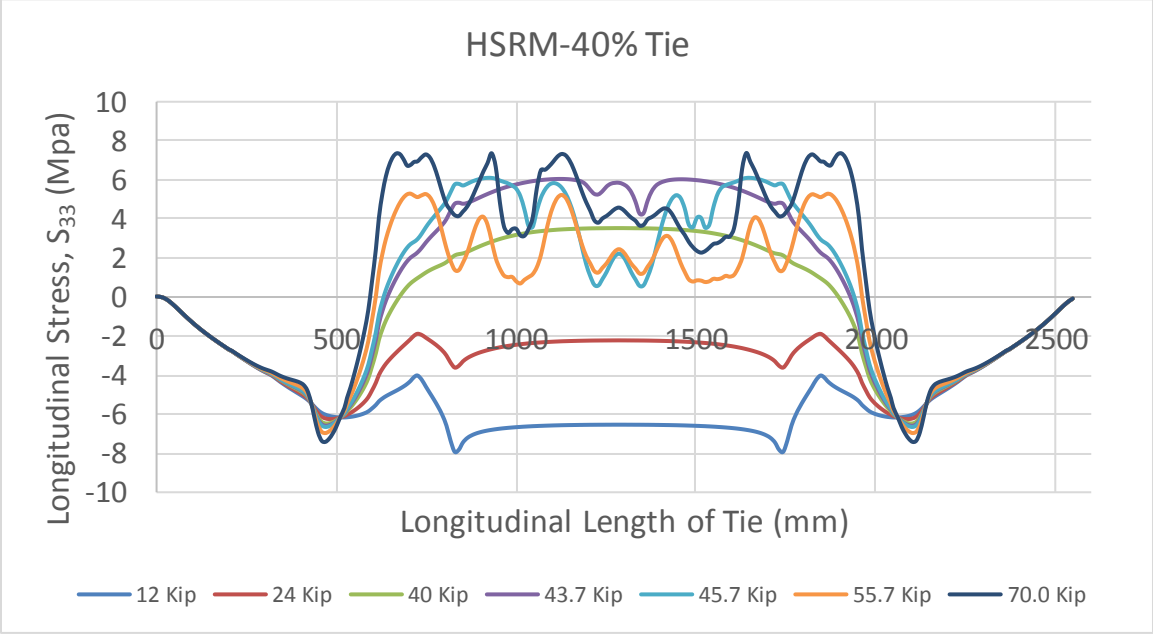

Figure 6.92: Longitudinal stress distribution at various loads for the HSRM-40% concrete tie. Support type: Center binding support, Load Case: L/V = 0

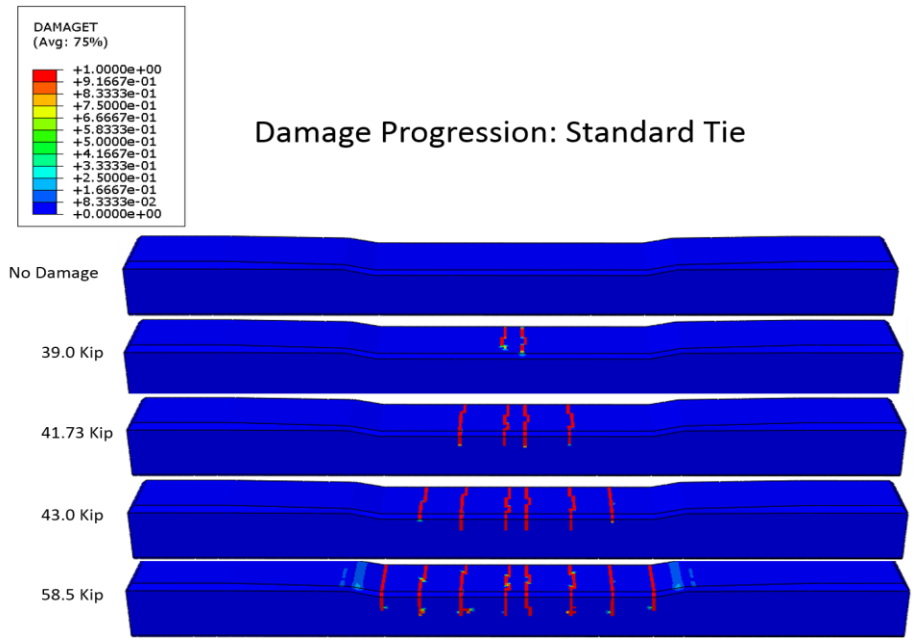

Figure 6.93: Damage progression at various loads for the standard concrete tie. Support type: Center binding support, Load Case: L/V = 0

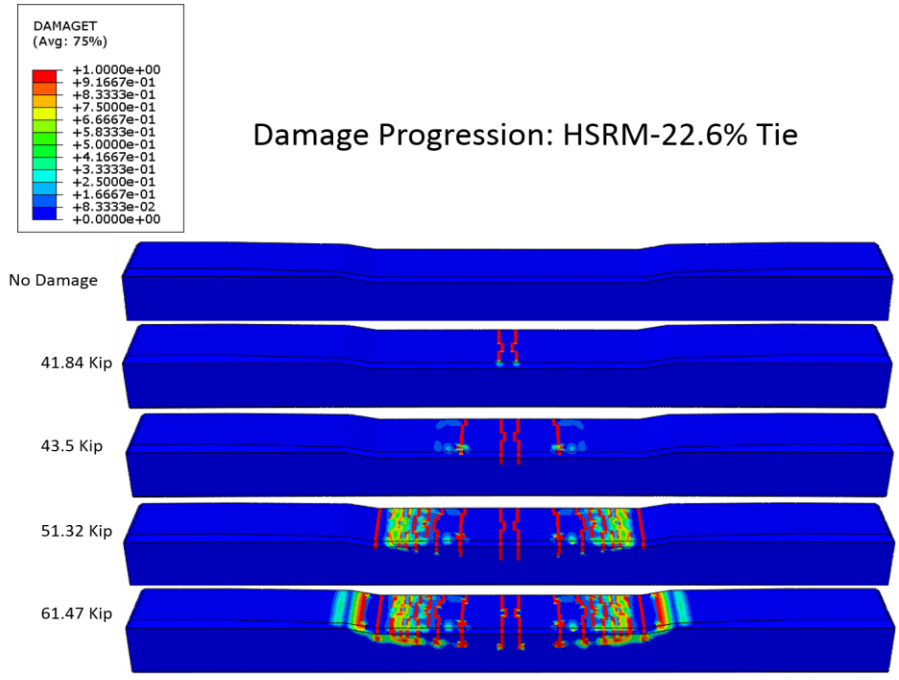

Figure 6.94: Damage progression at various loads for the HSRM-22.6% concrete tie. Support type: Center binding support, Load Case: L/V = 0

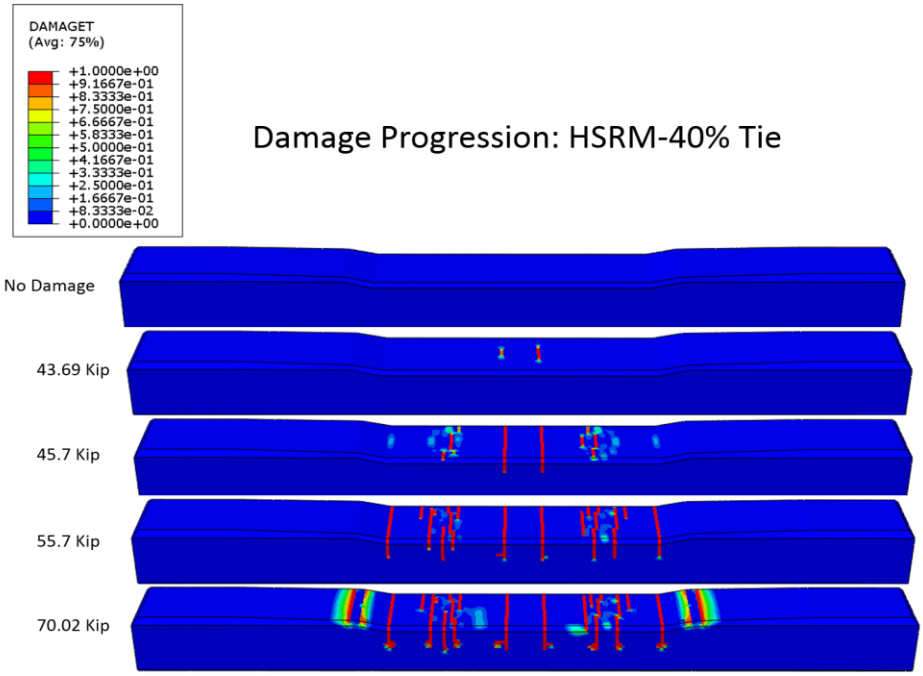

Figure 6.95: Damage progression at various loads for the HSRM-40% concrete tie. Support type: Center binding support, Load Case: L/V = 0

Load Case: L/V = .6

A 40 kip, vertically applied load, is distributed over each rail seat area for the L/V = .6 load case, as discussed in the "Loads and Boundary Conditions" section of Chapter 5 (Figure 6.96). However, the analysis step for each of the three tie models aborted due to convergence issues, which is attributed to the onset of cracks and damage in the concrete ties during the loading procedure. Consequently, the deformed shape, longitudinal stress (S_{33}), and von Mises Stresses, throughout the tie are recorded due to two 14 Kip (total of 28 Kip) vertically applied loads and one 8.4 Kip laterally applied load. Results are recorded at this load because no cracking has taken place yet. This gives insight into the behavior of the concrete ties before any damage has initiated. The

deformed shape, longitudinal stress maps, and von Mises stress maps are presented in (Figures 6.97-6.107) by superimposing the stresses onto the tie for visualization. Longitudinal and von Mises stresses at 28 Kips and 8.4 Kips of vertically and laterally applied loads are recorded along the top and bottom fibers of the concrete and graphed in Figures (6.108-6.111). Furthermore, longitudinal stresses along the top fibers of the concrete tie are recorded and graphed for a series of different loads to demonstrate the behavior of the tie before cracking has taken place and the redistribution of stresses after cracking (Figures (6.112-6.114)). Finally, the progression of tensile damage in the concrete is documented and presented in Figures (6.115-6.117).

The deformed shape of the tie depicts a negative bending moment, similar to that observed in the L/V = 0 load case, causing the top fibers to be inclined to a tensile behavior and the bottom fibers to be inclined to a compressive behavior. The maximum tensile stress in the top fibers of each tie are approximately located 42 in. (1,066.7 mm) from the tie end that contains the lateral load. The maximum compressive stress in the bottom fibers of each tie are approximately located 43.8 in. (1,112.4 mm) from the tie end that contains the lateral load. With regards to the three concrete tie models, it is apparent that the concrete tie that has a lower magnitude of tensile stress in its top fibers and lower magnitude of compressive stresses in its bottom fibers, under the same load, is preferred.

The longitudinal stress (S_{33}) measured at the top fibers (42 inches from the tie end containing the lateral load) of the standard, HSRM-22.6%, and HSRM-40% concrete

tie, due to two 14 Kip (total of 28 Kip) vertically applied loads and one 8.4 Kip laterally applied load, is 713.4 psi (4.92 Mpa), 609.3 psi (4.20 Mpa), and 497.2 (3.43 Mpa). The longitudinal stress (S_{33}) measured at the bottom fibers (43.8 inches from the tie end containing the lateral load) of the standard, HSRM-22.6%, and HSRM-40% concrete tie, due to two 14 Kip (total of 28 Kip) vertically applied loads and one 8.4 Kip laterally applied load, is -3,753.9 psi (-25.88 Mpa), -3,599.0 psi (-24.81 Mpa), and -3,423.0 psi (-23.60 Mpa). The von Mises Stress measured at the top fibers of the standard, HSRM-22.6%, and HSRM-40% concrete tie is 711.3 psi (4.90 Mpa), 607.3 psi (4.19 Mpa), and 495.4 psi (3.42 Mpa). The von Mises Stress measured at the bottom middle fibers of the standard, HSRM-22.6%, and HSRM-40% concrete tie is 3,742.8 psi (25.81 Mpa), 3,590.4 psi (24.76 Mpa), and 3,417.1 psi (23.56 Mpa). Both the HSRM-22.6% and HSRM-40% concrete tie appear to outperform the standard tie, with the HSRM-40% showing the most desirable response of better distributing the stresses throughout the tie. For the HSRM-22.6% concrete tie, a 14.6% decrease in the tensile stresses and a 4.13% decrease in the compressive stresses are observed at the previously described top and bottom fibers of the concrete tie, when compared to the standard tie. For the HSRM-40% concrete tie, a 30.33% decrease in the tensile stresses and an 8.81% decrease in the compressive stresses are observed at the previously described top and bottom fibers of the concrete tie, when compared to the standard tie. Due to the higher tensile stresses observed in the standard concrete tie, as a result from the two 14 Kip and one 8.4 Kip vertically and horizontally applied loads, one would expect cracks to initiate in the standard tie at a lower load than the two HSRM ties. Such was the case observed.

Tensile damage is observed in each of the three concrete tie simulations. The first crack is initiated in the standard concrete tie at a total vertical and horizontal load of 30.96 Kips and 9.29 Kips. The first crack is initiated in the HSRM-22.6% concrete tie at a total vertical and horizontal load of 32.32 Kips and 9.7 Kips. The first crack is initiated in the HSRM-40% concrete tie at a total vertical and horizontal load of 33.73 Kips and 10.12 Kips. Ensuing loading at each rail seat generates additional cracks, resulting in a redistribution of stresses throughout the tie. The damage evolution for the standard, HSRM-22.6%, and HSRM-40% tie is shown in Figures (6.115-6.117). The standard tie endured a vertical and horizontal load of approximately 46.05 Kips and 13.82 Kips before the simulation aborted due to convergence difficulties. The HSRM-22.6% tie endured a vertical and horizontal load of approximately 48.98 Kips and 14.69 Kips before the simulation aborted due to convergence difficulties. Finally, the HSRM-40% tie endured a vertical and horizontal load of approximately 51.80 Kips and 15.54 Kips before the simulation aborted due to convergence difficulties. The redistribution of stresses throughout the load history can be visualized in Figures (6.112-6.114). It should be noted that legend refers to the total vertically applied load at any time for simplicity. If the horizontal load is desired, one simply must divide the vertical load in half and substitute the value for "V" into the L/V = .6 equation. For the standard tie, the 8 Kip and 16 Kip load response show the linear behavior of the tie. The 28 Kip load response shows the response before the first crack has been initiated (30.96 kips). The 31.3 Kip, 35.83 Kip, 41 Kip, and 46.05 Kip load responses depict the redistribution of stresses in the top fibers of the concrete tie due to the formation of cracks. For the HSRM-22.6%

tie, the 8 Kip and 16 Kip load response show the linear behavior of the tie. The 28 Kip load response shows the response before the first crack has been initiated (32.32 kips). The 32.32 Kip, 35.48 Kip, 45.0 Kip, and 48.98 Kip load responses depict the redistribution of stresses in the top fibers of the concrete tie due to the formation of cracks. For the HSRM-40% tie, the 8 Kip and 16 Kip load response show the linear behavior of the tie. The 28 Kip load response shows the response before the first crack has been initiated (33.73 kips). The 33.73 Kip, 37.0 Kip, 44.86 Kip, and 51.8 Kip load responses depict the redistribution of stresses in the top fibers of the concrete tie due to the formation of cracks.

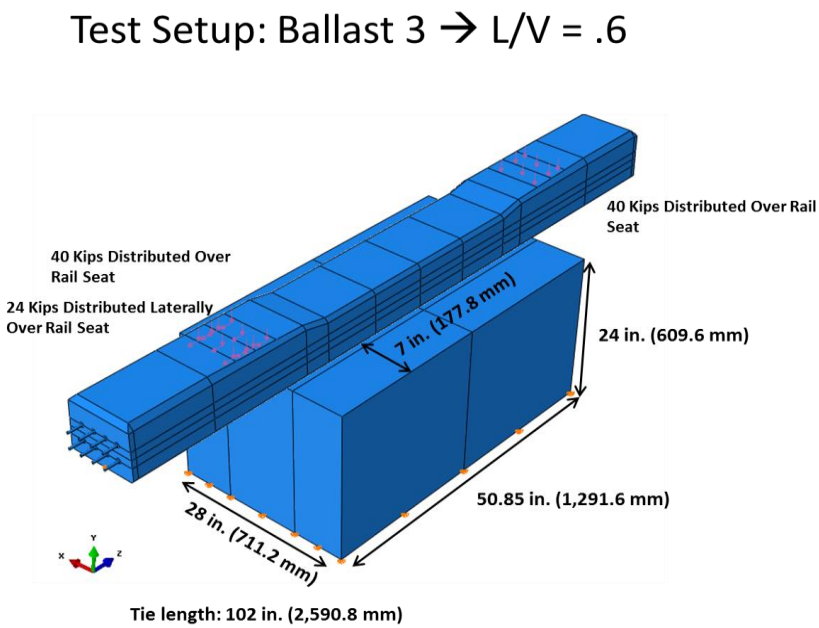

Figure 6.96: Test setup for the center binding supported tie with the load case of L/V = .6

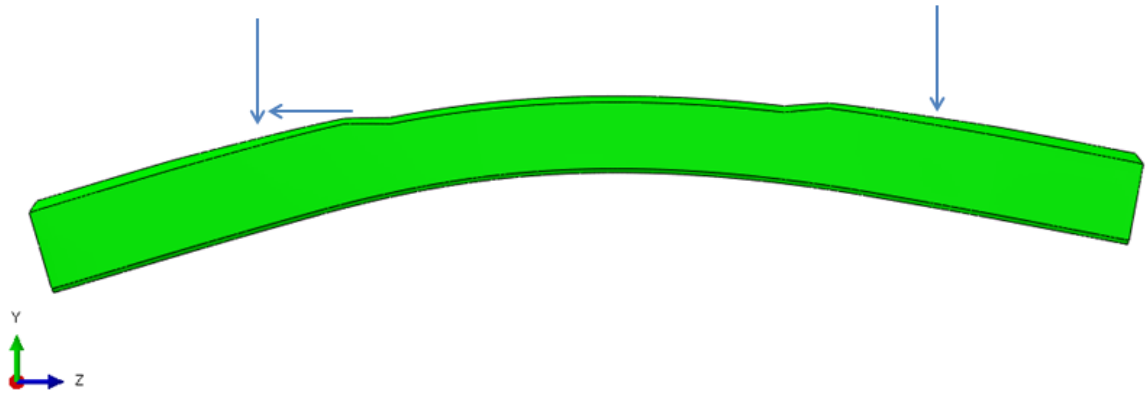

Figure 6.97: Deformed shape of the concrete tie for the center binding supported tie with the L/V = .6 load case

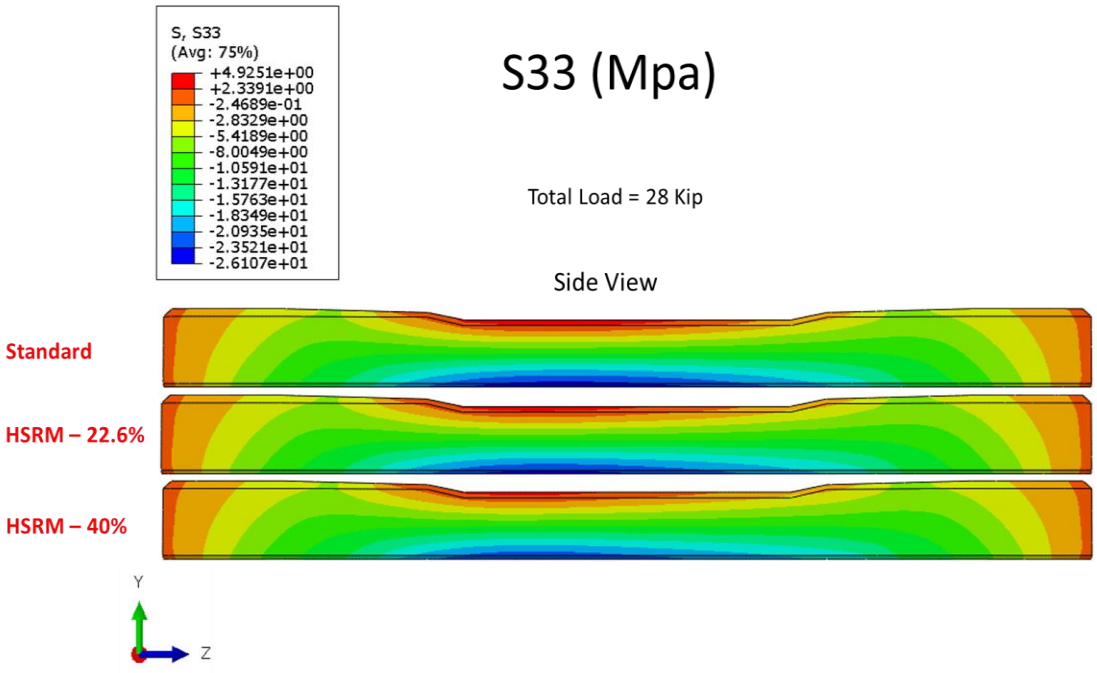

Figure 6.98: Longitudinal stress map with a side view for each concrete tie. Support type: Center binding support, Load case: L/V = .6 (Stresses are an outcome of a horizontal 8.4 Kip load applied at the left rail seat and a total 28 Kips of vertically applied load at the rail seats)

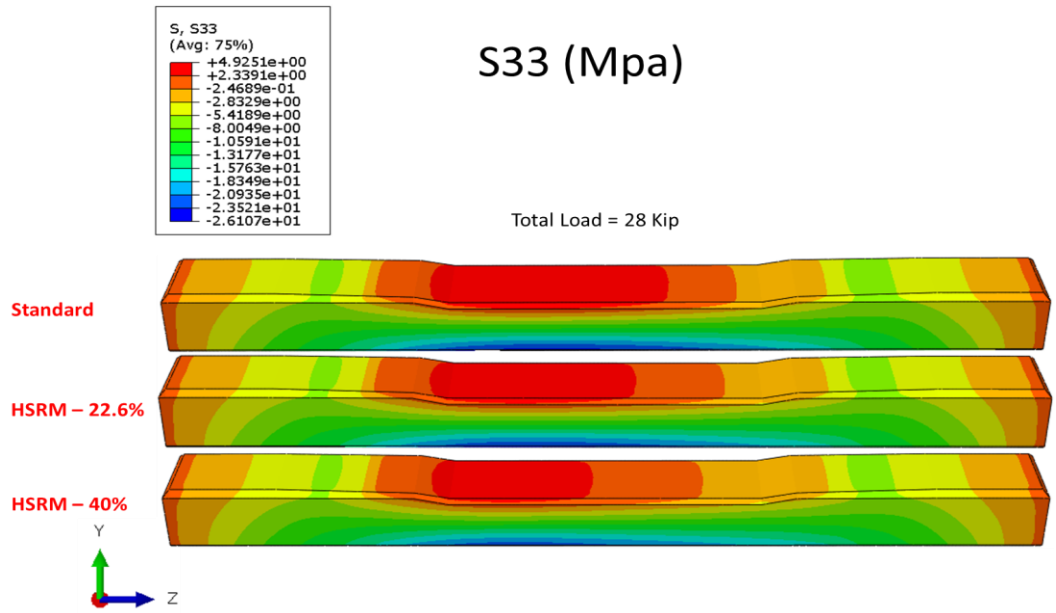

Figure 6.99: Longitudinal stress map with a rotated view for each concrete tie. Support type: Center binding support, Load case: L/V = .6 (Stresses are an outcome of a horizontal 8.4 Kip load applied at the left rail seat and a total 28 Kips of vertically applied load at the rail seats)

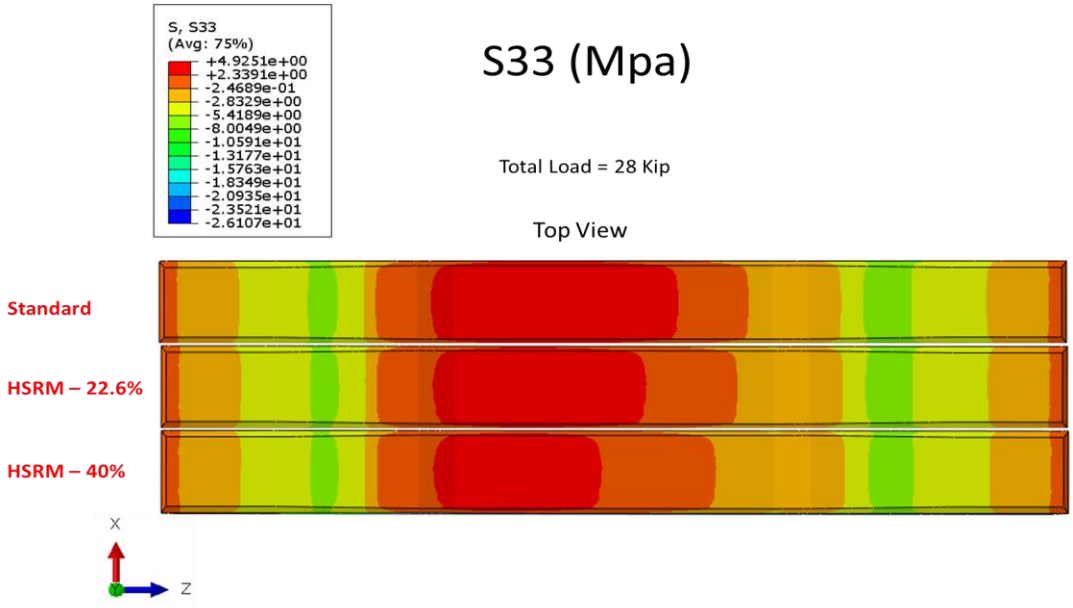

Figure 6.100: Longitudinal stress map with a top view for each concrete tie. Support type: Center binding support, Load case: L/V = .6 (Stresses are an outcome of a horizontal 8.4 Kip load applied at the left rail seat and a total 28 Kips of vertically applied load at the rail seats)

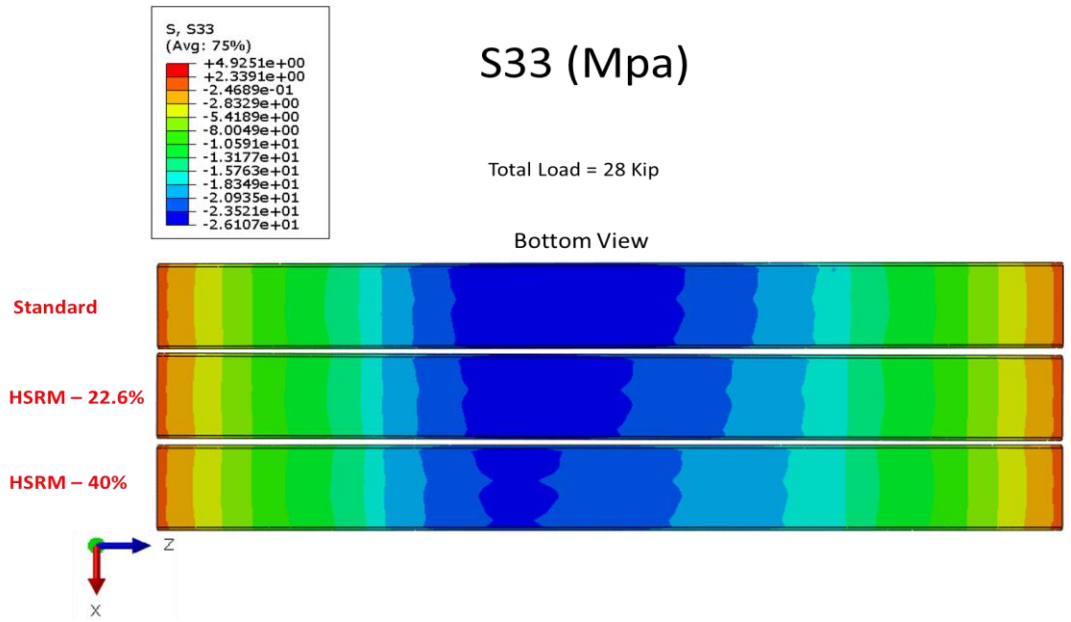

Figure 6.101: Longitudinal stress map with a bottom view for each concrete tie. Support type: Center binding support, Load case: L/V = .6 (Stresses are an outcome of a horizontal 8.4 Kip load applied at the left rail seat and a total 28 Kips of vertically applied load at the rail seats)

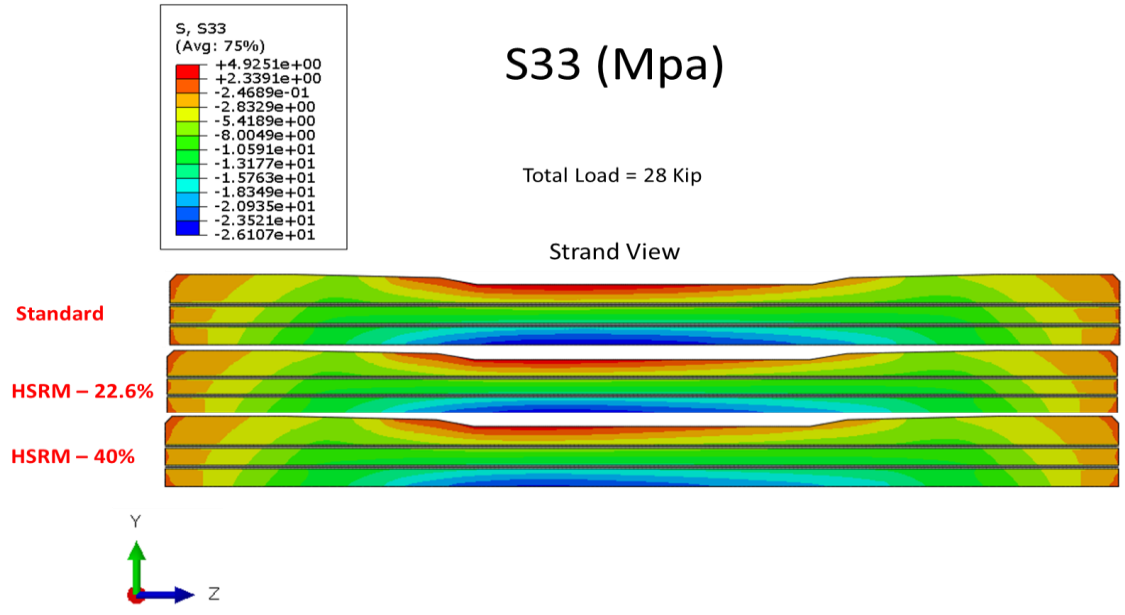

Figure 6.102: Longitudinal stress map inside the tie, at the inside strand, for each concrete tie. Support type: Center binding support, Load case: L/V = .6 (Stresses are an outcome of a horizontal 8.4 Kip load applied at the left rail seat and a total 28 Kips of vertically applied load at the rail seats)

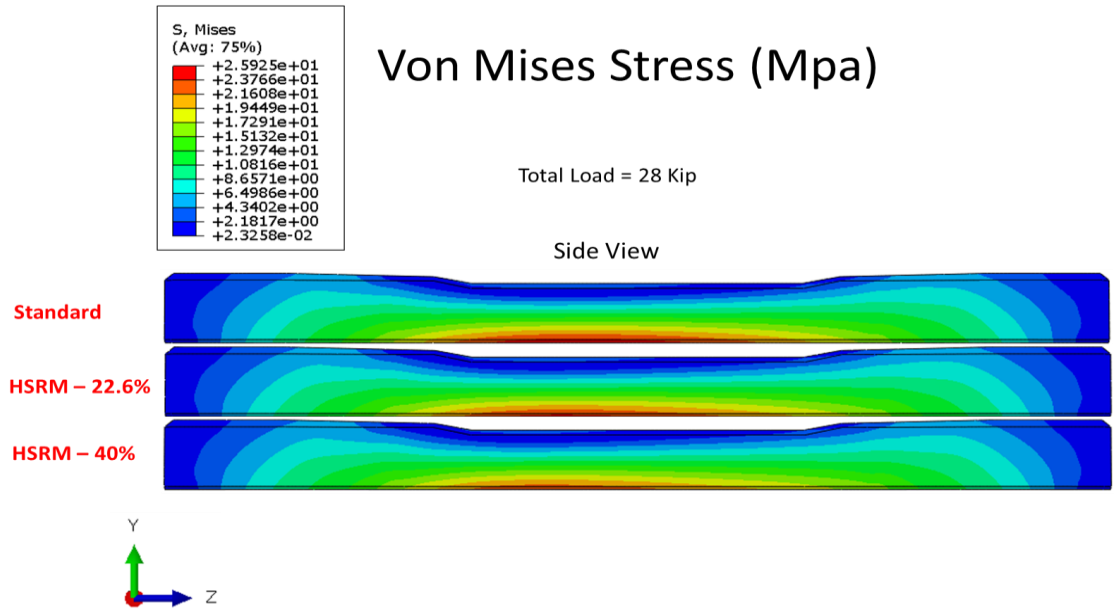

Figure 6.103: Von Mises stress map with a side view for each concrete tie. Support type: Center binding support, Load case: L/V = .6 (Stresses are an outcome of a horizontal 8.4 Kip load applied at the left rail seat and a total 28 Kips of vertically applied load at the rail seats)

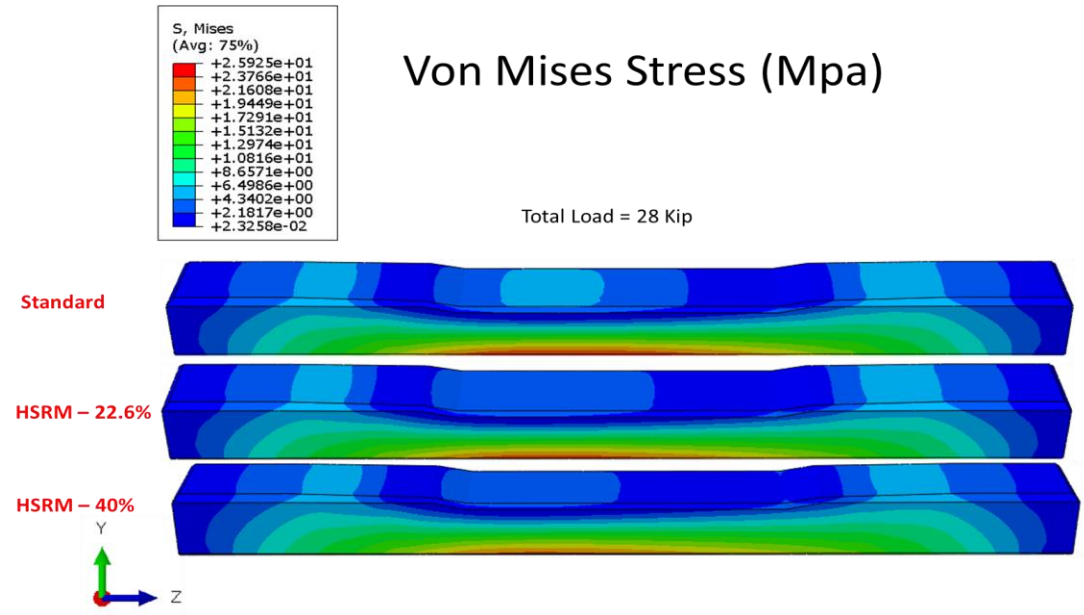

Figure 6.104: Von Mises stress map with a rotated view for each concrete tie. Support type: Center binding support, Load case: L/V = .6 (Stresses are an outcome of a horizontal 8.4 Kip load applied at the left rail seat and a total 28 Kips of vertically applied load at the rail seats)

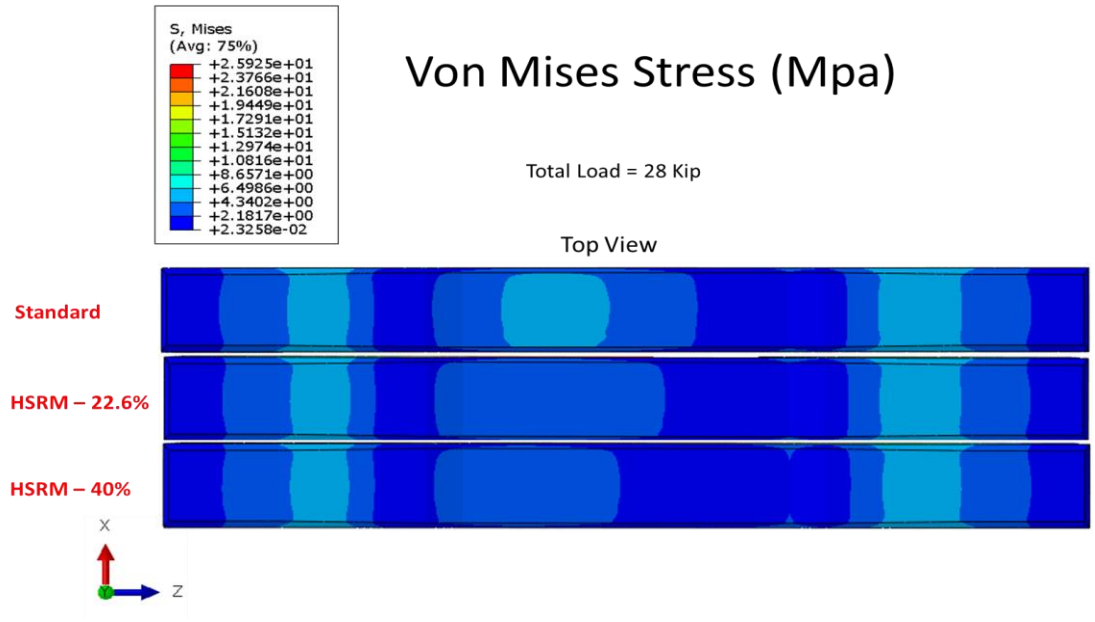

Figure 6.105: Von Mises stress map with a top view for each concrete tie. Support type: Center binding support, Load case: L/V = .6 (Stresses are an outcome of a horizontal 8.4 Kip load applied at the left rail seat and a total 28 Kips of vertically applied load at the rail seats)

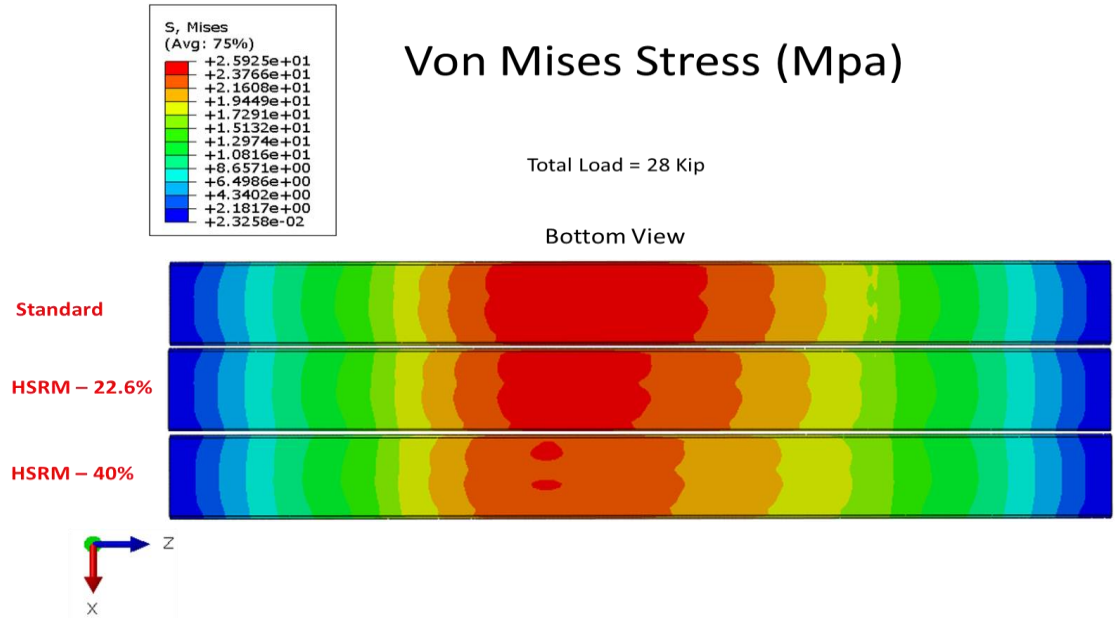

Figure 6.106: Von Mises stress map with a bottom view for each concrete tie. Support type: Center binding support, Load case: L/V = .6 (Stresses are an outcome of a horizontal 8.4 Kip load applied at the left rail seat and a total 28 Kips of vertically applied load at the rail seats)

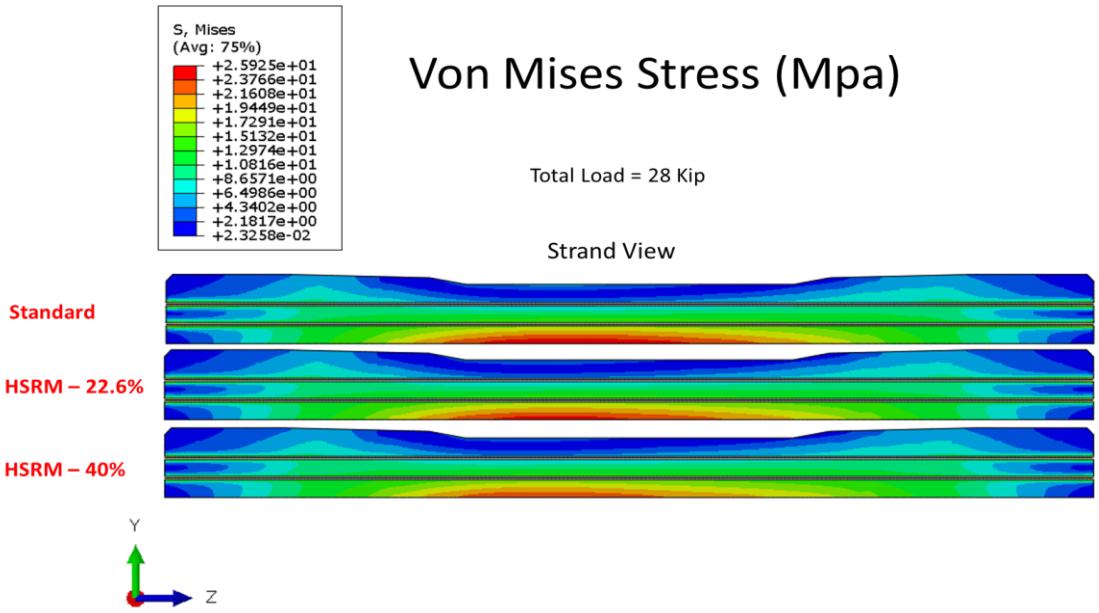

Figure 6.107: Von Mises stress map inside the tie, at the inside strand, for each concrete tie. Support type: Center binding support, Load case: L/V = .6 (Stresses are an outcome of a horizontal 8.4 Kip load applied at the left rail seat and a total 28 Kips of vertically applied load at the rail seats)

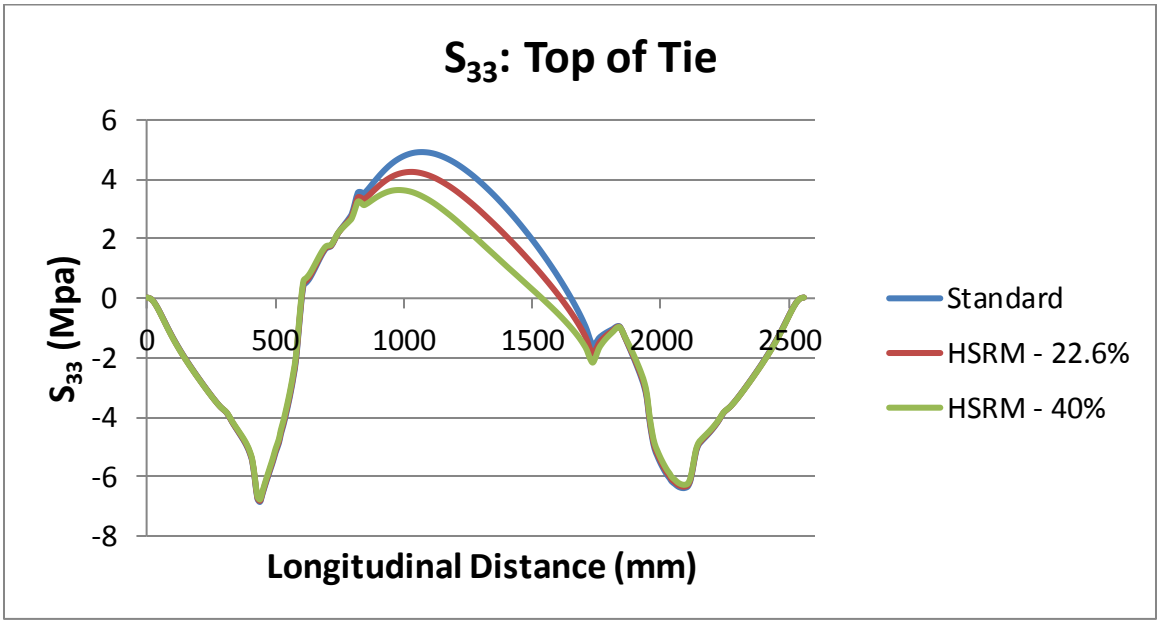

Figure 6.108: Plot of the longitudinal stress along the top fibers of each concrete tie. Support type: Center binding support, Load case: L/V = .6 (Stresses are an outcome of a horizontal 8.4 Kip load applied at the left rail seat and a total 28 Kips of vertically applied load at the rail seats)

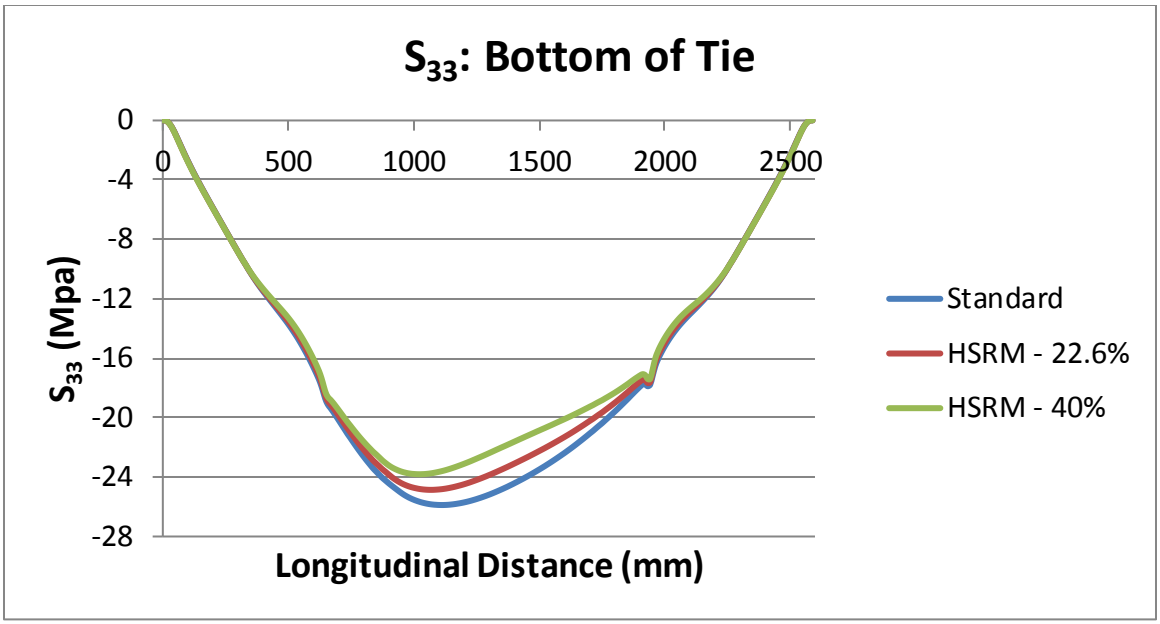

Figure 6.109: Plot of the longitudinal stress along the bottom fibers of each concrete tie. Support type: Center binding support, Load case: L/V = .6 (Stresses are an outcome of a horizontal 8.4 Kip load applied at the left rail seat and a total 28 Kips of vertically applied load at the rail seats)

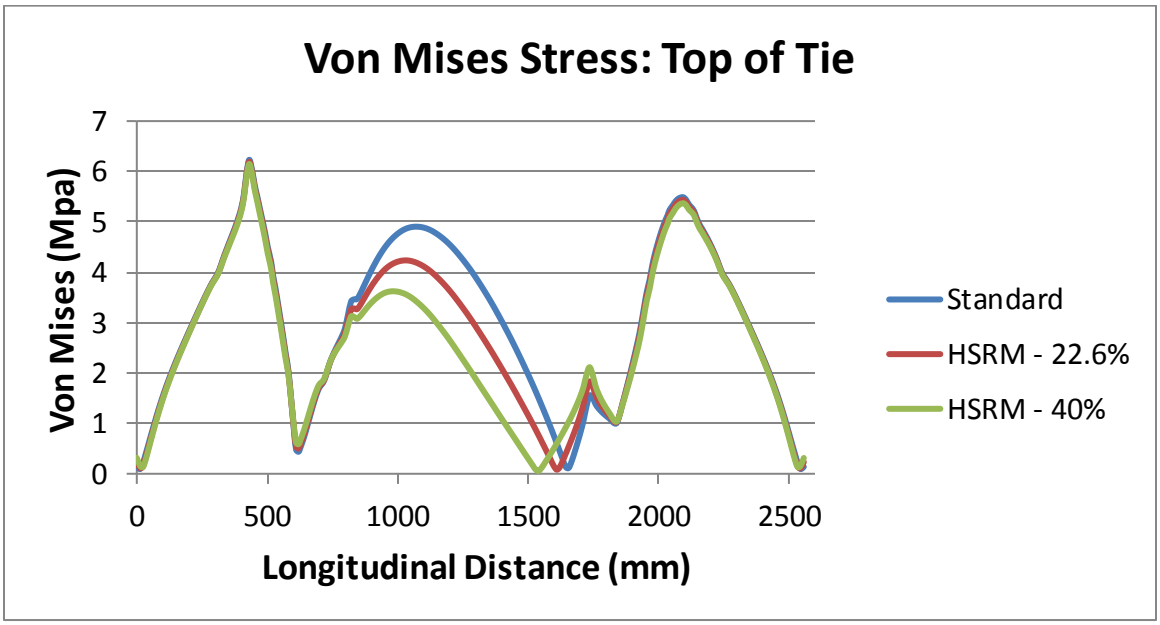

Figure 6.110: Plot of von Mises stress along the top fibers of each concrete tie. Support type: Center binding support, Load case: L/V = .6 (Stresses are an outcome of a horizontal 8.4 Kip load applied at the left rail seat and a total 28 Kips of vertically applied load at the rail seats)

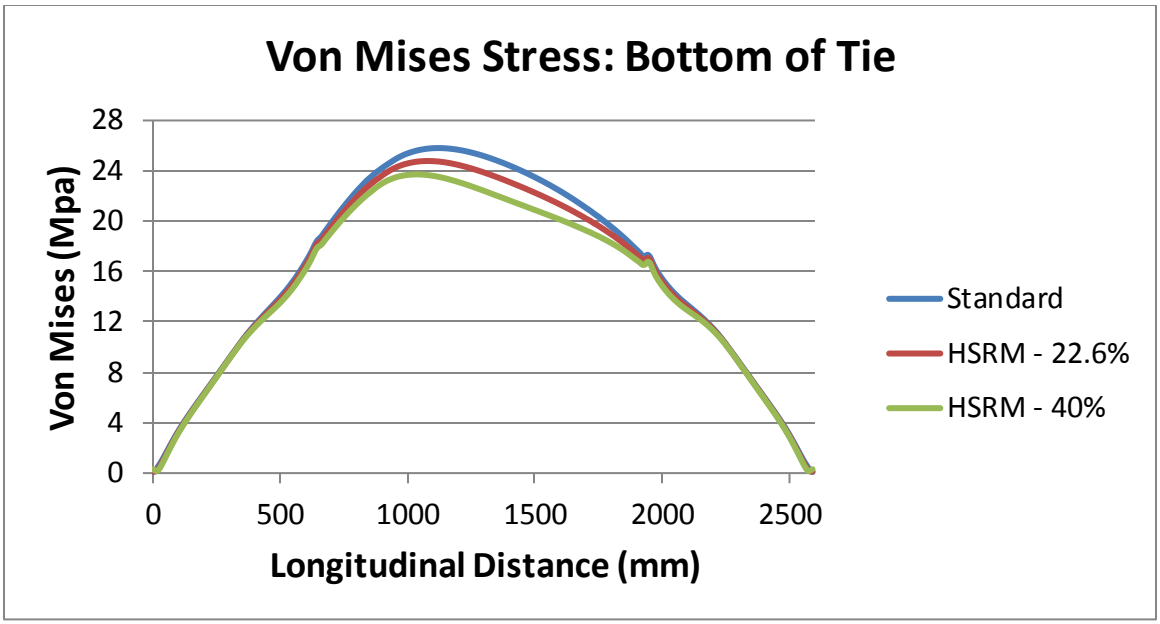

Figure 6.111: Plot of von Mises stress along the bottom fibers of each concrete tie. Support type: Center binding support, Load Case: L/V = .6 (Stresses are an outcome of a horizontal 8.4 Kip load applied at the left rail seat and a total 28 Kips of vertically applied load at the rail seats)

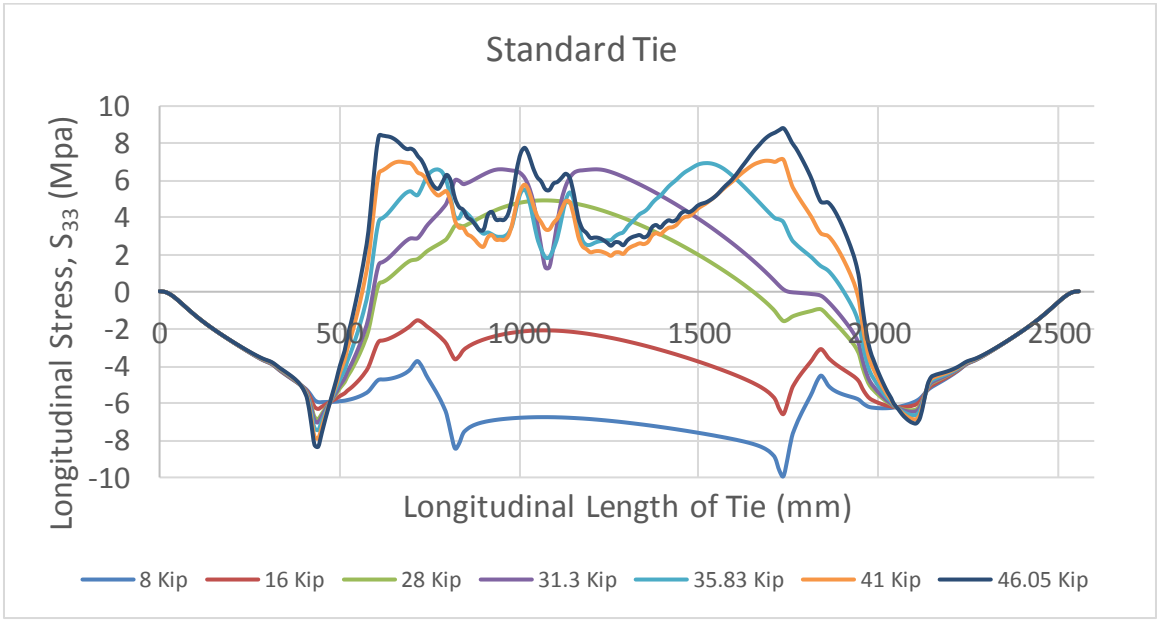

Figure 6.112: Longitudinal stress distribution at various loads for the standard concrete tie. Support type: Center binding support, Load Case: L/V = .6

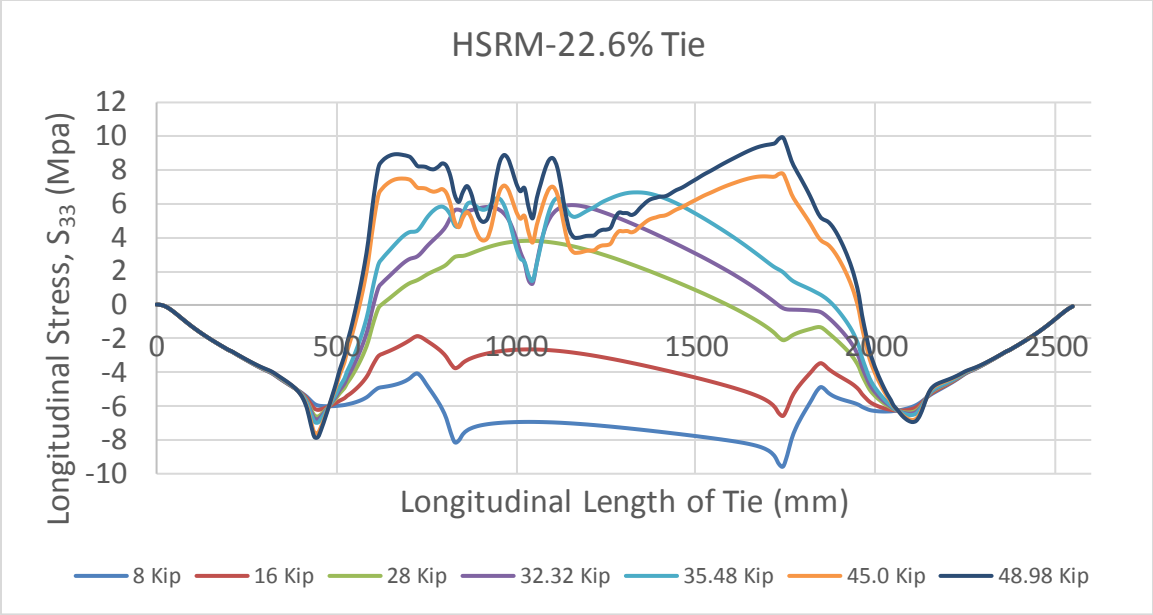

Figure 6.113: Longitudinal stress distribution at various loads for the HSRM-22.6% concrete tie. Support type: Center binding support, Load Case: L/V = .6

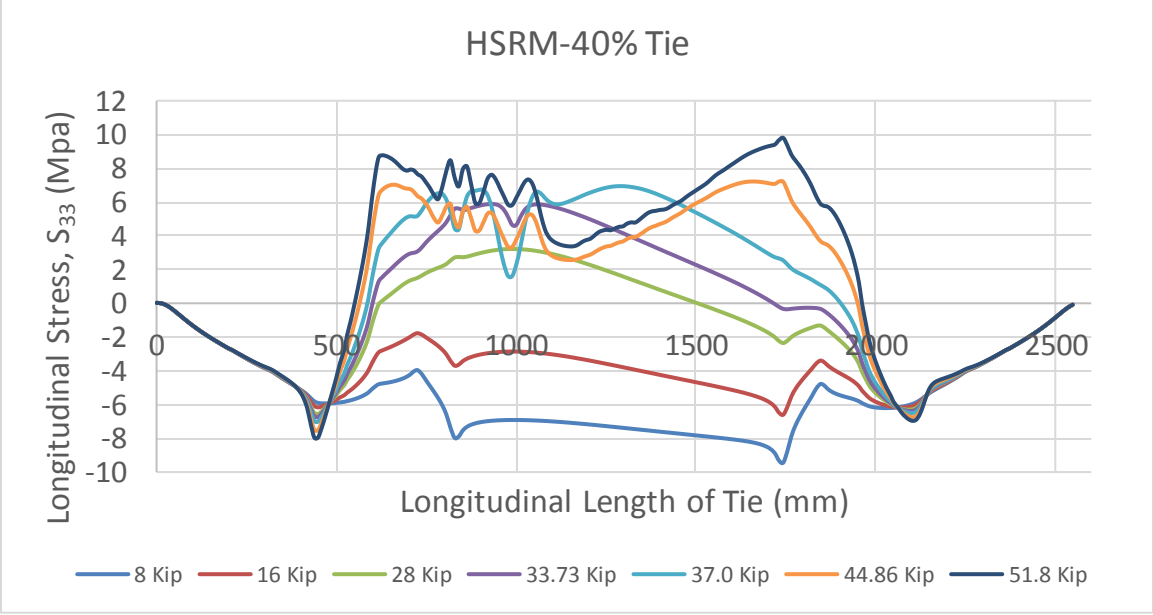

Figure 6.114: Longitudinal stress distribution at various loads for the HSRM-40% concrete tie. Support type: Center binding support, Load Case: L/V = .6

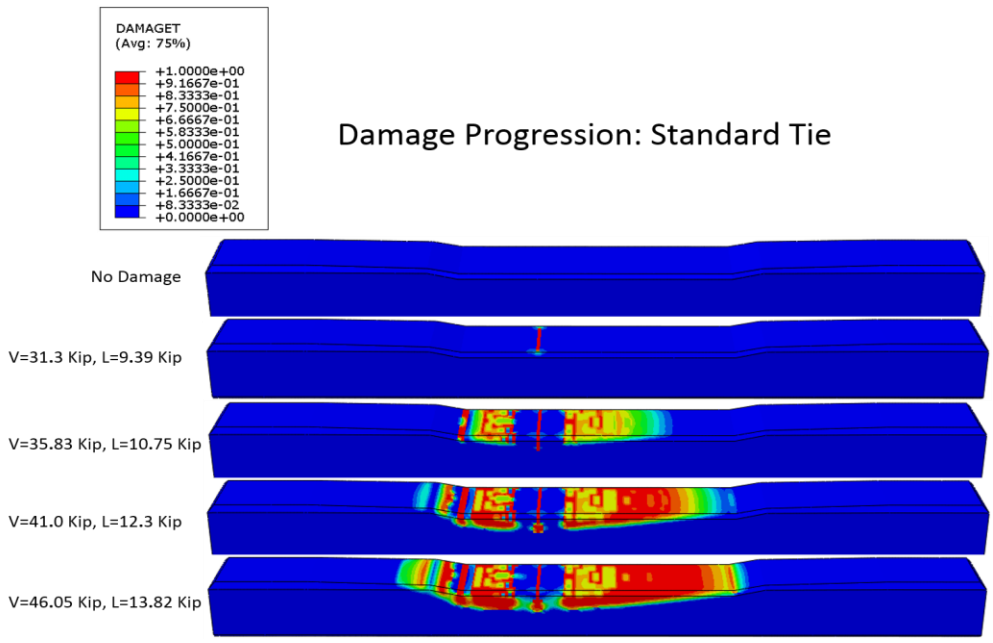

Figure 6.115: Damage progression at various loads for the standard concrete tie. Support type: Center binding support, Load Case: L/V = .6

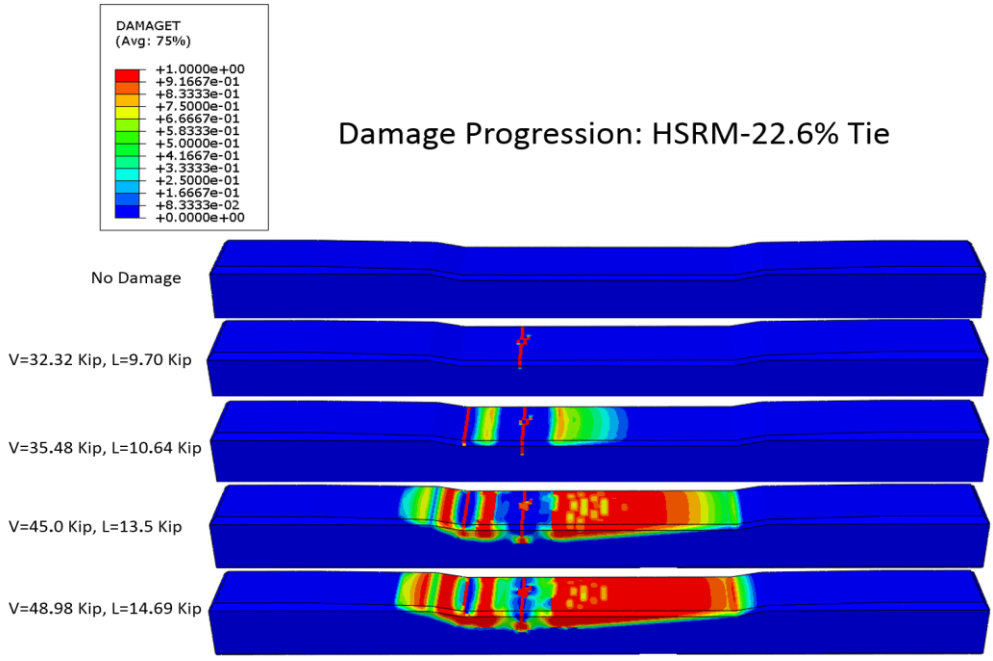

Figure 6.116: Damage progression at various loads for the HSRM-22.6% concrete tie. Support type: Center binding support, Load Case: L/V = .6

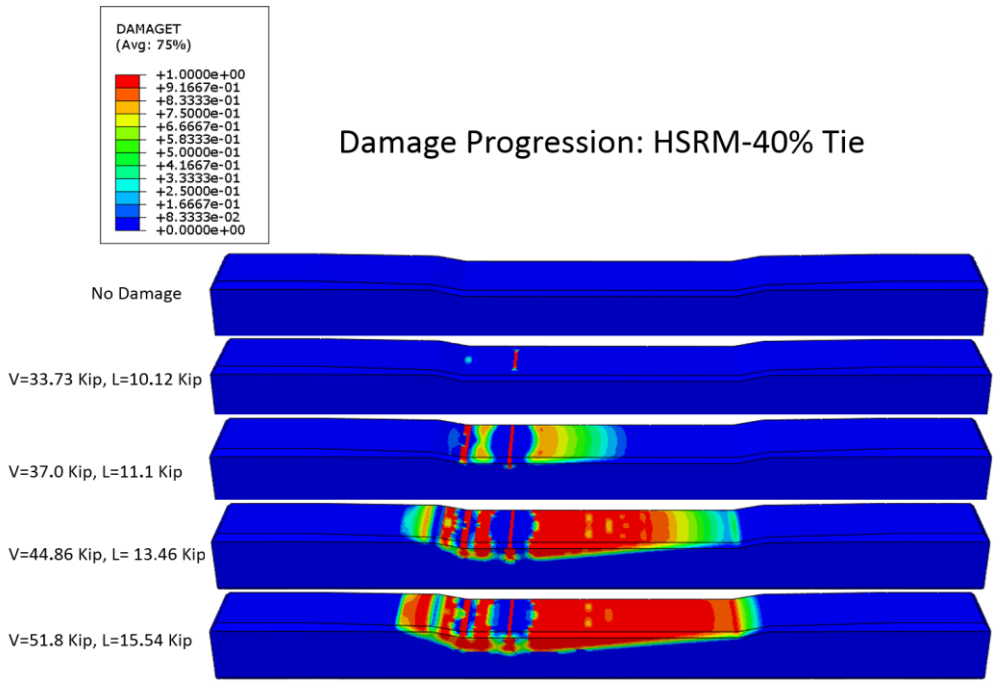

Figure 6.117: Damage progression at various loads for the HSRM-40% concrete tie. Support type: Center binding support, Load Case: L/V = .6

Critical Discussion of HSRM Tie Performance

The concrete tie is divided into three distinct regions to further compare the performance of each concrete tie. The three regions are defined as "End A", "End B", and the "Center" region. Within each region, locations of concern, such as sites where large stress amplitudes are observed or sites that are most prone to develop cracks under increasing loads, are recorded along the top and bottom surfaces of the concrete tie and summarized in Table (6.2). The center region represents the middle section where a constant cross-section is maintained or the middle 36 in. (914.4 mm) of the tie. End "A" depicts the region facing the field side, which contains the rail seat with the combination of vertical and lateral loads (if applicable). This region is 33 in. (838.2 mm)

long and begins at the tie end and terminates where the center region begins. In contrast, End "B" represents the remaining 33 in. (838.2 mm) of the tie on the opposite side of the tie where only vertical loads are applied.

The two HSRM concrete ties considered in this study outperformed the standard concrete tie in all the proposed loading and supporting scenarios by better distributing the stresses throughout the tie. This effect is most pronounced in the center binding support case, when the initiation of cracks appears on the HSRM ties at higher loads as compared to the standard concrete ties. The HSRM-22.6% tie experiences its first crack approximately 2.84 Kips and 1.36 Kips after the standard concrete tie has already cracked for the L/V = 0 and L/V = .6 load cases. The HSRM-40% delays the initiation of cracks by undergoing an additional 4.7 Kips and 2.77 Kips for the L/V = 0 and L/V = .6 load case, when compared to the standard tie. The finite element simulations show that reducing the elastic modulus of the standard concrete by 40% can allow as high as 4.7 Kips of additional load before the first crack is initiated. The positive behavior of the concrete ties is not just noticed in the nonlinear regions of the tie, but also in the linear regions.

In the continuously supported and end supported simulations, the concrete ties remained in the linear region and no plastic strains were developed. Even in the linear region it is obvious that the two HSRM material models show favorable responses when compared to the standard tie. For the continuously supported tie, it is preferred for the concrete tie to have lower tensile and compressive stress in its middle top and bottom

fibers. Both HSRM concrete ties exhibited this desired behavior. As compared to the standard tie, the HSRM-22.6% shows as high as an 11% increase in the compressive stress at the top fibers of the tie which are susceptible to tension cracking with increasing loads and as high as a 4.83% reduction in the compressive stresses in the bottom fibers of the tie which will reach crushing with increasing loads. The HSRM-40% shows as high as an 20.37% increase in the compressive stress at the top fibers of the tie (moving further from a tensile state) and as high as a 9.48% reduction in the compressive stresses in the bottom fibers of the tie, when compared to the standard tie. For the end supported ties, it is preferred for the concrete tie to lower tensile stresses in the bottom fibers of the tie and lower compressive stresses in the top fibers of the tie. Again, both HSRM ties exhibited this desired behavior. The HSRM-22.6% tie shows as high as a 6.67% reduction in the compressive stresses at the top fibers and as high as a 77.8% increase in the compressive stresses at the bottom fibers (moving further from a tensile state), when compared to the standard tie. The HSRM-40% tie shows as high as a 12.95% reduction in the compressive stresses at the top fibers while delaying the development of pure tensile stresses at the bottom fibers of the concrete preventing, thus, cracking when compared to the standard tie.

Table 6.2: Longitudinal Stress recorded at potential locations of concern at the top and bottom fibers of each concrete tie.

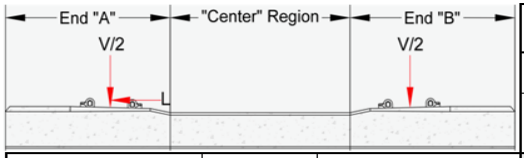

			Longitudinal Stress, S33 (Mpa)					
			Continuous Support		End Supports		Center Binding Support	
			L/V = 0 (V = 80^k)	L/V = 0.6 (V = 80^k)	L/V = 0 (V = 80^k)	L/V = 0.6 (V = 80^k)	L/V = 0 (V = 36^k)	L/V = 0.6 (V = 28^k)
HSRM-22.6%	Top	End A	-18.4	-20.0	-18.7	-18.3	-6.50	-6.82
		Center	-6.07	-4.55	-16.0	-21.5	3.80	4.20
		End B	-18.4	-18.7	-18.7	-19.4	-6.50	-6.33
	Bottom	End A	-5.02	-3.15	-4.35	-13.4	Center Governs	Center Governs
		Center	-15.8	-15.2	-7.73	-3.78	-24.4	-24.8
		End B	-5.02	-1.95	-4.35	-1.36	Center Governs	Center Governs
HSRM-40%	Top	End A	-18.0	-19.8	-17.4	-18.2	-6.44	-6.77
		Center	-6.30	-4.94	-14.9	-20.1	2.47	3.43
		End B	-18.0	-18.3	-17.4	-18.6	-6.44	-6.27
	Bottom	End A	-5.31	-3.21	-4.68	-13.5	Center Governs	Center Governs
		Center	-15.1	-14.4	-8.28	-4.41	-22.5	-23.6
		End B	-5.31	-2.17	-4.68	-1.90	Center Governs	Center Governs
Standard	Top	End A	-18.7	-20.2	-20.0	-18.6	-6.55	-6.85
		Center	-5.79	-4.10	-17.1	-22.9	5.13	4.92
		End B	-18.7	-19.1	-20.0	-20.3	-6.55	-6.38
	Bottom	End A	-4.81	-3.10	-3.92	-13.2	Center Governs	Center Governs
		Center	-16.5	-15.9	-7.02	-3.04	-26.2	-25.9
		End B	-4.81	-1.72	-3.92	-0.763	Center Governs	Center Governs

Chapter 7: Conclusions and Recommendations

Conclusions

This work presents a comparative study on the performance of prestressed HSRM and "standard" concrete ties through finite element model simulations. Three-dimensional nonlinear finite element models are developed to predict the response of HSRM and standard concrete ties to various loading and support conditions. Nonlinear material models for the HSRM and standard concrete are developed, using the concrete damage plasticity model within ABAQUS, to investigate the post-cracking behavior of each tie. A Four Point Flexural Bending Test was experimentally performed in the lab to validate the finite element model for the standard tie. The simulated results for the standard FE model show reasonable agreement with the experimental data. This work proceeded to simulate the performance of both the standard and HSRM tie to various loading and boundary conditions through several different simulations. Based on the results from these simulations, a series of conclusions are made:

1) The finite element model for the standard tie shows good agreement with experimental results and the simulation results are deemed reliable.

2) Post cracking performance of the ties is a good indication of the quality of the tie and length of the service life. Damaged plasticity models meet the need for investigating the post-cracking behavior, provided that the damaged plasticity model parameters are reflective of the physical model parameters and accurately capture the material response.
3) It is demonstrated that by reducing the elastic modulus of the standard concrete, while maintaining its high strength, beneficial effects on the performance of prestressed concrete are realized.
    a) Finite element simulations show that the HSRM concrete tie delays the initiation of tensile cracks when compared to the standard concrete tie.
    b) The HSRM tie appears to better distribute stresses throughout the tie resulting in a lower magnitude of tensile and compressive stress observed at the concrete's top and bottom fibers.
    c) The damage progression of the HSRM concrete tie, specific to the center binding support with L/V = 0 loading case, shows a tie with many short cracks distributed along its surface.
    d) The damage progression of the standard concrete tie, specific to the center binding support with L/V = 0 loading case, shows a tie with less cracks than the HSRM, but the cracks extend further into the tie (the cracks are deeper).
4) The quality of the ballast has a large impact on the performance of the tie. Discontinuities in the support, such as voids beneath the tie resulting from a

shift in aggregate, is very influential on the behavior of the tie. HSRM ties show a better overall performance under different support conditions since the increased flexibility allows the tie to conform better to the uneven ballast support.

5) HSRM concrete may offer itself as a cost effective alternative concrete to the traditional high performance concrete used in prestressed concrete ties with the potential to increase the life of the tie.

Recommendations

Though this study is very insightful into the benefits of using HSRM concrete in manufacturing prestressed concrete rail ties, there's still much work to be done in order fully grasp and further understand the mechanical behavior of HSRM concrete ties. The following recommendations are made for future studies:

1) Develop separate concrete-steel interface models specific to both the HSRM and standard concrete ties.
2) Perform model validations studies specific to the HSRM concrete tie.
3) Further calibrate the material models used in the finite element software with experimental results.
4) Simulate the behavior of HSRM concrete ties to dynamic loading scenarios.
5) Perform parametric studies on additional concrete parameters, such as poisson's ratio.

6) Investigate the need to use more elaborate models to investigate:

   a) The effects of the more flexible tie on the load distribution in the track in the longitudinal direction.

   b) The effects of the nonlinear behavior of the ballast.

   c) The effects of the nonlinear behavior of the steel strands.

   d) Effects of HSRM concrete on the performance of the fastening system.

References

Abdelatif, A.O, J.S Owen, and M.F.M Hussein. 2015. "Modelling the prestress transfer in pre-tensioned concrete elements." *In Finite Elements in Analysis and Design* 94: 47-63.

Abdulqader, A. 2017. "Performance Assessment of HSRM Prestressed Concrete Railroad Ties Through Labratory Testing." Master's Thesis, Department of Civil and Environmental Engineering, University of South Carolina, Columbia, SC.

Abrishami , Homayoun G., and Denis Mitchell. 1993. "Bond Characteristics of Pretensioned Strand." *ACI Materials Journal* 90 (3): 228-235.

Arab, Amir A., Sameh S. Badie, and Majid T. Manzari. 2011. "A methodological approach for finite element modeling of pretensioned concrete members at the release of pretensioning." *Engineering Structures* 33 (6): 1918-1929.

ASTM A886/A886M. 2016. "Standard Specification for Steel Strand, Indented, Seven-Wire Stress-Relieved for Prestressed Concrete." ASTM International, West Conshohocken, PA.

ASTM C127-15. 2015. "Standard Test Method for Relative Density (Specific Gravity) and Absorption of Coarse Aggregate." ASTM International, West Conshohocken, PA.

ASTM C131/C131M-14. 2006. "Standard Test Method for Resistance to Degradation of Small-Size Coarse Aggregate by Abrasion and Impact in the Los Angeles Machine." ASTM International, West Conshohocken, PA.

ASTM C136/C136M-14. 2014. "ASTM C136 / C136M-14, Standard Test Method for Sieve Analysis of Fine and Coarse Aggregates." ASTM International, West Conshohocken, PA.

ASTM C150/150M-17. 2017. "Standard Specification for Portland Cement." ASTM International, West Conshohocken, PA.

ASTM C192/C192M-16a. 2016. "Standard Practice for Making and Curing Concrete Test Specimens in the Laboratory." ASTM International, West Conshohocken, PA.ASTM C29/C29M-17a. 2017. "Standard Test Method for Bulk Density (“Unit Weight”) and Voids in Aggregate." ASTM International, West Conshohocken, PA.

ASTM C39/C39M-17b. 2017. "Standard Test Method for Compressive Strength of Cylindrical Concrete Specimens." ASTM International, West Conshohocken, PA.

ASTM D3148-02. 2002. "Standard Test Method for Elastic Moduli of Intact Rock Core Specimens in Uniaxial Compression (Withdrawn 2005)." ASTM International, West Conshohocken, PA.

ASTM D4543-08e1. 2008. "Standard Practices for Preparing Rock Core as Cylindrical Test Specimens and Verifying Conformance to Dimensional and Shape Tolerances (Withdrawn 2017)." ASTM International, West Conshohocken, PA.

Calayir, Yusuf, and Muhammet Karaton. 2005. "A continuum damage concrete model for earthquake analysis of concrete gravity dam–reservoir systems." *Soil Dynamics and Earthquake Engineering* 25 (11): 857-869.

Carreira , Domingo J., and Kuang-Han Chu. 1985. "Stress-Strain Relationship for Plain Concrete in Compression." *ACI Journal Proceedings* 82 (6): 797-804.

Collins, Michael P., and Denis Mitchell. 1997. *Prestressed Concrete Structures.* New Jersey: Prentice Hall.

Dassault Systèmes Simulia Corp. n.d. "ABAQUS Theory Manual. (6.12)"

Dassault Systèmes Simulia Corp. n.d. "ABAQUS User's Manual. (6.12)"

Desai, C. S., and H. J. Siriwardane. 1982. "Numerical Models for Track Support Structures." *Journal of the Geotechnical Engineering Division* (ASCE) 108 (3): 461-480. Cited by: Kumaran, G., Devdas Menon, and Krishnan Nair. 2002. "Evaluation of dynamic load on railtrack sleepers based on vehicle-track modeling and analysis." *International Journal of Structural Stability and Dynamics* 2 (3): 355-374.

Hillerborg, A., M. Modéer, and P.-E Petersson. 1976. "Analysis of crack formation and crack growth in concrete by means of fracture mechanics and finite elements." *Cement and Concrete Research* 6 (6): 773-781.

Hsu, L. S., and C.-T. T. Hsu. 1994. "Complete stress-strain behaviour of high-strength concrete under compression." *Magazine of Concrete Research* 301-312.

Jankowiak, T., and T. Łodygowski. 2005. "Identification of parameters of concrete damage plasticity constitutive model." *Foundations of Civil and Environmental Engineering* 53-69.

Kaewunruen, Sakdirat , Erosha K. Gamage, and Alex M. Remennikov. 2016. "Modelling Railway Prestressed Concrete Sleepers (Crossties) With Holes and Web Openings." *Procedia Engineering* 161: 1240-1246.

Kaewunruen, Sakdirat, and Alex M. Remennikov. 2010. "Dynamic Crack Propagations in Prestressed Concrete Sleepers in Railway Track Systems Subjected to Severe Impact Loads." *Journal of Structural Engineering* 136 (6): 749-754.

Kmiecik, P., and M. Kamiński. 2011. "Modelling of reinforced concrete structures and composite structures with concrete strength degradation taken into consideration." *Archives of Civil and Mechanical Engineering* 11 (3): 623-636.

Lee, J., and G. Fenves. 1998. "Plastic-Damage Model for Cyclic Loading of Concrete Structures." *Journal of Engineering Mechanics* 124 (8): 892-900.

Li, Dingqing, and Ernest T. Selig. 1995. "Wheel/Track Dynamic Interaction: Track Substructure Perspective." *Vehicle System Dynamics* 24: 183-196. Cited by: Kumaran, G., Devdas Menon, and Krishnan Nair. 2002. "Evaluation of dynamic load on railtrack sleepers based on vehicle-track modeling and analysis." *International Journal of Structural Stability and Dynamics* 2 (3): 355-374.

Lubliner, J., J. Oliver, S. Oller, and E. Oñate. 1989. "A plastic-damage model for concrete." *International Journal of Solids and Structures* 25 (3): 299-326.

Manda, Kartik R., Marcus Dersch, Riley J. Edwards, and David A. Lange. 2014. "Vertical Load Path Under Static and Dynamic Loads in Concrete Crosstie and Fastening Systems." *ASME/IEEE Joint Rail Conference.* ASME. doi:10.1115/JRC2014-3832.

Mayville, Ronald A., Liying Jiang, and Matthew Sherman. 2014. "Performance Evaluation of Concrete Railroad Ties on the Northeast Corridor." Publication, DOT/FRA/RPD-14/03.

Ortiz, Albert R., Juan M. Caicedo, and Dimitris Rizos. 2016. "Finite Element Model of High Strength Reduced Modulus High Performance Concrete." *ASME/IEEE Joint Rail Conference.* ASME. doi:10.1115/JRC2016-5834.

Phillips, D. V., and Zhang Binsheng. 1993. "Direct tension tests on notched and un-notched plain concrete specimens." *Magazine of Concrete Research* 45 (162): 25-35.

Popovics, Sandor. 1973. "A numerical approach to the complete stress-strain curve of concrete." *Cement and Concrete Research* 3 (5): 583-599.

RailTEC. 2016. "High Strength, Reduced Modulus (HSRM) Concrete Crosstie Testing at University of Illinois at Urbana-Champaign (UIUC)." Testing Report, University of South Carolina, Columbia, SC.

Rezaie, F., and S. M. Farnam. 2015. "Fracture mechanics analysis of pre-stressed concrete sleepers via investigating crack initiation length." *Engineering Failure Analysis* 58: 267-280.

Rizos, Dimitris. 2016. "High Strength Reduced Modulus High Performance Concrete (HSRM-HPC) for Railroad Tie Applications." *Joint Rail Conference.* ASME. doi:10.1115/JRC2016-5798.

Rizos, Dimitris. 2014. *High Strength Reduced Modulus High Performance Concrete for Tie Applications.* https://sdii.ce.sc.edu/ties-project/.

Stolarski, Henryk , Catherine French, and Henryk Stolarski. 1997. "Release Methodology of Strands to Reduce End Cracking in Pretensioned Concrete Girders." *PCI Journal* 42 (1): 42-54.

Sutton, M. A., F. Matta, D. Rizos, S. Rajan, D. H. Mollenhauer, H. W. Schreier, and A. O. Lasprilla. 2017. "Recent Progress in Digital Image Correlation: Background and Developments since the 2013 W M Murray Lecture." *Experimental Mechanics* 57 (1): 1-30.

Tao, Y., and J. F. Chen. 2015. "Concrete Damage Plasticity Model for Modeling FRP-to-Concrete Bond Behavior." *Journal of Composites for Construction* 19 (1). doi:10.1061/(ASCE)CC.1943-5614.0000482.

Van Dyk, Brandon J., Marcus S. Dersch, and Riley J. Edwards. 2016. "International Concrete Crosstie and Fastening System Survey - Final Results." Washington, D.C.: United States Department of Transportation (US DOT), Federal Railroad Administration (FRA).

Yapar, O., P. K. Basu, and N. Nordendale. 2015. "Accurate finite element modeling of pretensioned prestressed concrete beams." *Engineering Structures* 101: 163-178.

Yu, Hailing, and David Jeong. 2015. "Finite Element Bond Models for Seven-Wire Prestressing Strands in Concrete Crossties." *Joint Rail Conference.* ASME. doi:10.1115/JRC2015-5758.

Yu, Hailing, and David Jeong. 2012. "Railroad Tie Responses to Directly Applied Rail Seat Loading in Ballasted Tracks: A Computational Study." *Joint Rail Conference.* ASME. 123-132. doi:10.1115/JRC2012-74149.

Yu, Hailing, David Jeong, John Choros, and Ted Sussmann. 2011. "Finite Element Modeling of Prestressed Concrete Crossties With Ballast and Subgrade Support." *International Design Engineering Technical Conferences and Computers and Information in Engineering Conference.* ASME. 1077-1086. doi:10.1115/DETC2011-47452.

Zeman, John C. 2010. "Hydraulic Mechanisms of Concrete-Tie Rail Seat Deterioration." Master's Thesis, University of Illinois at Urbana-Champaign. http://hdl.handle.net/2142/16733 .

ZETA-TECH. 2010. *Assessment of Concrete Tie Life on US Freight Railroads.* Report, Railway Tie Association. http://www.rta.org/assets/docs/TieReports/tie%20report%2012.pdf.

Zhou, F. P., F. D. Lydon, and B.I.G. Barr. 1995. "Effect of coarse aggregate on elastic modulus and compressive strength of high performance concrete." *Cement and Concrete Research* 25 (1): 177-186.